UNIVERSIDAD DE CHILE
FACULTAD DE CIENCIAS FÍSICAS Y MATEMÁTICAS
DEPARTAMENTO DE ASTRONOMÍA

TYPE II SUPERNOVAE LIGHT CURVES CHARACTERIZATION USING MORIYA WIND ACCELERATION HYDRODYNAMICAL MODELS

TESIS PARA OPTAR AL GRADO DE
MAGÍSTER EN CIENCIAS, MENCIÓN ASTRONOMÍA

JAVIER IGNACIO SILVA FARFÁN

PROFESOR GUÍA:
FRANCISCO FÖRSTER BURÓN

MIEMBROS DE LA COMISIÓN:
PAULINA LIRA TEILLERY
RICARDO MUÑOZ VIDAL
TAKASHI MORIYA

Este trabajo ha sido parcialmente financiado por FONDECYT REGULAR NRO 1200710

SANTIAGO DE CHILE
2023

Resumen

CARACTERIZACIÓN DE LAS CURVAS DE LUZ DE LAS SUPERNOVAS TIPO II UTILIZANDO MODELOS HIDRODINÁMICOS DE ACELERACIÓN DEL VIENTO DE MORIYA

Las supernovas de tipo II (SNe) son el tipo más común de SNe en la naturaleza. Se originan por la explosión de estrellas masivas que conservan su envoltura de hidrógeno.

A pesar de ser el tipo más común de SNe, todavía hay incertidumbre en torno al origen de estos objetos. Las curvas de luz (LC) de las SNe de tipo II se ven afectadas por las propiedades de las estrellas progenitoras. Esto ha motivado trabajos sobre modelos teóricos de estos objetos para entender las propiedades de los progenitores de SNe tipo II y el mecanismo de explosión. Los últimos modelos han sugerido la presencia de un medio circunestelar (CSM) denso alrededor del progenitor. Dada la naturaleza transitoria de las SNe, es necesario observar constantemente el cielo para detectarlas. La aparición de surveys ópticos en los últimos años ha aumentado rápidamente el número de SNe conocidas. Esto ha permitido estudiar poblaciones de diferentes tipos de SNe y comprender sus orígenes y diferencias.

Con la llegada del Observatorio Vera Rubin, el número de SNe descubiertas por noche aumentará aproximadamente en un orden de magnitud. Sólo una pequeña fracción de estas SNe tendrá un seguimiento espectroscópico. Por lo tanto, es necesario desarrollar modelos y métodos capaces de estudiar estos objetos utilizando únicamente datos fotométricos.

En esta tesis, se ha desarrollado un método que infiere parámetros físicos de las SNe LC de tipo II usando modelos que tienen en cuenta la aceleración del viento en la superficie de la estrella progenitora. Estos modelos adoptan una ley de velocidad β para formular la aceleración del viento, y los parámetros que se ajustan son la masa de edad cero de la estrella, la energía de la explosión, la tasa de pérdida de masa ($\dot{M}$), el radio CSM y β. También se considera la atenuación (A_V) y el desplazamiento al rojo como parámetros ajustados.

Se infirieron parámetros físicos para una muestra de 186 SNe de tipo II confirmadas con espectro, utilizando datos de fotometría forzada de ZTF y ATLAS. Se encontró que los modelos de estrellas de masas bajas ($<$14 $M_\odot$) que producen un CSM denso ($\dot{M} > 10^{-3}$ [$M_\odot$ yr^{-1}], radio del CSM $\sim 10^{15}$ cm, $\beta > 2$) son los más representativos de la muestra. También se descubrió que el método puede inferir el corrimiento al rojo usando las LCs con mejor precisión que el corrimiento al rojo fotométrico de las galaxias anfitrionas. El código de esta tesis está disponible públicamente en `https://github.com/fforster/surveysim/tree/dev-javier`.

Abstract

Type II Supernovae (SNe) are the most common type of SNe in nature. They originate from the explosion of massive stars that retain their hydrogen envelopes.

Although being the most common type of SNe, there is still uncertainty around the origin of these objects. The light curves (LCs) of type II SNe are affected by the properties of the progenitor stars. This has motivated several works on theoretical modeling of these objects to understand the properties of SNe type II progenitors and the explosion mechanism. The latest models have suggested the presence of a dense circumstellar media (CSM) around the progenitor. Given the transient nature of SNe, it is necessary to constantly scan the sky to detect them. The appearance of optical surveys over the past years had rapidly increased the number of known SNe. Thus, allowing us to study populations of different types of SNe and understand their origins and differences.

With the upcoming of the Vera Rubin Observatory, the number of SNe discovered per night will increase by roughly an order of magnitude. Only a small fraction of these SNe will be spectroscopically follow-up. Therefore, it is necessary to develop models and methods capable of studying these objects using photometric data.

In this thesis, we implemented a method that infers physical parameters from type II SNe LCs using models that take into account wind acceleration at the surface of the progenitor star. These models adopt a β velocity law to formulate wind acceleration, and the parameters that are fitted are zero age main sequence mass of the star, energy of the explosion, mass loss rate ($\dot{M}$), CSM radius, and β. We considered the attenuation (A_V) and the redshift as fitted parameters as well.

We inferred physical parameters for a sample of 186 spectroscopically confirmed type II SNe, using forced photometry data from ZTF and ATLAS. We found that the models from low-mass stars ($<14\ M_\odot$) that produce a dense CSM ($\dot{M} > 10^{-3}$ [$M_\odot$ yr^{-1}], CSM radius $\sim 10^{15}$ cm, $\beta > 2$) are the most representative of the sample. We also found that our method can infer the redshift using the LCs with better accuracy than the photometric redshift of host galaxies.

The code from this thesis is publicly available in `https://github.com/fforster/surveysim/tree/dev-javier`.

Agradecimientos

Primero me gustaría agradecer tod@s l@s docentes que me han acompañado y guiado desde la licenciatura hasta este momento. En especial a Francisco por su paciencia y darse el tiempo casi todas las semanas para reunirse conmigo y discutir sobre mi investigación. Agradecer también a todos quienes forman parte de ALeRCE, lo que aprendí participando de las reuniones del grupo de astronomía y poder participar de este proyecto es algo que recordaré con cariño.

Agradecer a mi familia, en especial a mis padres, mi hermano y mis abuelos, su apoyo es fundamental para mí y sin ellos no podría haber llegado a donde estoy. Gracias por su cariño y todo lo que me han entregado.

Agradecer a mis amigos con quienes hablando, jugando jueguitos, o haciendo cualquier cosa puedo sacar mi mente del estrés constante de la investigación por un momento.

Por último, y para mí más importante, agradecer a una persona muy especial en mi vida, mi polola y mejor amiga, la maca. Tu apoyo, cariño, y constantes palabras de apoyo me motivan a ser la mejor versión de mí.

Table of Content

List of Tables

List of Figures

Chapter 1

Introduction

1.1 Supernovae

A Supernova (SN) is an event that happens when a star end its life, typically with an explosion of energy $\sim 10^{51}$ erg. SNe are often classified by features in their spectra with two main classes: Type I SNe that show no features of hydrogen in their spectra; and type II SNe that show features of hydrogen in their spectra, that arise from the progenitor's envelope [47, 21]. Some sub types for each class are defined from the presence of other element's lines (see Fig. 1.1).

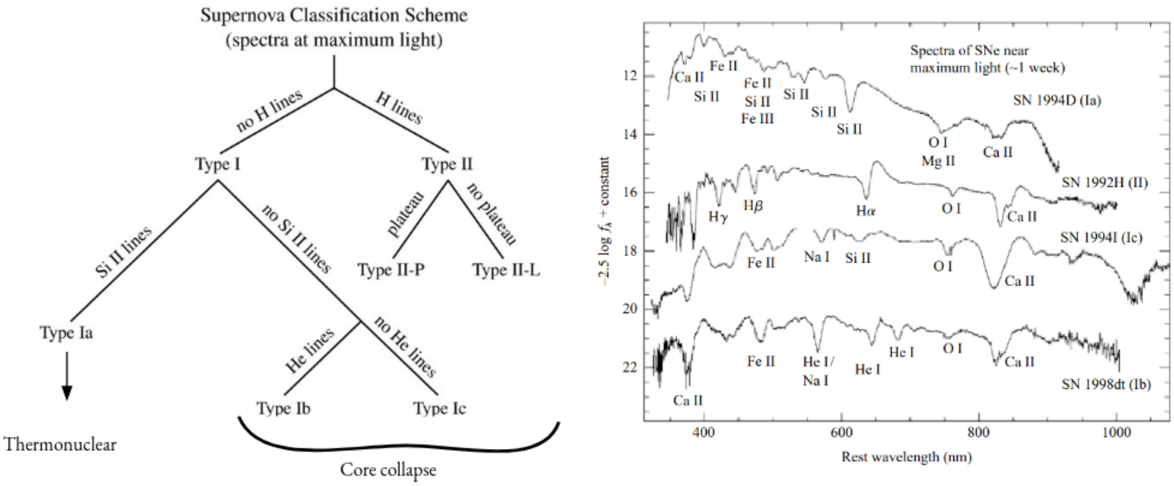

Figure 1.1: Left panel: A classification scheme showing the different types of supernovae (figure modified from [14]). Right panel: Spectra of four types of SNe (from top to bottom); Type Ia, II, Ic, and Ib (figure from [14]).

SNe are the result of two different explosive mechanisms. One mechanism is the thermonuclear explosion that occurs in type Ia SNe when the progenitor white dwarf accretes mass and becomes unstable, undergoing a thermonuclear runaway and producing the SN. The other mechanism is the collapse of the iron core of the progenitor star, occurring in massive stars, with zero-age main sequence (ZAMS) mass $\gtrsim 8 M_\odot$, This mechanism is responsible for producing type II SNe and type I that are not Ia (i.e. Ib, Ic)

1.1.1 Light curves of SNe

The light curve (LC) of a SN contains information about the physics behind these objects. We can identify different phases where certain mechanisms dominate the emission of the SNe. Figure 1.2, illustrates where we can identify a given phase in LCs of type Ia and type II SNe.

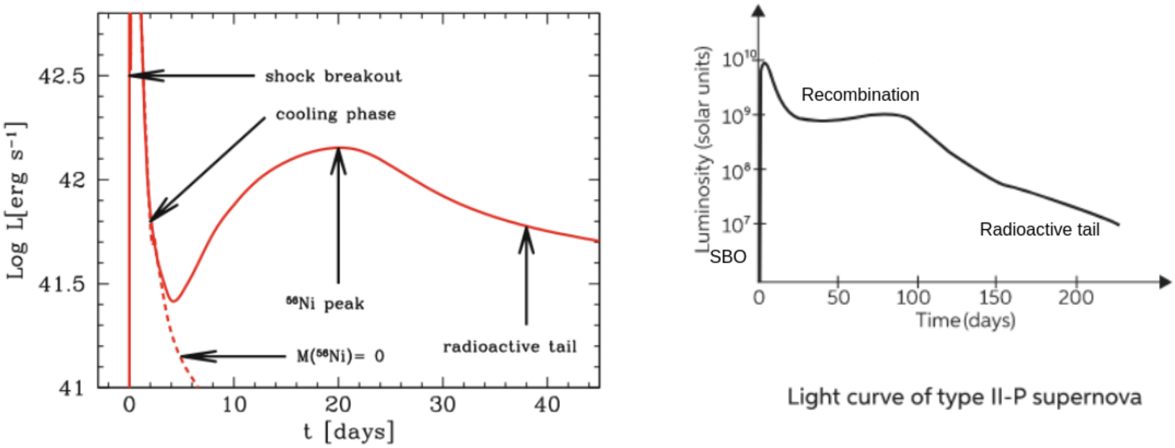

Figure 1.2: Left panel (Figure from [2]): Bolometric LC of Type I SN calculated using a hydrodynamical code from [9], where different phases are indicated. The dashed red line indicates how the LC would look if there was no ^{56}Ni produced. Right panel: Typical type IIP LC, with phases indicated. The effects of the recombination can be seen as the plateau of the LC

The most important phases observed in a SN LC are:

- Shock breakout(SBO): This is the earliest emission from the SN. This process occurs when the shock reaches the edge of the star. This emission is mostly in X-ray/UV and last from seconds to a fraction of an hour. The breakout can be delayed in the case of a star with dense circumstellar medium (CSM), lasting longer (see [24]).
- Shock cooling and ejecta recombination: When the Hydrogen in the envelope of type II SNe gets shock heated (from the SBO), it is ionized and becomes opaque, trapping the photons inside and gradually releasing photons as it cools reaching the recombination temperature (see Fig 1.3). The recombination is typical of type II SNe and it's responsible for the plateau in the LC of these objects.
- Radioactive heating: The shock produces radioactive elements, the most abundant is ^{56}Ni, which decays to ^{56}Co with a half life of 6.07 days. This process produces high-energy photons and positrons, some of these will be down-scattered to optical wavelengths before emerging from the ejecta, which is why LCs peaks at times later than the half life of ^{56}Ni.

- Radioactive tail: Other radioactive elements produced with longer half-life are responsible for fueling the last part of the LC we can observe. For example, the ^{56}Co produced from the decay of ^{56}Ni is also radioactive and decays with a half-life of 77.27 days.

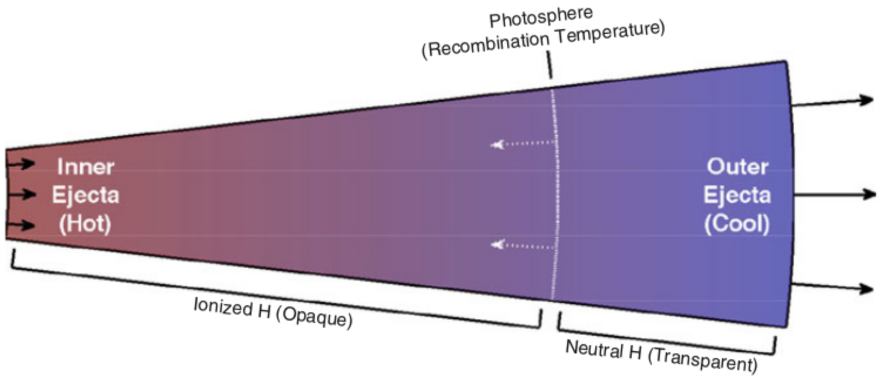

Figure 1.3: (Figure from [2]) Illustration of the recombination process typical of type II SNe. The ejected material is pushed outward, while the cooling occurs from the outside to the inside of the ejecta in mass coordinates, keeping the radius at which the recombination temperatures is reached (roughly) constant, approximately the photosphere (white dotted line)(see [20] for more details).

1.1.2 SNe LC modelling

In this section, we will construct a one-zone analytic model for the evolution of a cloud of gas based on the model for SN LC from [4, 5], and also in some other works that model transient LCs based on the previously mentioned model such as [35, 36, 16, 75]. We will find a general expression that relates the luminosity of the SN with different physical parameters.

We will start from the first law of thermodynamics, the thermal state of the expanding matter evolves as:

$$\dot{E} = -P\dot{V} - \partial L/\partial m + \varepsilon \tag{1.1}$$

Where $E = aVT^4$ is the internal energy, $P = (1/3)aT^4V$ the pressure, $V = 1/\rho$ is the volume, ε is the energy released from radioactive decay, and L the luminosity (the bolometric LC) that is given by

$$L = -4\pi r^2 \frac{\lambda c}{3} \frac{\partial}{\partial r} aT^4 \tag{1.2}$$

where c is the speed of light, $\lambda = 1/\kappa\rho$ is the mean free path with κ being the mean opacity, and ρ the density (see [16]).

We will make the following assumptions:

1. The ejecta goes through homologous expansion and it's spherically symmetric, this means the ejecta radius expands as $R = R_0 + vt$, where R_0 is the initial radius of the ejecta at the moment of shock breakout, and $v = \sqrt{2E_0/M}$ is the charactersitic velocity. The volume of the remnant increases with time as $V(t) = V_0(t/t_0)^3$, where $V_0 = (4\pi/3)R_0^3$ and $t_0 = R_0/v$.
2. The radiation energy dominates over gas energy.
3. ^{56}Ni (the heating source) is located at the center.
4. The optical opacity is constant. A typical value for stripped SNe is $\kappa = 0.1$ cm^2 g^{-1}.
5. The initial radius is small.

Citing the solution from [16], we can find the luminosity as a function of time for homologously expanding photosphere.

$$\begin{aligned} L(t) = \; & \frac{2E_0}{t_d} exp\left[-\frac{t^2}{t_d^2} + \frac{2R_0 t}{vt_d^2}\right] \int_0^t exp\left[\frac{t'^2}{t_d^2} + \frac{2R_0 t'}{vt_d^2}\right] \left(\frac{t'}{t_d} + \frac{R_0}{vt_d}\right) f(t')dt' \\ & + \frac{E_{th,0}}{t_0} exp\left[-\frac{t^2}{t_d^2} + \frac{2R_0 t}{vt_d^2}\right] \end{aligned} \tag{1.3}$$

where f(t) is the time-dependence of the power input (central heating source) , $E_{th,0}$ is the initial internal energy from the SN blast wave, and v is the expansion velocity. The term $t_d = \sqrt{2t_0 t_h}$ is the effective LC timescale, where $t_h = R_0/v$ is the expansion timescale and $t_0 = \sqrt{2\kappa M_{ej}/\beta cv}$ is the diffusion timescale, where M_{ej} is the ejecta mass, κ is the opacity, c is the speed of light, and β is a geometric correction factor. [5] adopted a value of $\beta = 4\pi/9 \approx 13.7$.

And also the solution for the fixed photosphere

$$L(t) = \frac{1}{t_0} e^{-\frac{t}{t_0}} \int_0^t e^{-\frac{t'}{t_0}} f(t')dt' + \frac{E_{th,0}}{t_0} e^{-t/t_0} \tag{1.4}$$

Given these solutions, it is possible to obtain general models for different kind of progenitors tweaking the values of different parameters (see [75]).

We will show as an example one of the most studied models, the heating source produced by the radioactive decay of ^{56}Ni and ^{56}Co. In this model the input luminosity is given by:

$$f(t) = M_{Ni}\left[\varepsilon_{Co} e^{-t/\tau_{Co} + (\varepsilon_{Ni} - \varepsilon_{Co}) e^{-t/\tau_{Ni}}}\right] \tag{1.5}$$

Where M$_{Ni}$ is the initial mass of ^{56}Ni, $\varepsilon_{Ni} = 3.9 \times 10^{10}$ erg s^{-1} g^{-1} and $\varepsilon_{Co} = 6.8 \times 10^9$ erg s^{-1} g^{-1} correspond to the energy generation of ^{56}Ni and ^{56}Co respectively, and $\tau_{Ni} = 8.8$

days and $\tau_{Co} = 111$ days are the decay rate of ^{56}Ni and ^{56}Co respectively. By plugging the eq. 1.5 into eq. 1.4 we find the bolometric luminosity of a transient powered by radioactive decay.

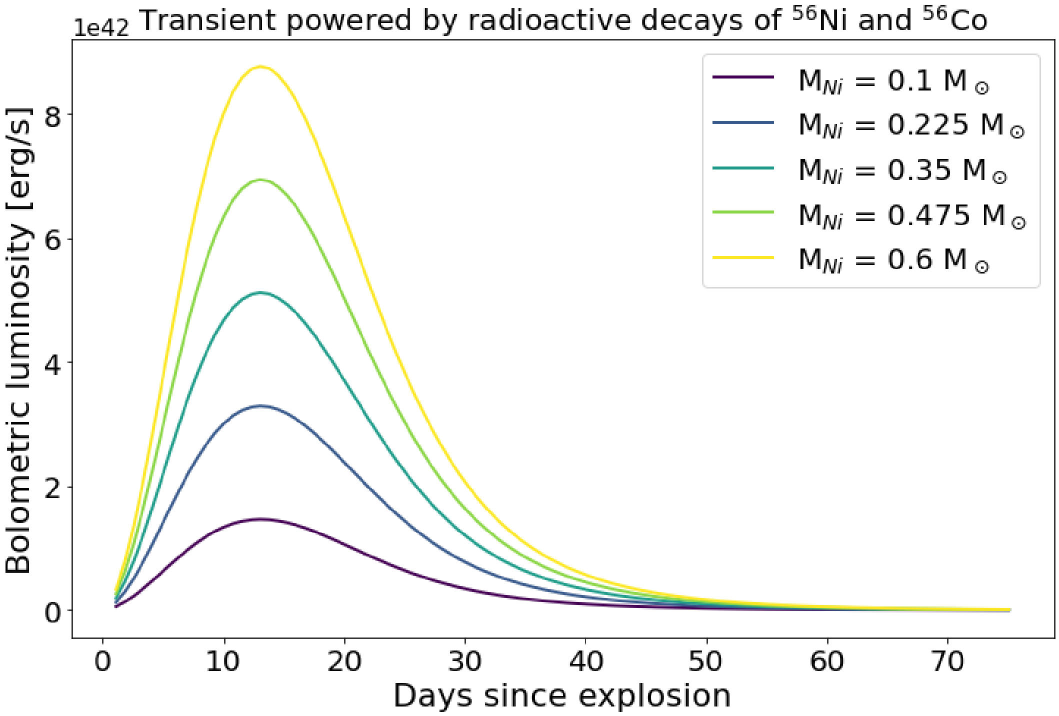

Figure 1.4: Light curve of transient powered by radioactive decay for different Ni Mass values

The only free parameter of the radioactive decay model is M_{Ni}. We show the effect of varying this parameter in Fig. 1.4, for a $M_{ej} = 1.4 M_\odot$ (representative of a SN Ia), and $\kappa = 0.1$ cm^2 g^{-1}.

1.1.3 Type II SNe

Type II SNe are core collapse SNe whose progenitors are Red Supergiant (RSGs) stars. The progenitors ZAMS masses are expected to be around 8 - 25 $M_\odot$, they reach peak luminosities $\sim 10^{42}$ ergs s^{-1}, and are the most common type of SNe [40] (see Fig. 1.5).

These SNe can be sub-classified by the shape of their LCs as II-P when the LC shows a plateau of about 100 days since maximum, and II-L when it shows a linear decline [6]. There has been debate around whether this distinction comes from two different populations of progenitors or if there is a continuous transition between type IIL and type IIP, although some works have shown that there is a continuous transition when the sample is large enough [3]. In this work, we are not going to make a distinction between type IIL and type IIP and just going to refer to them as type II.

Type II SNe show a wide range of photometric features, that are attributed to the properties of the progenitor and its evolutionary history. To understand the diversity of

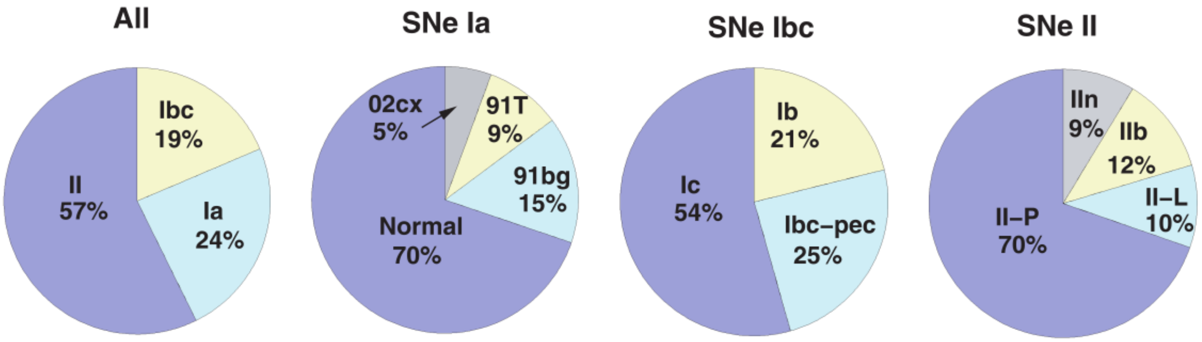

Figure 1.5: Figure from [40], The observed fractions of the sub classes of SNe in the sample from [40].

their LCs we need to study their progenitors and all the possible mechanism that could affect the LC.

The question that arises is, how can we study the progenitor of a SN?. The most direct way is to check in archival images if there is a detection of an object in the position where the SN occurred. The limitation of this method is that it is only possible to do with nearby objects out to 30 Mpc [45].

Some of the first works that did this were [74, 64], this method led [63] to notice a discrepancy between the higher mass of a RSG progenitors of SNe, finding an upper mass limit of 17 $M_{\odot}$, in comparison with the RSGs population in Local group galaxies, that have masses up to 25 $M_{\odot}$, this is known as the "Red Supergiant problem". This upper mass limit differs in value in works that use different methods or larger samples, but the RSG problem remains an open problem.

There are other two methods to study progenitors, but they are indirect. The first is to model late time spectra, as done in [34], based on nucleosynthesis from stellar evolution and explosion spectral modeling when applied to the late time spectra of a SN it is able to constrain the mass of the object. The second method is to use hydrodynamical modeling to study the LC of the SN, as discussed previously, the LC of a SN is heavily affected by the physics behind the SN so it is affected by different physical parameters, for example: ZAMS mass, the energy of the explosion, the amount of ^{56}Ni, the mass loss rate, etc.

1.2 Hydrodynamical models

Hydrodynamical modeling of type II SNe used to have problems explaining the rise times of these objects (around 5-10 days), the models predict to have slower than observed rise times and therefore obtained low values of the radius of the progenitor that was in disagreement with the radius expected for RSGs ([25, 26, 27, 60]). As a possible explanation for these observed slow rise times, [27] proposed two possible scenarios. The first is that the shock cooling from the core collapse of RSG with small and dense envelopes is being observed. The second is that we are observing the delayed and prolonged shock breakout of the collapse of a RSG embedded within circumstellar material. In the latter case, SN ejecta will clash into the dense CSM, this collision will result in the conversion of the kinetic energy to radiation, making the SN LC rise fast. This is supported by previous work [48] where it is shown that the LC of SN 2009kf, a type II SN, is reproduced by LC models with a dense CSM. Also, [37] detected narrow emission lines in early-time spectra of a type II SN as evidence of a dense CSM around its progenitor.

The problem is that to explain this dense CSM structure, the RSG progenitor needs to have mass loss rate values higher than the ones a normal RSG has, so it is expected that some mechanism in the final years before explosion enhances the mass loss of the progenitor. Two possible mechanisms could explain the dense CSM, 1) Wind Acceleration: [51, 49] notices that when the wind is accelerated following a beta velocity law in the last ~ 100 years before explosion it is possible to obtain similar conditions to high mass loss values with this enhanced mass loss, although mass loss rates are also larger than expected; 2) Pre-explosion outburst: Considers the ejection of CSM caused by wave heating during nuclear burning in the final years before the explosion, some works related to this are [22, 52]. In this thesis, we are going to work with models that take into account wind acceleration, in the next subsection we will expand on this topic.

1.2.1 Moriya wind acceleration models

Moriya introduced the first LC hydrodynamical models that takes into account wind acceleration in RSG progenitors [51, 49]. The density ρ of the CSM in this model is given by the following expression:

$$\rho_{CSM}(r) = \frac{\dot{M}}{4\pi v_{wind}(r)} r^{-2} \tag{1.6}$$

Where $\dot{M}$ is the progenitor's mass-loss rate and v_{wind} is the wind velocity that is given by a β-velocity law:

$$v_{wind}(r) = v_0 + (v_\infty - v_0)\left(1 - \frac{R_0}{r}\right)^{\beta} \tag{1.7}$$

Where v_0 is the initial wind velocity, v_∞ is the terminal wind velocity, and R_0 is the wind launching radius that is set at the stellar surface. In [49], they fixed $v_\infty = 10$ km s^{-1}, and v_0 is chosen so that the CSM density is smoothly connected from the surface of the progenitors. The wind acceleration of RSGs is unknown, but we can constrain it given that we know that OB stars have β values around 0.5 - 1 [31], and RSGs are known to experience slower wind acceleration than OB stars [8, 43], so a value of β between 1 and 5 is assumed for RSGs.

The SN progenitors were obtained using the the public stellar evolution code MESA [54, 55, 56, 57]. While the LCs from the explosions of the progenitors with CSM are numerically obtained by using the one-dimensional multi-group radiation hydrodynamics code STELLA [10, 12, 11]

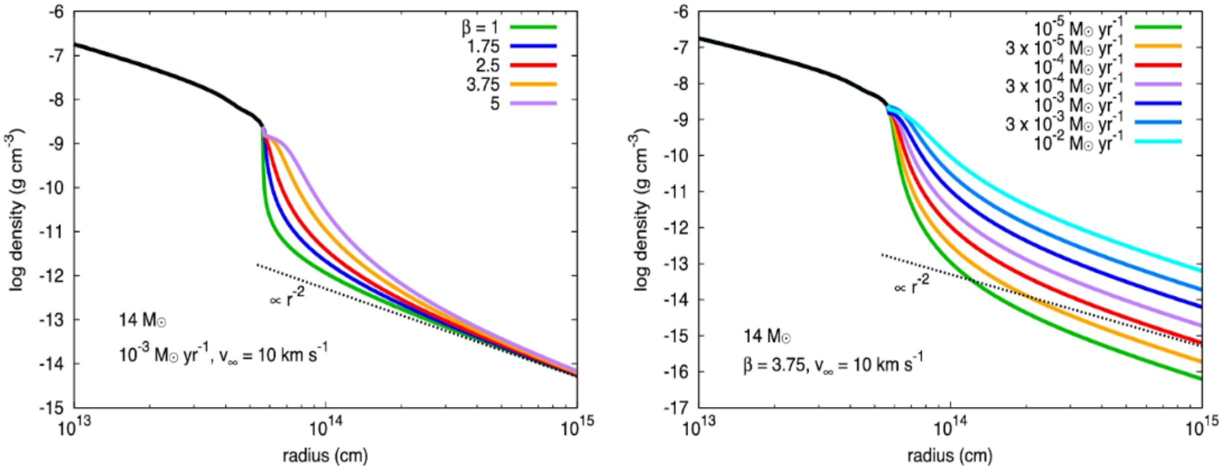

Figure 1.6: Figure from [49], Density structure of a 14 M$_\odot$ At the left: Fixed $\dot{M} = 10^{-3}$ M$_\odot$ yr^{-1} and for different β. The dotted line is the CSM structure which assumes that the wind is instantaneously accelerated to the terminal velocity. At the right: Fixed $\beta = 3.75$ for different $\dot{M}$ values. The dotted line is the CSM structure which assumes that the wind is instantaneously accelerated to the terminal velocity for the $\dot{M} = 10^{-4}$ M$_\odot$ yr^{-1} value

Figure 1.6, shows how the effect of β and the mass loss rate affects the CSM structure near the progenitor's surface, in the immediate vicinity of the progenitor's surface the effect of higher values of β (slower winds), have similar effects of higher mass loss rates, where a dense CSM is obtained. Figure 1.7 shows representative g band LCs for different values of β while fixing the mass loss rates, and for different values of mass loss rates while fixing β, once again it can be seen that slower winds have similar effects to higher mass loss rates at early times, being able to produce LCs with fast rise times like the ones observed.

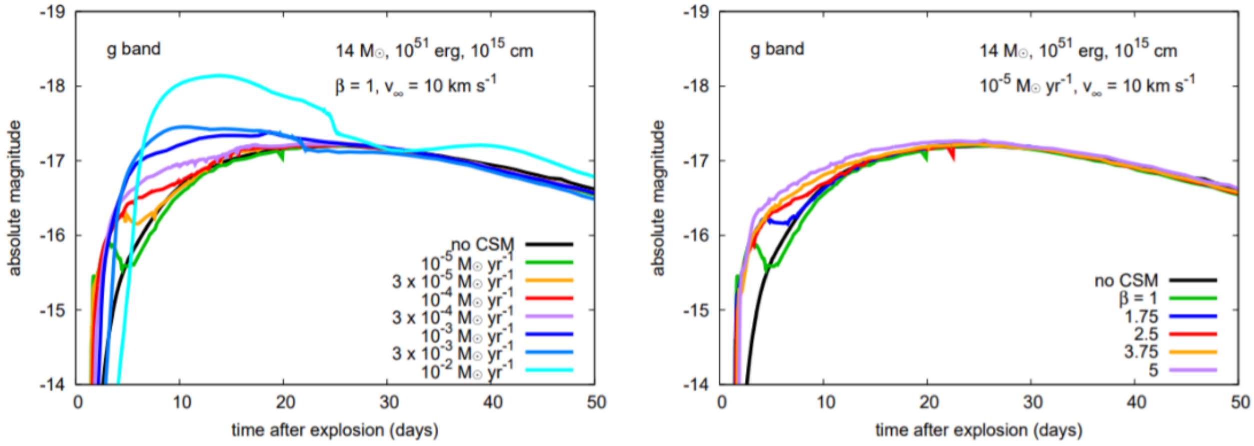

Figure 1.7: From [49], At the left: g band LCs with fixed $\beta = 1$ and different mass-loss rates, while at the right panel: g band LCs with a $\dot{M} = 10^{-5}$ M$_\odot$ yr^{-1} and different β.

The hydrodynamicals models not only consider the effect of β in the light curves, but also take into account the effect of the mass of the ZAMS progenitor, the energy of the explosion, the mass loss rate, and the CSM radius. A total of 1686 models are generated as a combination of progenitors parameters from table 1.1.

Table 1.1: RSG progenitor parameters

Mass ($M_\odot$)	**Energy** (foe)	**Mass loss rate** ($M_\odot$ / year)	**CSM radius** (10^{15} cm)	β
12	0.5	0	0	0
14	1	10^{-5}	0.1	1
16	1.5	3×10^{-5}	0.3	1.75
	2	10^{-4}	0.5	2.5
		3×10^{-4}	1	3.75
		10^{-3}		5
		3×10^{-3}		
		10^{-2}		

1.3 Surveys

The number of discovered supernovae has largely increased over the last decades (see Figure 1.8). Given the transient nature of these objects, the increase is related to the contribution of different astronomical surveys that have been scanning the sky constantly. Not only the surge of more surveys has allowed us to improve and enrich our understanding of the transient universe, but the progress in telescope instrumentation alongside the progress in computational power has allowed us to produce and process more data than ever before.

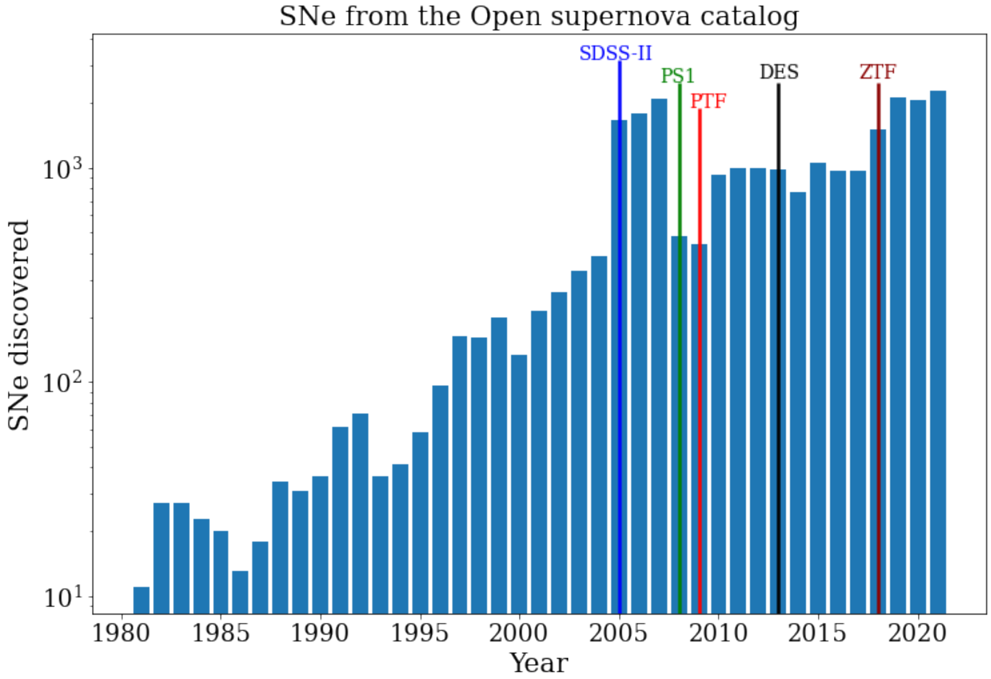

Figure 1.8: Number of SNe discovered per year from the open supernova catalog [32], some survey's starting year of operation are shown with a vertical color line with their respective names on top

All the experience from previous surveys and the advances previously mentioned have led to the construction of the Vera C. Rubin Observatory [42], whose goal is to conduct the 10-year Legacy Survey of Space and Time (LSST) using 6 different filters (ugrizy), and producing around 20 TB of data per night.

LSST is forecast to discover three to four million more SNe during its ten-year survey [41]. A lot of these objects are not going to be properly followed-up, so we are not going to have more information about them other than the LC of LSST and maybe photometric data from other surveys. Therefore, we believe it is necessary to take advantage of all this data that it is going to be produced and design methods capable of doing science with the data available.

This is why in this thesis we will do Bayesian inference with SNe data from ZTF and ATLAS, to infer physical parameters from a sample of 186 type II SNe LCs using the method from [24]. We will be able to study the distribution of parameters from the sample to check what are the parameters that better describe the data, search for correlation between parameters, and test the viability of using our method with large samples of data.

Chapter 2

Data

As previously stated, the idea of this thesis is to implement the method from [24] in a large sample of type II SNe, with public data of currently active surveys, the Zwicky Transient Facility (ZTF) and Asteroid Terrestrial-impact Last Alert System (ATLAS). In this section, we will explain the objectives and technicalities of these surveys.

2.1 ZTF

ZTF is an optical time domain survey that uses the Palomar 48-inch Schmidt telescope [7]. Its goal is to do a systematic study of the optical night sky, using an extremely wide-field of view camera scanning the entire Northern sky every two days. ZTF observes in three filters: ZTF-g, ZTF-r, and ZTF-i; doing observations of 30 s exposure time. During dark time the bands ZTF-g, ZTF-r, ZTF-i have a limiting magnitude of 21.1, 20.9, 20.2 respectively [19]. Specifications of the telescope are in table 2.1

Half of ZTF's CCDs have a single-layer anti-reflective coating, while the other half has a dual-layer coating, this implies that the CCDs have different quantum efficiency (QE) depending on the coating. In this work, we will consider 4 filters. Instead of 2 from ZTF given the different QE of CCDs, instead of having just a g and r filter, we will have a g_single and r_single, for g and r (respectively) observations with the single-layer anti-reflective coating CCD, and g_multi and r_multi for g and r (respectively) observations with the dual-layer coating CCD. This will be significant when we implement the method of [24] to be used in the data. ZTF transmission curve (filter + QE + atmosphere) is shown in Fig. 2.1

2.2 ATLAS

ATLAS is a sky survey system funded by NASA and developed by the University of Hawaii to find dangerous near-Earth asteroids [71]. It consists of four telescopes, two in Hawaii (Mauna Loa and Haleakala), one in Chile, and one in South Africa. Despite its main goal being the

Table 2.1: Specifications of the ZTF Observing System from [7]

Telescope and Camera	
Telescope	Palomar 48 inch (1.2 m) Samuel Oschin Schmidt
Location	33°21’26”.35 N, 116°51’32”.04 W, 1700 m
Camera field dimensions	7.50° N-S × 7.32° E-W
Camera field of view	55 deg^2
Light-sensitivity area	47 deg^2
Fill factor	86.7%
Filters	ZTF-g, ZTF-r, ZTF-i
Image quality	g = 2.1”, r = 2.0”, i = 2.1” FWHM
Median Sensitivity (30 s, 5 σ)	$m_g = 20.8$, $m_r = 20.6$, $m_i = 19.9$
	$m_g = 21.1$, $m_r = 20.9$, $m_i = 20.2$ (new moon)
CCD Array	
Science CCDs	16 6144 × 6160 pixel e2v CCD231-C6
Guide and Focus CCDs	4 2k × 2k STA; delta doped by JPL
Pixels	15 μm pixel^{-1}
Plate scale	1.01” pixel^{-1}
Chip gaps	0.205° N-S, 0.140° E-W
CCD readout channels	4
Readout time	8.2 s
Read noise	10.3 e- (median)
Gain	5.8 e- / ADU
Linearity	1.02% ± 0.09% (correction factor variation)
Saturation	350000 e-

detection of asteroids, the high cadence of observations (2 per night) allows it to detect 10-15 SN candidates per night [65]. ATLAS observes in two bands: The cyan (c, covering 420-650 nm); and the orange band (o, 560-820 nm). Specifications of the telescopes are in table 2.2

ATLAS on Haleakala usually observes in c band during dark time on and o band during bright time, and always observes in o band on Mauna Loa. The transimission curve of ATLAS is shown in Fig. 2.2

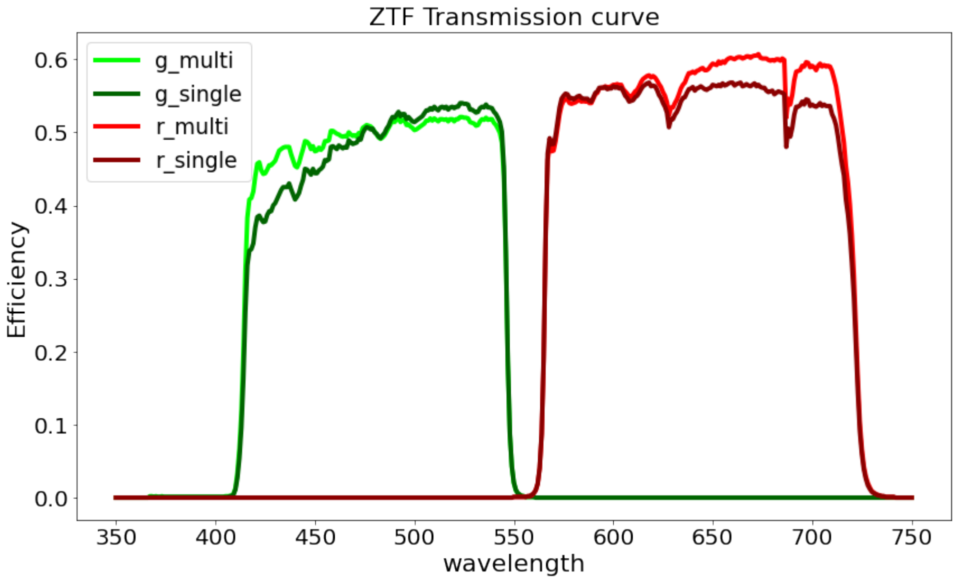

Figure 2.1: Total transmission curve of ZTF, including the effects of the filters g and r, the QE (including the effects of different coating), and the atmosphere.

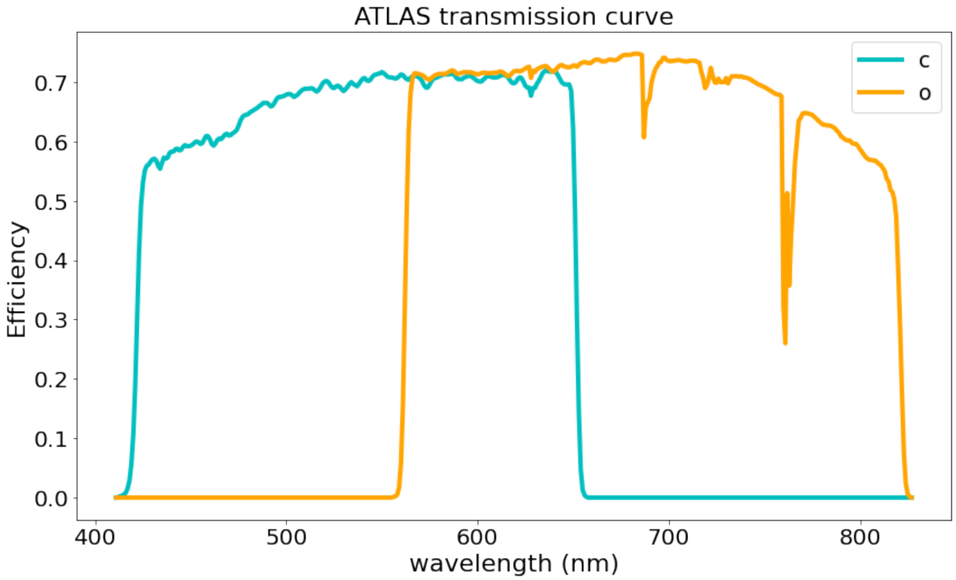

Figure 2.2: Total transmission curve of ATLAS, including the effects of the filters c and o, the QE, and the atmosphere.

Table 2.2: Specifications of ATLAS

ATLAS technical specifications	
Telescope design	DFM custom Wright Schmidt
Location Maunaloa (Hawaii)	19.5361°N, -155.5761°E, 3397m
Location Haleakala (Hawaii)	20.7076°N, -156.2570°E, 3052 m
Location Chile	30.47103°S, 70.76498°W, 1759m
Location South Africa	32.3783°S, 20.8105°E, 1570m
Telescope aperture	0.5 m
Telescope focal length	1.0 m (f/2.0)
Telescope field of view	7.4°
Individual camera field of view	30 deg^2
Detector	STA-1600, 10.5x10.5k CCD
Pixel size	9 μm
Pixel scale	1.86”
Effective PSF FWHM (assuming 1.5” seeing)	3.8”
Filters	orange (o), cyan(c)
Nominal exposure time	30 s
Expected readout time	6 sec
Saturation	r $\sim$ 12.5
Survey coverage	20,000 deg^2 three times per night
Best 5 σ limiting magnitude (dark)	19.8 o band

Chapter 3

Methods

In this chapter, we describe the data we use from ZTF and ATLAS. First, we explain how we get the photometry data from ZTF and ATLAS and the cleaning we did to discard outliers. Then we explain the method from [24] and how it was adapted and optimized to be used in our data.

3.1 Data selection

The first sample was selected using the Automatic Learning for the Rapid Classification of Events (ALeRCE) light curve classifier [23, 69]. We selected all the objects classified as SNII with a probability higher than 0.3. At the time when this was done, a sample of 452 possible SNe was selected. This process allowed us to search for SNe that have a minimum number of detections in ZTF and that have standard light curves of type II SNe

The next step was to keep objects that were spectroscopically classified as type II SNe. This step was done by crossmatching with the Transient Name Server (TNS) database and discarding the objects in our sample that were not type II SNe. 252 confirmed type II SNe were found in the 452 possible candidates sample, 19 were classified as type IIn. Of this 252 confirmed SNe, we discarded those that have large gap between the last observation previous to the SN, thus we can have an estimation of the explosion time, this leave us with a final sample of 186 confirmed type II SNe.

We could have started this process by selecting a sample of confirmed type II SNe, but this way we would have had many SNe with bad coverage in ZTF or with anomalous LCs that would produce unreliable results. Also, the classification reported in TNS is not always reliable, because the spectra could have been taken too early or too late to correctly classify the object as a type II SN.

Then we proceed with acquiring the data for both surveys using the forced photometry services provided. For ZTF see [46] and for ATLAS see `https://fallingstar-data.com/forcedphot/` [71] and [65]. To download the data, we provided the coordinates from the ALeRCE LC classifier and the range of days going from 50 days before the first alert reported by ZTF to the day the data was requested.

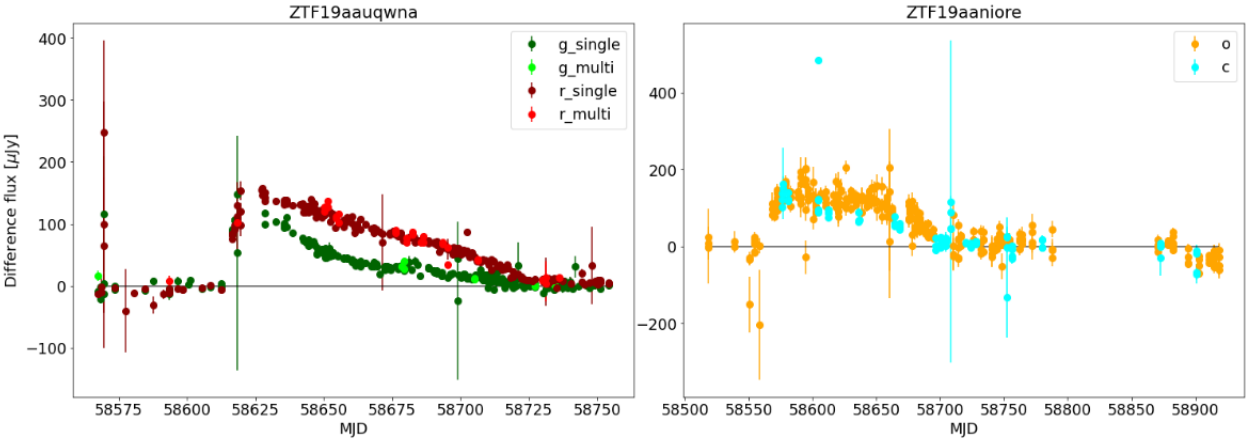

Figure 3.1: LCs before cleaning, Left panel: LC from ZTF forced photometry of SN2019fem/ZTF19aauqwna. Right Panel: LC from ATLAS forced photometry of SN2019ceg/ZTF19aaniore

The LCs of SN2019fem (ZTF19aauqwna), and SN2019ceg (ZTF19aaniore) are displayed in Fig. 3.1. The first shows ZTF data (left panel), and the second ATLAS data (right panel). Both LCs have multiple data points that are either outliers and/or measurements with large errors. In the next section, we will discuss how we clean the data and the parameters used to do this for ATLAS and ZTF.

3.2 Light curve cleaning

We will start describing how we cleaned data from ZTF. The procedure presented in this section is the product of the work of a group of astronomers from ALeRCE (where I was included) that studied this issue. The following criteria were found to satisfactorily clean the data.

First, we follow the guidelines from [46] where we filter by the `procstatus` variable where any observation with a `procstatus` (Per-epoch processing status codes) value not equal to 0 (Successful execution), or 56 (One or more epochs have photometry measurements that may be impacted by bad pixels), or 57 (One or more epochs had no reference image catalog source falling within 5 arcsec) was removed. Any observation where `infobits` value (that is related to the quality of CCD-quadrant-based images from individual epochs) was not equal to 0 was removed.

Also, we perform quality cuts following The ZTF Science Data System (ZSDS) Advisories and Cautionary Notes, from the ZTF DR5 Documentation, section 2.4, flagging as a bad data point any data point that satisfies any of the following conditions:

- For g filter:

  - zeropoint magnitude $>$ 26.7 - 0.2 × airmass OR
  - zeropoint magnitude rms $>$ 0.06 OR
  - zeropoint magnitude $<$ threshold[ccd] - 0.2 × airmass
- For r filter
  - zeropoint magnitude $>$ 26.65 - 0.15 × airmass OR
  - zeropoint magnitude rms $>$ 0.05 OR
  - zeropoint magnitude $<$ threshold[ccd] - 0.15 × airmass

Where threshold[ccd] varies depending on the CCD used for the observation and the filter. The value of threshold[ccd] can go from 25.6712 to 25.9225 for the g-filter and from 25.6199 to 25.9759 for the r-filter. Finally, for those cases when the SN was already in the difference image, a baseline correction was applied when possible. This means when data before the explosion was available.

The ATLAS reduction pipeline has a custom built point-spread-function (PSF) fitting routine that runs on the difference images to produce flux measurements of all sources that are detected at 5σ or more above the background noise. This routine is called tphot and is based on the algorithms discussed in [72, 66]. The forced photometry is again PSF based using tphot.

At the time of this work and unlike the case of ZTF, there were no guidelines available to clean ATLAS forced photometry LCs, so we explored the available metrics to discard contaminated observations or with large error bars. Observations that do not fulfill any of the following conditions were removed:

- $0.5 <$ chi/N < 3
- flux $>$ -100 [μJy]
- magnitude error < 5
- sky (o filter) magnitude > 18, sky (c filter) magnitude > 18.5
- flux error < 40 [μJy]

Where chi/N is the reduced χ^2 of the PSF fit. In Fig. 3.2 the result of this algorithm applied to the LCs from Fig. 3.1 is shown. It is possible to notice that points with large error bars are no longer in the LC and neither are the points that clearly are outliers.

Fig. 3.3 shows two LCs combining data from ZTF and ATLAS. ATLAS data, although having larger errors than ZTF data, fill the gap between ZTF data points, allowing us to have a better estimation of the whole LC behavior. This shows the advantages of using data from both surveys to constraint SNe.

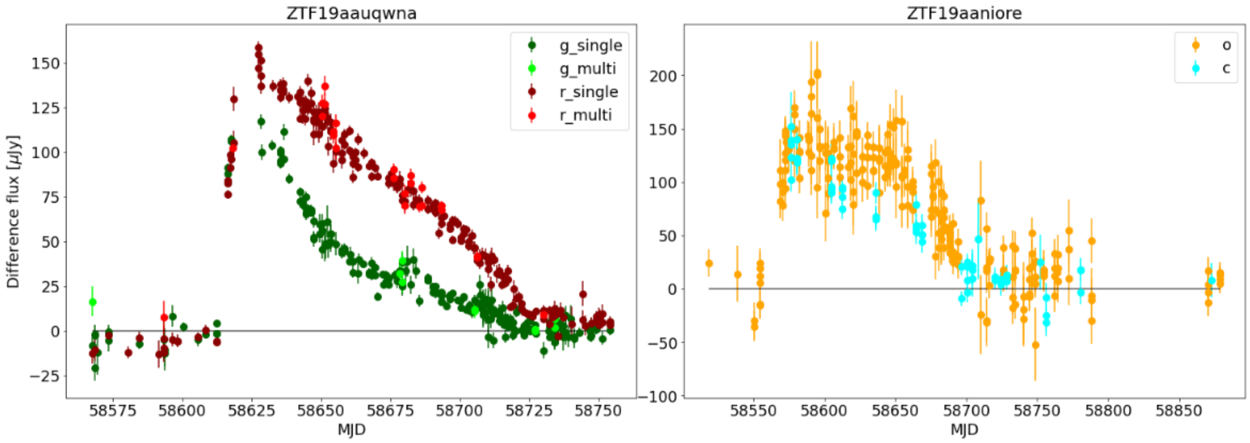

Figure 3.2: Same as Fig. 3.1 but discarding outliers, Left panel: LC from ZTF forced photometry of SN2019fem/ZTF19aauqwna after cleaning. Right Panel: LC from ATLAS forced photometry of SN2019ceg/ZTF19aaniore after cleaning.

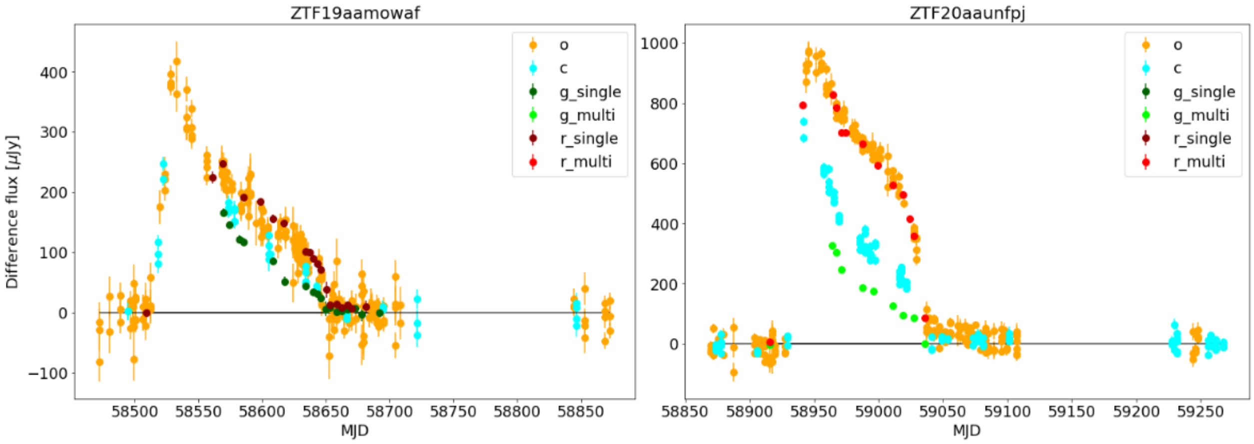

Figure 3.3: LCs using forced photometry data from ZTF and ATLAS. Left panel: Clean LC of SN2019asz/ZTF19aamowaf using ZTF and ATLAS forced photometry. Right Panel: Clean LC of SN2020fsb/ZTF20aaunfpj using ZTF and ATLAS forced photometry

3.3 Physical parameters

As previously stated, the method used in this work is the same from [24], that uses a Bayesian approach to infer physical parameters from the LC of a SN. However, before using a Bayesian approach, we need to be able to compare our data to the models and to explore the whole parameter space quickly. This is why we first perform the following steps.

3.3.1 Synthetic light curves

The first step is to produce synthetic LCs for any redshift, attenuation, and explosion time from hydrodynamic models time series of spectra. A standard Λ-CDM model is assumed and then the spectra time series are redshifted and attenuated with distance assuming a Cardelli law with $R_V = 3.1$ for dust attenuation. The spectra are integrated with the bands from ATLAS and ZTF to generate synthetic LCs. In our work, we use the time series spectra generated from [49] models, as a combination of the parameters of Table 1.1, having a total of 1686 spectra time series. We pre-compute the LCs for all the bands and all available models in a logarithmically spaced time array using 100 points from 10^{-3} days to 1000 days, a logarithmically spaced attenuation array for 10 different values from 10^{-4} to 10, and a logarithmically spaced redshift array for 30 different values from 10^{-3} to 1, producing a total of 505800 synthetic LCs as a combination of the model physical parameters, attenuation, and redshift.

The generated synthetic LCs are displayed in Fig. 3.4 for the ATLAS o filter, and for ZTF g filter in Fig. 3.5 varying all the different parameters of the physical parameter vector, the attenuation value (A_V), and the redshift (z), one at a time while the others parameters are fixed.

3.3.2 Interpolation

To explore the whole parameter space and search for intermediate values it is necessary to interpolate between the models with different physical parameters. First, it's necessary to find the closest values in all the intrinsic physical dimensions and find all the models that have a combination of these values, that will be call $\vec{\theta}_{\text{close}}$. The final LC will be a weighted combination of these models,

$$m(t, t_{\text{exp}}, z, A_v, \vec{\theta}_{\text{close}}) = \sum_{\vec{\theta}_i \in \vec{\theta}_{\text{close}}} \hat{w}(\vec{\theta}, \vec{\theta}_i) m(t, t_{\text{exp}}, z, A_v, \vec{\theta}_i) \tag{3.1}$$

where $m(t, t_{\text{exp}}, z, A_v, \vec{\theta}_{\text{close}})$ is the magnitude of the model at a given observation time t, explosion time t_{exp}, redshift z, a given attenuation A_V and a given vector of model parameters $\vec{\theta}$; and the normalized weights $\hat{w}(\vec{\theta}, \vec{\theta}_i)$ are defined as:

$$\hat{w}(\vec{\theta}, \vec{\theta}_i) = \frac{w(\vec{\theta}, \vec{\theta}_i)}{\sum_{\vec{\theta}_j \in \vec{\theta}_{\text{close}}} w(\vec{\theta}, \vec{\theta}_i)} \tag{3.2}$$

the weights are defined as a function of the parameter vectors $\vec{\theta}$ and $\vec{\theta}_i$. A problem that arises is how to compare values in different dimensions from the vector of physical parameters. To avoid this problem the weights are defined to be inversely proportional to the product of the differences in all the dimensions, given by the following expression

$$w(\vec{\theta}, \vec{\theta}_i) = \left(\prod_j |\theta^j - \theta_i^j| + \delta^j \right)^{-1} \tag{3.3}$$

where $\vec{\delta}$ is a vector with the same physical units as the parameters vector, but much smaller than the typical separation in the grid models, in order to avoid divergence when a given model matches the coordinates of known models.

Interpolated LCs are shown in Fig. 3.6 for ATLAS o filter, and in Fig. 3.7 for ZTF g filter, similar to Fig. 3.4 and Fig. 3.5 respectively. Here it is possible to see how varying different parameters affect the LCs.

3.3.3 MCMC

Now that we are able to interpolate quickly and generate LCs at any explosion time, redshift, attenuation, and combination of physical parameters, we are able to do the final step, obtain the posterior distribution of the model parameter given the data and a prior distribution using a Markov Chain Monte Carlo (MCMC) sampler that uses an affine invariant approach [28]. This method is evolved by moving one sampler (or walker) at a time, parallel Markov chains sample the posterior distribution by moving randomly in directions parallel to the relative positions of the walkers, i.e., if we consider one step of the ensemble Markov chain X (t) → X (t + 1) to consist of one cycle through all L walkers in the ensemble. Expressing this as a pseudo-code

```
for k = 1, ..., L:
    [
    update: X (t) →  X (t + 1)
    ]
```

Each walker X_k is updated using the current positions of all of the other walkers in the ensemble. The other walkers (besides itself) form the complementary ensemble, this means:

$$\vec{X}_k(t) = \{X_1(t+1), ..., X_{k-1}(t+1), X_{k+1}(t), ..., X_L(t)\}$$

And following acceptance rules that satisfy the condition of detailed balance for reversible Markov chains (see section 6.5 of [30]), this step can be accepted or not. The MCMC is implemented in python via emcee [29], and we interactively select the initial state to be around a set of physical parameters that replicate the rise of the SNe and the peak, to correctly constrain the explosion time. This step is done to ensure faster burn-in and avoid problems with convergence.

It's necessary to define the prior distributions, used in Table 3.1, where N (μ, σ) is a Gaussian distribution with mean μ and standard deviation σ, U (a, b) is a uniform distribution between a and b, and t_{exp0} is an initial guess of the explosion time of the SN. The prior probabilities are zero outside the intervals indicated.

There is also a variable scale parameter, which is standard in MCMC, to allow for errors in absolute calibrations, for which we use a Gaussian prior centered at 1.0 and with a standard deviation of 0.01 (1% errors). Finally, when running MCMC, we use 400 parallel walkers and 900 steps per sampler, with a burn-in period of 450 steps in all cases, just like [24].

Table 3.1: Prior parameters distribution

Parameter	Prior distribution	Units
t_{exp}	$N(t_{exp0}, 4)$	days
ln z	$N(\ln 0.18, 2)$, $z \in (10^{-3}, 1)$	
ln A_V	$N(\ln 0.05, 2)$, $A_V \in (10^{-4}, 10)$	ln mag
mass	$N(14, 3)$, mass $\in (12, 16)$	$M_\odot$
energy	$N(1, 1)$, energy $\in (0.5, 2)$	foe
$\log_{10} \dot{M}$	$U(-8, -2)$, $\log_{10} \dot{M} \in (-8, -2)$	$M_\odot$ yr^{-1}
r csm	$N(0.5, 1)$, r csm $\in (0.1, 1)$	10^{15} cm
β	$N(3, 2)$, $\beta \in (0, 5)$	

In order to improve the method of [24], a profiling of the algorithm was done, finding that the interpolation of the LCs was the most time-consuming part when executing it. So, we optimized this part using Numba [39], a just-in-time compiler for Python, making the method $\sim$ 6 times faster.

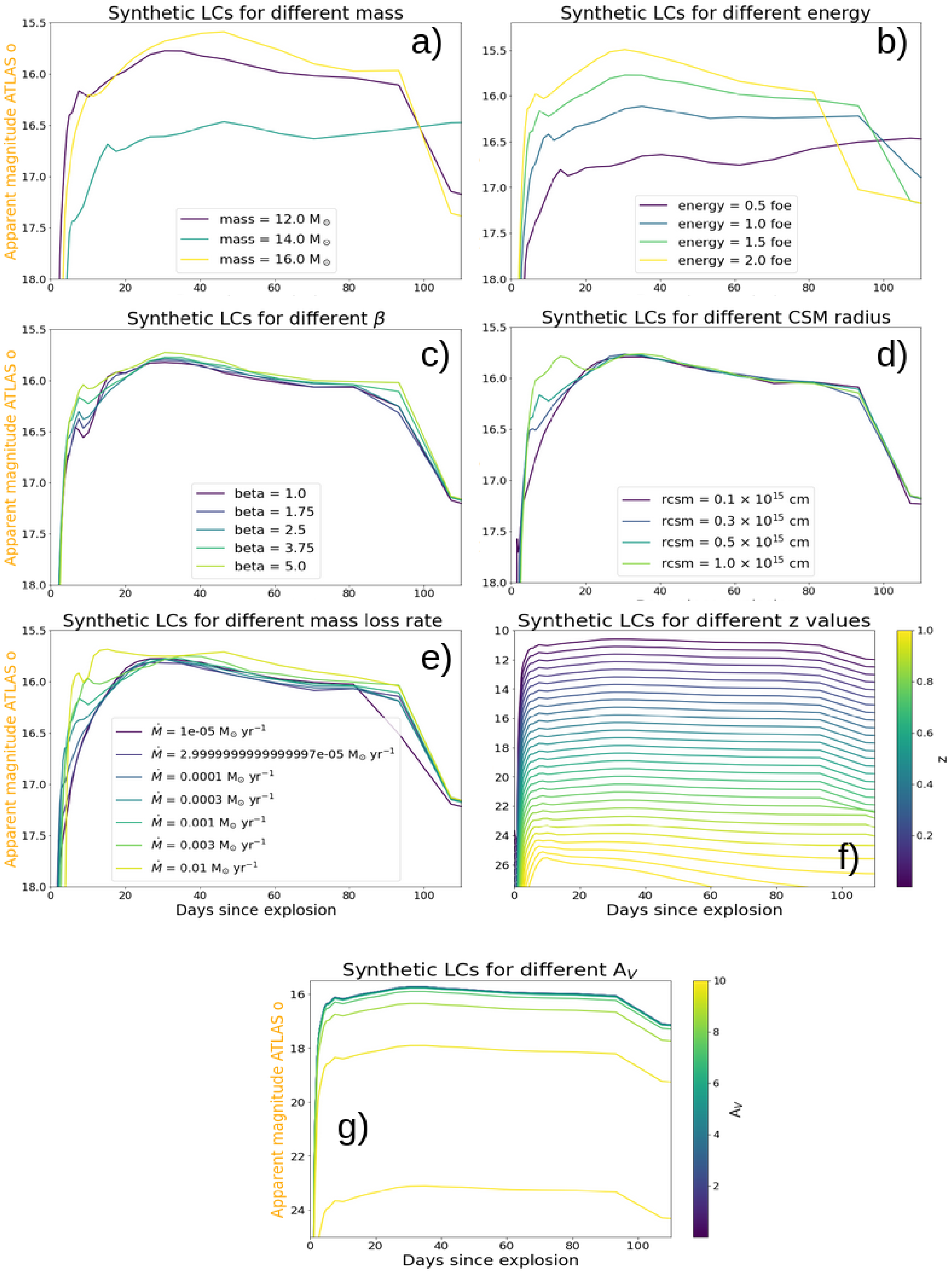

Figure 3.4: Synthetic LCs from [49] models for ATLAS o filter varying one parameter at a time, from a) to e) using the values from table 1.1. a) Varying the mass, b) the energy, c) the value of β, d) the radius of the CSM, e) the mass loss rate, f) the redshift logarithmically from 0.001 to 1, and f) A_V logarithmically from 10^{-4} to 10. The parameters that were not varied are fixed at mass of 12 $M_\odot$, energy of 1.5 foe, beta of 3.75, radius of the CSM 0.5 × 10^{15} cm, mass loss rate of 0.001 $M_\odot$ yr^{-1}

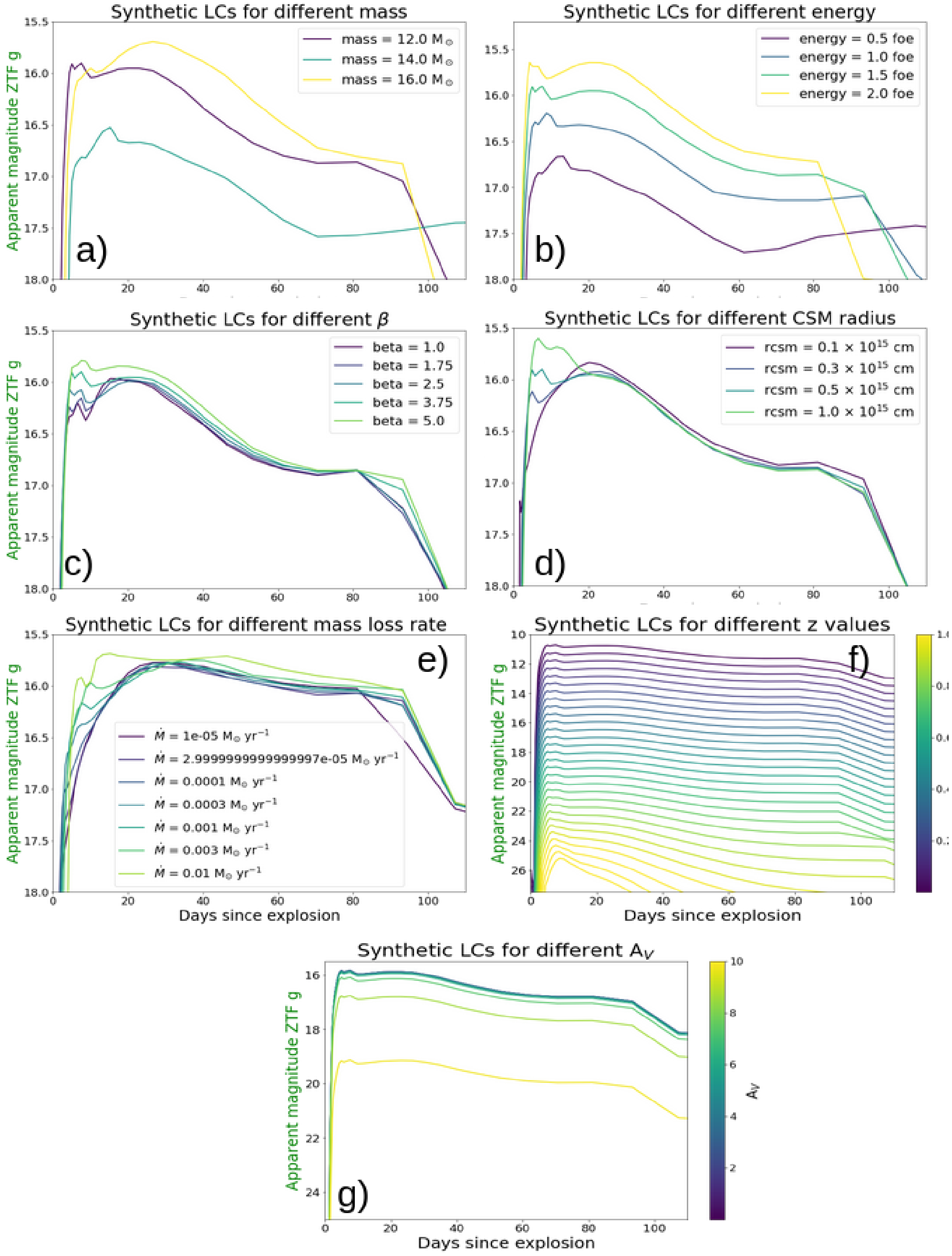

Figure 3.5: Same as Fig. 3.4 but for ZTF g$_{single}$ filter

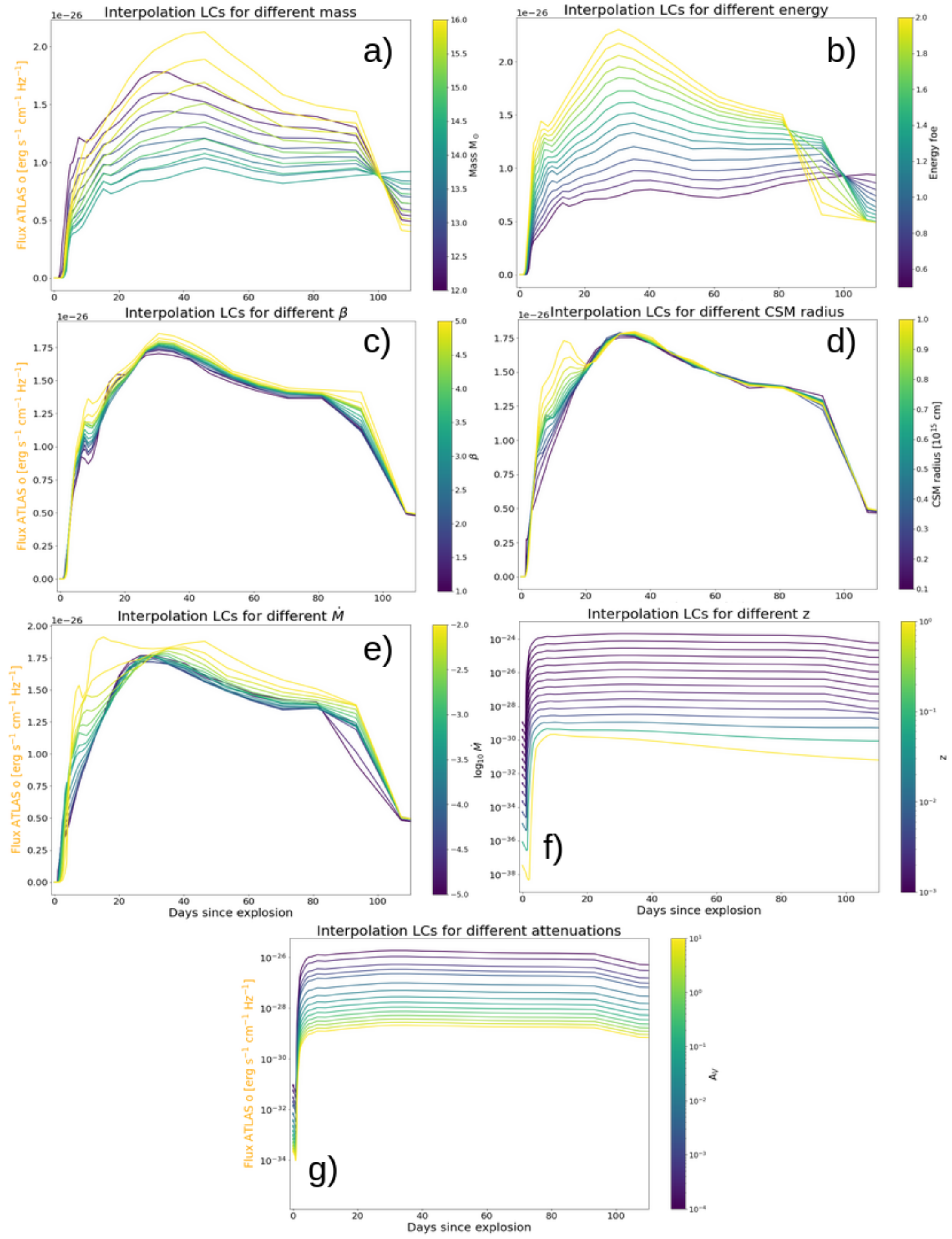

Figure 3.6: Interpolated flux LCs for ATLAS o filter varying one parameter at a time (Similar to 3.4), using 15 different values. a) Mass linearly between 12 and 16 M$_\odot$, b) energy linearly between 0.5 and 2, c) the value of β linearly between 1 and 5, d) the radius of the CSM linearly between 0.1 and 1, e) mass loss rate logarithmically between 10^{-5} and 10^{-2} M$_\odot$ yr^{-1}, f) the redshift logarithmically from 0.001 to 1 and y-axis in logarithmic scale, and f) A$_V$ logarithmically from 10^{-4} to 10 and y-axis in logarithmic scale. The parameters that were not varied are fixed at mass of 12 M$_\odot$, energy of 1.5 foe, beta of 3.75, radius of the CSM 0.5 $\times$ 10^{15} cm, mass loss rate of 0.001 M$_\odot$ yr^{-1}

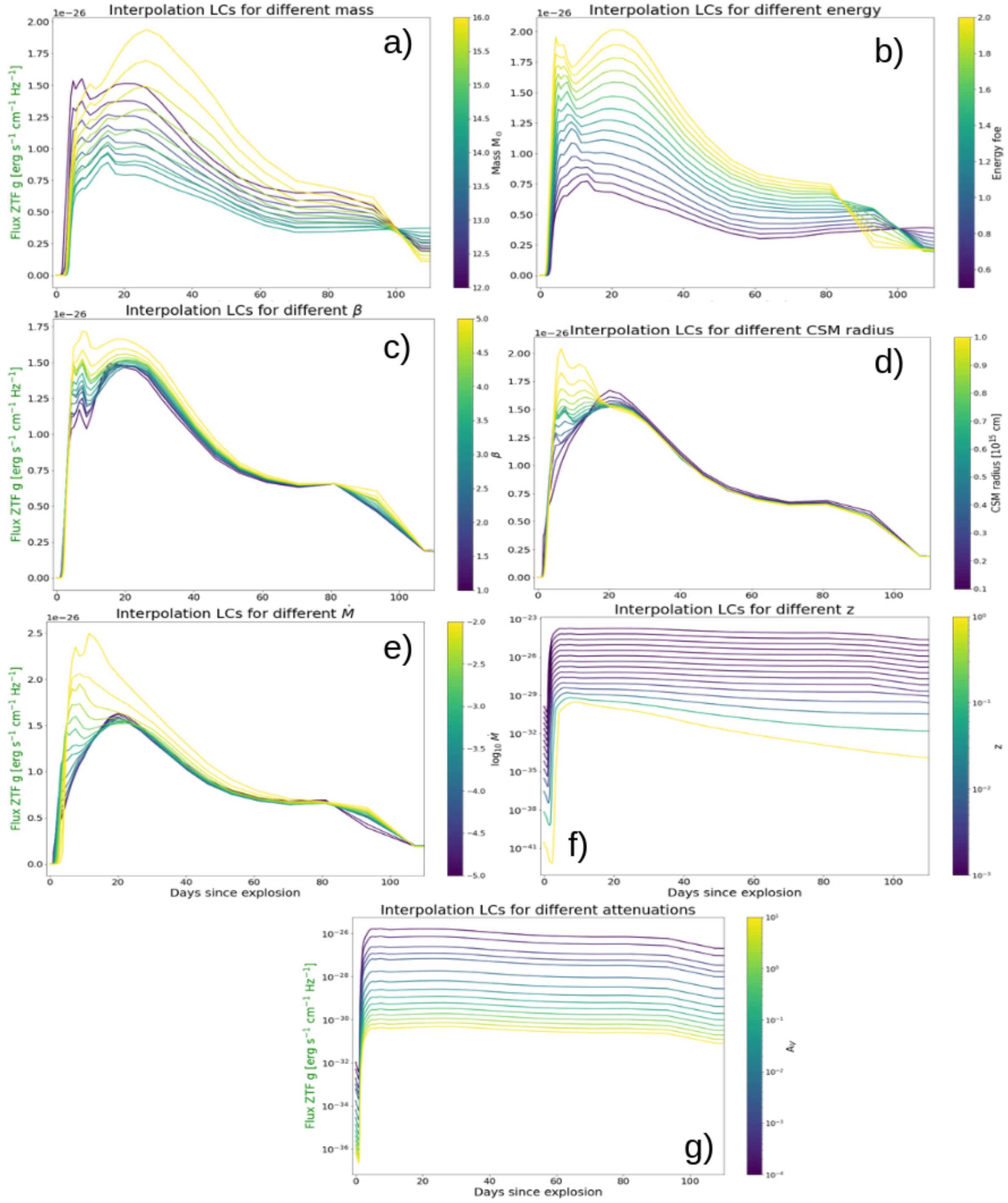

Figure 3.7: Same as Fig. 3.6 but for ZTF g_{single} filter

Chapter 4

Results

In this Chapter, we will present the results of this thesis. First, we will present the posterior distribution of the physical parameters inferred for a SN as an example of the results, then we will present the results obtained for the full sample, and lastly, we will compare our inferred redshift with redshifts of SN host galaxies.

4.1 Posterior distribution

Using the method described in section 3.3, we were able to obtain the posterior distribution of physical parameters for a sample of 186 SNe. The corner plot for the posterior distribution of SN 2019odf/ZTF19abqrhvy is shown as an example in Fig.4.1, alongside the LC of the object with 100 random LCs sampled from the posterior distribution (thin continuous lines). This can be used to visually inspect how the models fit the data. The explosion time for a given LC is plotted as a vertical grey line. In this case, all the adjusted parameters converge to a single-peaked multivariable distribution.

For every parameter, we take the median from the posterior distribution as a representative value and the 95 and 5 percentiles as upper and lower limits for this value respectively. We choose these values instead of the mean and standard deviation because not all posterior distributions are Gaussian and some posterior distribution are bimodal or multimodal. Thus, the median and percentiles give us more robust information about the distribution. We report this value for every SNe and every parameter in Table 4.1, where the median is reported and the upper and lower limits as the superscript and subscript respectively. The units for t_{exp}, mass, energy, $\dot{M}$, r_{CSM}, and A_V are Modified Julian date (MJD), $M_\odot$, foe, $M_\odot$ year^{-1}, 10^{15} cm, and mag respectively, β and z are unitless, and ZTF oid correspond to the ZTF object identifier.

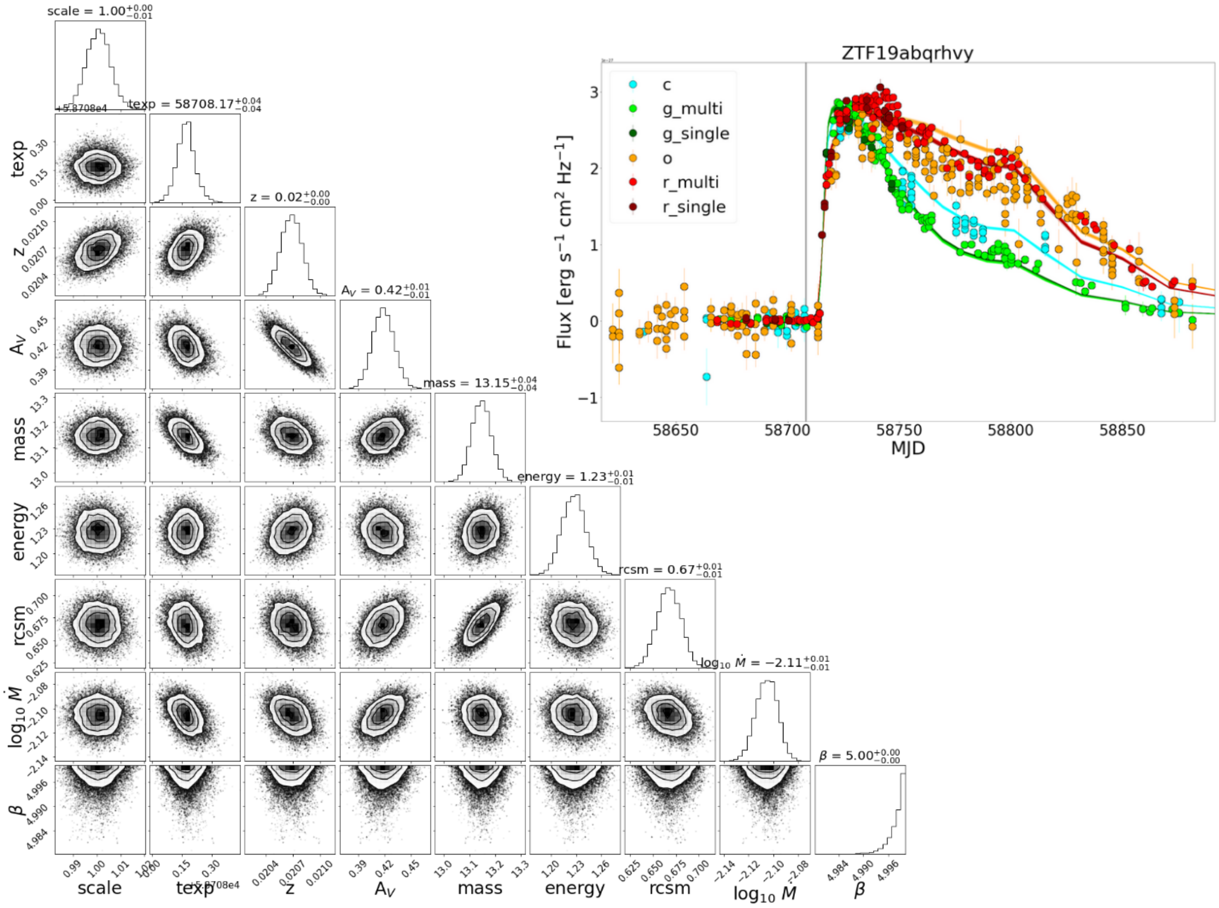

Figure 4.1: Bottom left corner: Corner plot of the posterior distribution of physical parameters obtained using our method for SN 2019odf/ZTF19abqrhvy. Top right corner: Observations of ZTF19abqrhvy (dots) and 100 random sampled from the posterior LCs (continuous lines). Explosion times are indicated as grey vertical lines.

Table 4.1: SNe posterior

ZTF oid	t_{exp}	mass	energy	$\dot{M}$	r_{csm}	β	A_V	z
ZTF18aatyqds	$58243.8^{+0.0}_{-0.0}$	$13.23^{+0.033}_{-0.035}$	$1.519^{+0.011}_{-0.011}$	$0.009^{+1.542}_{-5.124}$	$0.999^{+0.000}_{-0.000}$	$4.998^{+0.001}_{-0.003}$	$0.906^{+0.006}_{-0.006}$	$0.024^{+0.000}_{-0.000}$
ZTF18aawyjjq	$58256.9^{+0.2}_{-0.4}$	$12.22^{+0.969}_{-0.220}$	$1.151^{+0.567}_{-0.033}$	$0.009^{+2.957}_{-0.000}$	$0.947^{+0.011}_{-0.207}$	$3.751^{+1.247}_{-0.003}$	$0.983^{+0.040}_{-0.148}$	$0.029^{+0.001}_{-0.000}$
ZTF18abaeqpf	$59155.0^{+0.0}_{-0.4}$	$12.70^{+0.955}_{-0.024}$	$1.251^{+0.016}_{-0.075}$	$7.901^{+9.139}_{-6.371}$	$0.498^{+0.001}_{-0.006}$	$3.751^{+0.597}_{-0.003}$	$0.000^{+0.023}_{-0.000}$	$0.017^{+0.000}_{-0.000}$
ZTF18abckutn	$58283.7^{+0.1}_{-0.1}$	$12.01^{+0.112}_{-0.015}$	$1.108^{+0.034}_{-0.033}$	$0.009^{+0.000}_{-0.000}$	$0.828^{+0.045}_{-0.036}$	$4.921^{+0.066}_{-0.098}$	$0.821^{+0.034}_{-0.033}$	$0.034^{+0.000}_{-0.000}$
ZTF18abcpmwh	$58284.6^{+0.0}_{-0.0}$	$12.06^{+0.056}_{-0.043}$	$1.928^{+0.048}_{-0.060}$	$0.009^{+6.163}_{-0.000}$	$0.876^{+0.018}_{-0.016}$	$4.994^{+0.005}_{-0.020}$	$0.512^{+0.052}_{-0.039}$	$0.016^{+0.000}_{-0.000}$
ZTF18abcptmt	$58284.8^{+0.0}_{-0.0}$	$12.00^{+0.010}_{-0.002}$	$1.996^{+0.002}_{-0.011}$	$0.009^{+0.000}_{-0.000}$	$0.999^{+0.000}_{-0.001}$	$4.780^{+0.047}_{-0.046}$	$0.639^{+0.056}_{-0.046}$	$0.045^{+0.000}_{-0.000}$
ZTF18abeajml	$58297.1^{+0.0}_{-0.0}$	$12.00^{+0.003}_{-0.001}$	$1.999^{+0.000}_{-0.001}$	$0.009^{+3.694}_{-1.111}$	$0.999^{+6.362}_{-0.000}$	$3.750^{+0.001}_{-0.000}$	$0.354^{+0.013}_{-0.012}$	$0.035^{+0.000}_{-0.000}$
ZTF18abgladq	$58302.0^{+0.6}_{-0.9}$	$12.01^{+0.061}_{-0.011}$	$1.042^{+0.925}_{-0.525}$	$0.009^{+0.000}_{-0.000}$	$0.999^{+0.000}_{-0.003}$	$3.751^{+0.037}_{-0.040}$	$0.317^{+0.183}_{-0.056}$	$0.027^{+0.006}_{-0.006}$
ZTF18abmdpwe	$58333.9^{+0.0}_{-0.0}$	$12.00^{+0.005}_{-0.001}$	$1.712^{+0.013}_{-0.014}$	$0.008^{+0.000}_{-0.000}$	$0.999^{+0.000}_{-0.001}$	$4.998^{+0.001}_{-0.004}$	$1.142^{+0.017}_{-0.018}$	$0.014^{+0.000}_{-0.000}$
ZTF18abokyfk	$58344.8^{+0.0}_{-0.0}$	$13.05^{+0.080}_{-0.083}$	$1.796^{+0.018}_{-0.017}$	$0.009^{+0.000}_{-0.000}$	$0.947^{+0.009}_{-0.010}$	$4.998^{+0.001}_{-0.004}$	$1.316^{+0.012}_{-0.011}$	$0.015^{+0.000}_{-0.000}$
ZTF18abqyvzy	$58352.9^{+0.0}_{-0.0}$	$12.30^{+0.029}_{-0.029}$	$1.928^{+0.010}_{-0.009}$	$0.009^{+9.419}_{-3.466}$	$0.999^{+5.833}_{-0.000}$	$4.999^{+6.408}_{-0.000}$	$1.018^{+0.004}_{-0.004}$	$0.012^{+6.466}_{-6.123}$
ZTF18absclsr	$58349.4^{+0.0}_{-0.0}$	$12.00^{+0.005}_{-0.001}$	$1.998^{+0.001}_{-0.004}$	$0.009^{+1.550}_{-5.413}$	$0.999^{+0.000}_{-0.000}$	$4.996^{+0.003}_{-0.008}$	$0.826^{+0.012}_{-0.013}$	$0.023^{+0.000}_{-0.000}$
ZTF18absldfl	$58357.7^{+0.1}_{-0.1}$	$12.00^{+0.022}_{-0.006}$	$1.985^{+0.013}_{-0.035}$	$0.007^{+0.000}_{-0.000}$	$0.999^{+0.000}_{-0.001}$	$3.749^{+0.034}_{-0.031}$	$0.819^{+0.020}_{-0.019}$	$0.032^{+0.000}_{-0.000}$
ZTF18abvmlow	$58477.8^{+0.0}_{-0.0}$	$12.00^{+0.017}_{-0.004}$	$1.625^{+0.038}_{-0.040}$	$0.001^{+6.697}_{-6.371}$	$0.999^{+0.000}_{-0.000}$	$4.994^{+0.004}_{-0.020}$	$0.274^{+0.012}_{-0.012}$	$0.014^{+0.000}_{-0.000}$
ZTF18acbvhit	$58402.9^{+0.1}_{-0.1}$	$15.41^{+0.166}_{-0.130}$	$1.000^{+0.004}_{-0.004}$	$0.000^{+6.283}_{-5.620}$	$0.998^{+0.001}_{-0.005}$	$3.749^{+0.037}_{-0.055}$	$0.947^{+0.021}_{-0.022}$	$0.014^{+0.000}_{-0.000}$
ZTF18achtnvk	$58427.7^{+0.0}_{-0.1}$	$12.01^{+0.053}_{-0.015}$	$1.996^{+0.003}_{-0.010}$	$0.008^{+0.001}_{-0.000}$	$0.966^{+0.018}_{-0.021}$	$4.842^{+0.133}_{-0.216}$	$1.182^{+0.066}_{-0.059}$	$0.033^{+0.001}_{-0.001}$
ZTF18acqwdla	$58439.0^{+0.0}_{-0.0}$	$12.73^{+0.066}_{-0.068}$	$1.099^{+0.008}_{-0.007}$	$0.009^{+5.155}_{-2.009}$	$0.999^{+8.130}_{-0.000}$	$3.750^{+0.002}_{-0.002}$	$0.752^{+0.022}_{-0.033}$	$0.016^{+0.000}_{-0.000}$
ZTF18acrtvmm	$58442.5^{+0.3}_{-0.7}$	$12.89^{+0.293}_{-0.339}$	$1.015^{+0.040}_{-0.050}$	$0.009^{+0.000}_{-0.001}$	$0.914^{+0.031}_{-0.028}$	$3.326^{+0.647}_{-0.871}$	$0.728^{+0.063}_{-0.108}$	$0.019^{+0.000}_{-0.000}$
ZTF18acvgyst	$58447.9^{+1.1}_{-0.2}$	$13.25^{+0.376}_{-0.530}$	$1.067^{+0.121}_{-0.138}$	$0.000^{+0.005}_{-0.000}$	$0.729^{+0.169}_{-0.617}$	$4.155^{+0.823}_{-1.648}$	$0.064^{+0.166}_{-0.061}$	$0.027^{+0.001}_{-0.001}$
ZTF18adbacau	$58471.3^{+1.9}_{-0.4}$	$14.35^{+0.163}_{-0.404}$	$1.728^{+0.141}_{-0.550}$	$0.001^{+0.006}_{-0.000}$	$0.488^{+0.288}_{-0.151}$	$4.980^{+0.018}_{-0.948}$	$0.297^{+0.314}_{-0.050}$	$0.030^{+0.001}_{-0.002}$
ZTF18adbclkd	$58470.1^{+0.5}_{-1.7}$	$12.64^{+1.027}_{-0.302}$	$0.959^{+0.038}_{-0.293}$	$0.007^{+0.001}_{-0.004}$	$0.522^{+0.258}_{-0.040}$	$4.722^{+0.262}_{-0.205}$	$0.389^{+0.293}_{-0.052}$	$0.015^{+0.000}_{-0.001}$
ZTF19aadnxog	$58492.4^{+0.0}_{-0.0}$	$15.11^{+0.077}_{-0.076}$	$0.697^{+0.005}_{-0.005}$	$0.007^{+0.000}_{-0.000}$	$0.999^{+8.587}_{-0.000}$	$4.731^{+0.036}_{-0.037}$	$0.707^{+0.026}_{-0.024}$	$0.012^{+9.571}_{-9.915}$
ZTF19aakssnv	$58514.7^{+0.3}_{-0.2}$	$14.08^{+0.112}_{-0.093}$	$1.003^{+0.033}_{-0.042}$	$0.003^{+0.000}_{-0.000}$	$0.819^{+0.025}_{-0.023}$	$2.870^{+0.246}_{-0.137}$	$0.165^{+0.060}_{-0.053}$	$0.025^{+0.000}_{-0.000}$
ZTF19aallimd	$58535.0^{+0.1}_{-0.1}$	$12.56^{+0.105}_{-0.096}$	$1.134^{+0.024}_{-0.023}$	$0.009^{+0.000}_{-0.000}$	$0.500^{+0.004}_{-0.004}$	$3.749^{+0.039}_{-0.040}$	$0.244^{+0.023}_{-0.023}$	$0.015^{+0.000}_{-0.000}$
ZTF19aalsnbp	$58534.7^{+0.2}_{-0.0}$	$12.90^{+0.125}_{-0.283}$	$1.097^{+0.019}_{-0.009}$	$0.009^{+3.351}_{-0.000}$	$0.999^{+0.000}_{-0.002}$	$3.749^{+0.054}_{-0.089}$	$0.689^{+0.061}_{-0.077}$	$0.037^{+0.000}_{-0.000}$
ZTF19aamggnw	$58537.6^{+0.4}_{-0.9}$	$12.20^{+0.259}_{-0.180}$	$1.082^{+0.036}_{-0.035}$	$0.001^{+0.008}_{-0.000}$	$0.970^{+0.028}_{-0.499}$	$3.591^{+0.407}_{-1.156}$	$0.017^{+0.046}_{-0.015}$	$0.032^{+0.000}_{-0.000}$
ZTF19aamhmsx	$58540.0^{+2.0}_{-0.7}$	$15.18^{+0.495}_{-1.054}$	$1.032^{+0.264}_{-0.071}$	$0.009^{+0.000}_{-0.004}$	$0.893^{+0.046}_{-0.048}$	$4.949^{+0.047}_{-1.147}$	$0.455^{+0.152}_{-0.302}$	$0.035^{+0.001}_{-0.001}$
ZTF19aamkfvy	$58549.1^{+1.9}_{-0.3}$	$12.80^{+0.177}_{-0.787}$	$1.289^{+0.306}_{-0.033}$	$0.006^{+0.000}_{-0.002}$	$0.993^{+0.005}_{-0.041}$	$4.944^{+0.051}_{-0.691}$	$0.975^{+0.052}_{-0.148}$	$0.026^{+0.002}_{-0.000}$
ZTF19aamljom	$58548.9^{+0.0}_{-0.0}$	$13.19^{+0.030}_{-0.028}$	$1.566^{+0.008}_{-0.008}$	$0.009^{+7.936}_{-1.390}$	$0.999^{+8.424}_{-0.000}$	$4.998^{+0.000}_{-0.004}$	$0.015^{+0.005}_{-0.010}$	$0.019^{+0.000}_{-0.000}$

ZTF19aamowaf	$58512.4^{+1.2}_{-0.2}$	$14.07^{+0.160}_{-0.093}$	$1.990^{+0.009}_{-0.102}$	$0.006^{+0.000}_{-0.005}$	$0.843^{+0.031}_{-0.028}$	$3.750^{+1.244}_{-0.031}$	$0.005^{+0.033}_{-0.004}$	$0.026^{+0.000}_{-0.000}$
ZTF19aamtwiz	$58552.4^{+0.4}_{-0.3}$	$12.63^{+0.348}_{-0.233}$	$1.158^{+0.069}_{-0.040}$	$0.009^{+0.000}_{-0.000}$	$0.799^{+0.048}_{-0.082}$	$4.992^{+0.007}_{-0.047}$	$0.264^{+0.041}_{-0.073}$	$0.040^{+0.001}_{-0.000}$
ZTF19aamwhat	$58543.2^{+0.3}_{-0.4}$	$15.91^{+0.080}_{-1.246}$	$0.689^{+0.335}_{-0.014}$	$0.003^{+0.006}_{-0.000}$	$0.300^{+0.140}_{-0.003}$	$3.749^{+0.010}_{-1.246}$	$0.895^{+0.026}_{-0.166}$	$0.011^{+0.001}_{-0.000}$
ZTF19aanhhal	$58557.1^{+0.1}_{-1.5}$	$12.29^{+2.298}_{-0.097}$	$1.149^{+0.027}_{-0.152}$	$0.007^{+0.000}_{-0.000}$	$0.504^{+0.387}_{-0.023}$	$4.497^{+0.191}_{-0.458}$	$0.276^{+0.341}_{-0.028}$	$0.026^{+0.000}_{-0.002}$
ZTF19aaniore	$58557.9^{+0.2}_{-0.2}$	$15.96^{+0.029}_{-0.097}$	$0.696^{+0.011}_{-0.009}$	$0.005^{+0.000}_{-0.000}$	$0.820^{+0.022}_{-0.024}$	$3.730^{+0.112}_{-0.087}$	$0.693^{+0.056}_{-0.055}$	$0.024^{+0.000}_{-0.000}$
ZTF19aanlekq	$58557.3^{+0.1}_{-0.9}$	$12.00^{+0.008}_{-0.002}$	$1.866^{+0.112}_{-0.019}$	$0.009^{+4.369}_{-6.306}$	$0.999^{+0.000}_{-0.002}$	$3.750^{+1.160}_{-0.002}$	$0.776^{+0.012}_{-0.089}$	$0.031^{+0.002}_{-0.000}$
ZTF19aanovps	$58559.7^{+0.2}_{-1.8}$	$13.94^{+1.542}_{-0.314}$	$1.116^{+0.065}_{-0.476}$	$0.006^{+0.000}_{-0.002}$	$0.746^{+0.186}_{-0.059}$	$3.805^{+0.680}_{-0.115}$	$1.007^{+0.058}_{-0.050}$	$0.020^{+0.000}_{-0.000}$
ZTF19aanrrqu	$58562.7^{+0.0}_{-0.0}$	$12.00^{+0.004}_{-0.001}$	$1.999^{+0.000}_{-0.001}$	$0.009^{+4.632}_{-1.532}$	$0.999^{+8.528}_{-0.000}$	$3.750^{+0.002}_{-0.002}$	$0.430^{+0.027}_{-0.025}$	$0.024^{+0.000}_{-0.000}$
ZTF19aapafit	$58573.6^{+0.0}_{-0.0}$	$12.00^{+0.007}_{-0.002}$	$0.923^{+0.005}_{-0.004}$	$0.000^{+3.756}_{-3.032}$	$0.944^{+0.017}_{-0.021}$	$3.750^{+0.008}_{-0.007}$	$0.017^{+0.016}_{-0.004}$	$0.019^{+0.000}_{-0.000}$
ZTF19aapbfot	$58570.6^{+0.2}_{-0.2}$	$15.33^{+0.426}_{-0.416}$	$1.659^{+0.067}_{-0.091}$	$0.009^{+0.000}_{-0.001}$	$0.982^{+0.015}_{-0.028}$	$4.966^{+0.030}_{-0.123}$	$0.882^{+0.047}_{-0.168}$	$0.036^{+0.001}_{-0.001}$
ZTF19aaqdkrm	$58579.0^{+0.2}_{-0.1}$	$12.21^{+0.201}_{-0.173}$	$1.996^{+0.003}_{-0.010}$	$0.009^{+0.000}_{-0.000}$	$0.997^{+0.001}_{-0.007}$	$3.752^{+0.087}_{-0.064}$	$0.190^{+0.049}_{-0.063}$	$0.039^{+0.000}_{-0.000}$
ZTF19aaqxosb	$58584.2^{+0.2}_{-0.1}$	$12.02^{+0.095}_{-0.027}$	$1.245^{+0.041}_{-0.040}$	$0.001^{+0.000}_{-0.000}$	$0.997^{+0.002}_{-0.006}$	$4.868^{+0.122}_{-1.169}$	$0.845^{+0.036}_{-0.034}$	$0.022^{+0.000}_{-0.000}$
ZTF19aariwfe	$58589.6^{+0.7}_{-0.8}$	$12.35^{+0.462}_{-0.312}$	$1.616^{+0.083}_{-0.079}$	$0.003^{+0.002}_{-0.001}$	$0.947^{+0.042}_{-0.063}$	$4.300^{+0.651}_{-0.786}$	$0.239^{+0.111}_{-0.127}$	$0.036^{+0.001}_{-0.002}$
ZTF19aarjfqe	$58588.2^{+1.0}_{-0.5}$	$12.94^{+1.155}_{-0.522}$	$1.665^{+0.166}_{-0.467}$	$0.007^{+0.001}_{-0.005}$	$0.804^{+0.192}_{-0.077}$	$4.972^{+0.025}_{-0.117}$	$0.363^{+0.173}_{-0.131}$	$0.028^{+0.001}_{-0.001}$
ZTF19aatlqdf	$58593.6^{+0.7}_{-0.3}$	$15.58^{+0.362}_{-0.620}$	$0.570^{+0.072}_{-0.048}$	$0.006^{+0.000}_{-0.000}$	$0.805^{+0.042}_{-0.051}$	$4.794^{+0.179}_{-0.338}$	$0.208^{+0.055}_{-0.088}$	$0.032^{+0.001}_{-0.001}$
ZTF19aaugaam	$58604.2^{+0.3}_{-0.2}$	$12.02^{+0.077}_{-0.021}$	$1.973^{+0.024}_{-0.085}$	$0.007^{+0.001}_{-0.006}$	$0.624^{+0.065}_{-0.035}$	$4.974^{+0.023}_{-0.108}$	$0.259^{+0.041}_{-0.129}$	$0.032^{+0.000}_{-0.000}$
ZTF19aauishy	$58606.8^{+0.4}_{-0.3}$	$12.02^{+0.108}_{-0.023}$	$0.963^{+0.046}_{-0.054}$	$0.000^{+0.000}_{-0.000}$	$0.991^{+0.008}_{-0.043}$	$1.732^{+0.262}_{-0.525}$	$0.255^{+0.068}_{-0.047}$	$0.029^{+0.001}_{-0.001}$
ZTF19aauqwna	$58608.9^{+0.0}_{-0.0}$	$12.02^{+0.069}_{-0.021}$	$1.997^{+0.002}_{-0.009}$	$0.009^{+8.286}_{-0.000}$	$0.998^{+0.001}_{-0.004}$	$4.990^{+0.008}_{-0.020}$	$1.068^{+0.023}_{-0.023}$	$0.031^{+0.000}_{-0.000}$
ZTF19aavbjfp	$58612.8^{+1.1}_{-0.1}$	$12.81^{+0.220}_{-0.714}$	$1.628^{+0.061}_{-0.049}$	$0.002^{+0.000}_{-0.001}$	$0.842^{+0.150}_{-0.056}$	$3.749^{+0.035}_{-0.055}$	$0.199^{+0.041}_{-0.093}$	$0.033^{+0.002}_{-0.001}$
ZTF19aavhblr	$58612.0^{+0.2}_{-0.3}$	$12.02^{+0.066}_{-0.022}$	$1.808^{+0.153}_{-0.112}$	$0.009^{+0.000}_{-0.000}$	$0.998^{+0.001}_{-0.003}$	$3.776^{+0.878}_{-0.137}$	$0.274^{+0.065}_{-0.116}$	$0.046^{+0.003}_{-0.002}$
ZTF19aavkptg	$58613.9^{+0.6}_{-0.8}$	$13.08^{+0.589}_{-0.581}$	$1.068^{+0.246}_{-0.215}$	$0.003^{+0.001}_{-0.000}$	$0.967^{+0.028}_{-0.057}$	$3.997^{+0.891}_{-1.009}$	$0.133^{+0.138}_{-0.084}$	$0.041^{+0.003}_{-0.004}$
ZTF19aavrcew	$58622.1^{+0.0}_{-0.0}$	$12.00^{+0.010}_{-0.002}$	$1.995^{+0.003}_{-0.013}$	$0.009^{+0.000}_{-0.000}$	$0.998^{+0.000}_{-0.003}$	$4.980^{+0.017}_{-0.047}$	$0.787^{+0.018}_{-0.018}$	$0.019^{+0.000}_{-0.000}$
ZTF19aawgxdn	$58628.6^{+0.0}_{-0.0}$	$12.00^{+0.005}_{-0.001}$	$0.832^{+0.011}_{-0.011}$	$0.007^{+0.000}_{-0.000}$	$0.515^{+0.004}_{-0.003}$	$3.750^{+0.005}_{-0.004}$	$0.725^{+0.028}_{-0.026}$	$0.022^{+0.000}_{-0.000}$
ZTF19aaycrgf	$58623.3^{+4.3}_{-0.7}$	$13.58^{+0.223}_{-0.207}$	$0.737^{+0.408}_{-0.079}$	$0.003^{+0.002}_{-0.001}$	$0.534^{+0.315}_{-0.081}$	$4.811^{+0.170}_{-0.494}$	$0.577^{+0.100}_{-0.063}$	$0.017^{+0.000}_{-0.000}$
ZTF19aaydtur	$58635.6^{+0.2}_{-0.2}$	$12.50^{+0.356}_{-0.293}$	$0.844^{+0.091}_{-0.090}$	$0.002^{+0.000}_{-0.000}$	$0.835^{+0.066}_{-0.063}$	$3.750^{+0.100}_{-0.159}$	$0.148^{+0.087}_{-0.073}$	$0.030^{+0.001}_{-0.001}$
ZTF19aazfvhh	$58640.6^{+0.3}_{-0.3}$	$12.02^{+0.115}_{-0.027}$	$1.194^{+0.021}_{-0.018}$	$0.006^{+0.000}_{-0.001}$	$0.641^{+0.118}_{-0.172}$	$4.152^{+0.694}_{-0.529}$	$0.710^{+0.095}_{-0.110}$	$0.033^{+0.000}_{-0.001}$
ZTF19aazyvub	$58644.3^{+0.2}_{-0.4}$	$12.94^{+0.324}_{-0.356}$	$1.311^{+0.041}_{-0.041}$	$0.000^{+0.000}_{-0.000}$	$0.998^{+0.000}_{-0.005}$	$4.838^{+0.150}_{-0.799}$	$0.003^{+0.014}_{-0.002}$	$0.030^{+0.000}_{-0.000}$
ZTF19abajxet	$58651.5^{+0.0}_{-0.8}$	$12.37^{+0.094}_{-0.377}$	$1.617^{+0.009}_{-0.085}$	$0.002^{+0.007}_{-9.415}$	$0.963^{+0.011}_{-0.151}$	$4.998^{+0.001}_{-0.181}$	$0.284^{+0.155}_{-0.013}$	$0.014^{+0.000}_{-0.000}$
ZTF19abbwfgp	$58654.6^{+0.9}_{-0.0}$	$13.16^{+0.075}_{-0.877}$	$1.582^{+0.080}_{-0.020}$	$0.009^{+5.290}_{-0.001}$	$0.961^{+0.009}_{-0.069}$	$4.999^{+0.000}_{-0.013}$	$0.425^{+0.020}_{-0.126}$	$0.021^{+0.000}_{-0.000}$
ZTF19abcekty	$58648.9^{+0.0}_{-0.0}$	$12.00^{+0.001}_{-0.000}$	$1.999^{+0.000}_{-0.000}$	$0.009^{+4.104}_{-1.455}$	$0.999^{+4.348}_{-0.000}$	$4.931^{+0.022}_{-0.023}$	$0.369^{+0.013}_{-0.012}$	$0.015^{+0.000}_{-0.000}$
ZTF19abgiwkt	$58672.2^{+0.1}_{-0.2}$	$13.71^{+0.663}_{-0.173}$	$1.136^{+0.038}_{-0.309}$	$0.004^{+0.001}_{-0.000}$	$0.751^{+0.129}_{-0.049}$	$3.474^{+0.283}_{-0.985}$	$1.235^{+0.043}_{-0.052}$	$0.010^{+0.000}_{-0.000}$
ZTF19abjbtbm	$58689.0^{+0.1}_{-0.0}$	$12.76^{+0.152}_{-0.218}$	$0.516^{+0.040}_{-0.014}$	$0.000^{+9.200}_{-0.000}$	$0.302^{+0.115}_{-0.050}$	$4.033^{+0.881}_{-0.713}$	$0.002^{+0.007}_{-0.002}$	$0.016^{+0.000}_{-0.000}$

ZTF19abjpntj	$58686.1^{+1.0}_{-0.6}$	$13.65^{+0.701}_{-0.406}$	$1.273^{+0.135}_{-0.095}$	$0.004^{+0.002}_{-0.002}$	$0.700^{+0.070}_{-0.095}$	$4.526^{+0.419}_{-1.009}$	$0.594^{+0.137}_{-0.457}$	$0.030^{+0.006}_{-0.001}$
ZTF19abjrjdw	$58688.5^{+0.2}_{-1.0}$	$12.36^{+1.241}_{-0.246}$	$1.585^{+0.062}_{-0.123}$	$0.006^{+0.002}_{-0.002}$	$0.888^{+0.082}_{-0.043}$	$4.861^{+0.129}_{-0.582}$	$1.108^{+0.107}_{-0.064}$	$0.018^{+0.000}_{-0.000}$
ZTF19abpyqog	$58705.6^{+0.0}_{-0.0}$	$12.26^{+0.142}_{-0.135}$	$1.985^{+0.013}_{-0.036}$	$0.006^{+0.000}_{-0.000}$	$0.934^{+0.013}_{-0.013}$	$3.751^{+0.052}_{-0.040}$	$0.849^{+0.026}_{-0.024}$	$0.037^{+0.000}_{-0.000}$
ZTF19abqgtqo	$58707.5^{+0.3}_{-0.2}$	$14.06^{+0.218}_{-0.117}$	$1.667^{+0.077}_{-0.064}$	$0.000^{+0.000}_{-0.000}$	$0.799^{+0.029}_{-0.044}$	$3.749^{+0.038}_{-0.037}$	$0.272^{+0.031}_{-0.027}$	$0.033^{+0.000}_{-0.000}$
ZTF19abqhobb	$58709.7^{+0.1}_{-0.1}$	$12.17^{+0.148}_{-0.123}$	$1.605^{+0.019}_{-0.017}$	$0.001^{+8.073}_{-7.041}$	$0.996^{+0.002}_{-0.004}$	$4.989^{+0.009}_{-0.022}$	$0.434^{+0.015}_{-0.015}$	$0.017^{+0.000}_{-0.000}$
ZTF19abqrhvt	$58706.2^{+0.1}_{-0.0}$	$12.00^{+0.010}_{-0.003}$	$1.998^{+0.000}_{-0.002}$	$0.009^{+2.074}_{-5.567}$	$0.999^{+0.000}_{-0.001}$	$4.993^{+0.005}_{-0.012}$	$0.102^{+0.025}_{-0.019}$	$0.025^{+0.000}_{-0.000}$
ZTF19abqrhvy	$58708.1^{+0.0}_{-0.0}$	$13.14^{+0.062}_{-0.061}$	$1.226^{+0.023}_{-0.022}$	$0.007^{+0.000}_{-0.000}$	$0.667^{+0.021}_{-0.021}$	$4.998^{+0.001}_{-0.004}$	$0.417^{+0.020}_{-0.020}$	$0.020^{+0.000}_{-0.000}$
ZTF19abrbmvt	$58713.3^{+0.3}_{-0.9}$	$12.65^{+0.762}_{-0.306}$	$1.375^{+0.082}_{-0.108}$	$0.000^{+0.000}_{-0.000}$	$0.970^{+0.027}_{-0.072}$	$4.970^{+0.027}_{-0.105}$	$0.324^{+0.149}_{-0.049}$	$0.035^{+0.001}_{-0.002}$
ZTF19abudjie	$58715.5^{+0.4}_{-0.5}$	$15.47^{+0.159}_{-0.102}$	$1.409^{+0.069}_{-0.156}$	$0.003^{+0.001}_{-0.000}$	$0.500^{+0.025}_{-0.009}$	$4.990^{+0.008}_{-0.556}$	$1.242^{+0.055}_{-0.067}$	$0.022^{+0.000}_{-0.000}$
ZTF19abueupg	$58716.6^{+2.6}_{-0.1}$	$13.94^{+0.069}_{-0.776}$	$1.472^{+0.037}_{-0.460}$	$0.009^{+7.492}_{-0.006}$	$0.881^{+0.097}_{-0.030}$	$4.796^{+0.128}_{-0.468}$	$0.817^{+0.031}_{-0.198}$	$0.030^{+0.000}_{-0.000}$
ZTF19abukbit	$58714.5^{+0.8}_{-0.8}$	$12.23^{+0.556}_{-0.213}$	$1.346^{+0.101}_{-0.091}$	$0.001^{+0.001}_{-0.000}$	$0.989^{+0.009}_{-0.042}$	$4.307^{+0.654}_{-1.314}$	$0.340^{+0.221}_{-0.148}$	$0.047^{+0.004}_{-0.003}$
ZTF19abwamby	$58723.5^{+0.1}_{-0.1}$	$12.03^{+0.104}_{-0.031}$	$1.888^{+0.101}_{-0.229}$	$0.006^{+0.000}_{-0.000}$	$0.998^{+0.001}_{-0.004}$	$3.749^{+0.084}_{-0.084}$	$0.293^{+0.053}_{-0.042}$	$0.043^{+0.001}_{-0.002}$
ZTF19abwsagv	$58726.0^{+0.0}_{-0.1}$	$12.00^{+0.025}_{-0.005}$	$1.996^{+0.003}_{-0.014}$	$0.007^{+0.000}_{-0.000}$	$0.597^{+0.034}_{-0.026}$	$4.971^{+0.026}_{-0.082}$	$0.005^{+0.016}_{-0.004}$	$0.041^{+0.000}_{-0.000}$
ZTF19abwztsb	$58723.8^{+0.2}_{-0.1}$	$14.03^{+0.058}_{-0.033}$	$1.994^{+0.005}_{-0.021}$	$0.009^{+0.000}_{-0.000}$	$0.738^{+0.012}_{-0.015}$	$4.084^{+0.089}_{-0.078}$	$0.824^{+0.012}_{-0.012}$	$0.010^{+0.000}_{-0.000}$
ZTF19abzrdup	$58736.9^{+1.2}_{-4.7}$	$13.43^{+0.066}_{-0.107}$	$1.923^{+0.069}_{-0.654}$	$0.004^{+0.004}_{-0.001}$	$0.498^{+0.009}_{-0.395}$	$4.918^{+0.073}_{-0.151}$	$0.004^{+0.010}_{-0.003}$	$0.037^{+0.000}_{-0.000}$
ZTF19acbhvgi	$58744.0^{+0.4}_{-0.6}$	$14.86^{+0.527}_{-0.854}$	$1.072^{+0.042}_{-0.037}$	$0.002^{+0.001}_{-0.000}$	$0.997^{+0.002}_{-0.014}$	$4.173^{+0.796}_{-0.605}$	$0.103^{+0.115}_{-0.062}$	$0.035^{+0.001}_{-0.001}$
ZTF19acbrzzr	$58749.5^{+0.3}_{-1.0}$	$15.05^{+0.617}_{-0.531}$	$0.971^{+0.124}_{-0.124}$	$0.009^{+0.000}_{-0.001}$	$0.850^{+0.040}_{-0.044}$	$2.525^{+0.798}_{-0.211}$	$0.557^{+0.159}_{-0.119}$	$0.027^{+0.001}_{-0.001}$
ZTF19acbvisk	$58746.1^{+1.0}_{-0.8}$	$13.24^{+0.463}_{-0.432}$	$1.095^{+0.036}_{-0.033}$	$0.007^{+0.002}_{-0.003}$	$0.908^{+0.037}_{-0.046}$	$2.769^{+1.402}_{-0.406}$	$0.219^{+0.150}_{-0.145}$	$0.035^{+0.002}_{-0.002}$
ZTF19acchaza	$58751.8^{+0.1}_{-0.0}$	$12.01^{+0.037}_{-0.010}$	$1.995^{+0.004}_{-0.012}$	$0.009^{+4.757}_{-0.000}$	$0.999^{+0.000}_{-0.001}$	$2.496^{+0.027}_{-0.757}$	$0.471^{+0.082}_{-0.074}$	$0.044^{+0.001}_{-0.001}$
ZTF19acewuwn	$58768.1^{+0.3}_{-0.5}$	$12.04^{+0.156}_{-0.040}$	$0.951^{+0.048}_{-0.049}$	$0.003^{+0.000}_{-0.002}$	$0.500^{+0.038}_{-0.019}$	$1.066^{+0.694}_{-0.061}$	$0.231^{+0.046}_{-0.052}$	$0.031^{+0.001}_{-0.001}$
ZTF19acftfav	$58767.8^{+0.1}_{-0.1}$	$12.03^{+0.103}_{-0.029}$	$1.504^{+0.034}_{-0.028}$	$0.009^{+0.000}_{-0.000}$	$0.864^{+0.023}_{-0.025}$	$4.996^{+0.003}_{-0.012}$	$1.226^{+0.033}_{-0.035}$	$0.015^{+0.000}_{-0.000}$
ZTF19acgbkzr	$58769.6^{+0.8}_{-1.3}$	$12.16^{+3.068}_{-0.158}$	$1.179^{+0.067}_{-0.253}$	$0.007^{+0.001}_{-0.005}$	$0.778^{+0.215}_{-0.129}$	$4.079^{+0.868}_{-1.557}$	$0.506^{+0.239}_{-0.173}$	$0.033^{+0.002}_{-0.002}$
ZTF19acignlo	$58775.1^{+0.1}_{-0.1}$	$12.00^{+0.009}_{-0.002}$	$0.742^{+0.020}_{-0.020}$	$0.007^{+0.000}_{-0.000}$	$0.998^{+0.001}_{-0.005}$	$4.711^{+0.123}_{-0.168}$	$0.610^{+0.047}_{-0.045}$	$0.023^{+0.000}_{-0.000}$
ZTF19acjwdnu	$58776.9^{+0.2}_{-0.2}$	$12.01^{+0.059}_{-0.015}$	$1.977^{+0.021}_{-0.060}$	$0.009^{+0.000}_{-0.000}$	$0.998^{+0.001}_{-0.005}$	$3.746^{+0.110}_{-0.192}$	$0.404^{+0.094}_{-0.075}$	$0.039^{+0.001}_{-0.001}$
ZTF19aclobbu	$58782.0^{+0.1}_{-0.1}$	$12.15^{+0.070}_{-0.070}$	$0.758^{+0.009}_{-0.009}$	$0.006^{+0.000}_{-0.000}$	$0.729^{+0.023}_{-0.024}$	$3.971^{+0.099}_{-0.092}$	$0.549^{+0.029}_{-0.025}$	$0.014^{+0.000}_{-0.000}$
ZTF19acryurj	$58794.8^{+0.0}_{-0.0}$	$12.00^{+0.006}_{-0.001}$	$1.999^{+0.000}_{-0.001}$	$0.009^{+7.949}_{-2.776}$	$0.999^{+0.000}_{-0.000}$	$3.749^{+0.003}_{-0.002}$	$0.584^{+0.039}_{-0.037}$	$0.021^{+0.000}_{-0.000}$
ZTF19acszmgx	$58791.2^{+0.7}_{-1.1}$	$15.26^{+0.571}_{-0.648}$	$1.096^{+0.332}_{-0.044}$	$0.003^{+0.005}_{-0.001}$	$0.994^{+0.004}_{-0.107}$	$4.735^{+0.236}_{-0.798}$	$0.380^{+0.153}_{-0.283}$	$0.034^{+0.003}_{-0.001}$
ZTF19acvrjzd	$58801.2^{+1.1}_{-0.3}$	$13.13^{+0.292}_{-1.099}$	$1.995^{+0.004}_{-0.017}$	$0.009^{+0.000}_{-0.006}$	$0.993^{+0.005}_{-0.011}$	$2.510^{+2.485}_{-0.325}$	$0.106^{+0.084}_{-0.051}$	$0.041^{+0.001}_{-0.001}$
ZTF19acwrrvg	$58809.3^{+0.0}_{-0.0}$	$12.00^{+0.003}_{-0.000}$	$1.999^{+0.000}_{-0.001}$	$0.009^{+2.930}_{-9.646}$	$0.999^{+7.072}_{-0.000}$	$3.750^{+0.000}_{-0.000}$	$0.112^{+0.019}_{-0.017}$	$0.027^{+0.000}_{-0.000}$
ZTF19acxowrr	$58817.5^{+1.1}_{-0.0}$	$15.98^{+0.012}_{-0.041}$	$1.084^{+0.040}_{-0.224}$	$0.009^{+3.234}_{-0.000}$	$0.889^{+0.027}_{-0.077}$	$4.994^{+0.005}_{-1.248}$	$0.003^{+0.004}_{-0.002}$	$0.041^{+0.000}_{-0.005}$
ZTF19acyplkt	$58825.2^{+0.3}_{-0.3}$	$12.81^{+0.260}_{-0.348}$	$1.996^{+0.002}_{-0.009}$	$0.009^{+2.024}_{-8.138}$	$0.999^{+0.000}_{-0.001}$	$2.502^{+0.310}_{-0.061}$	$0.262^{+0.035}_{-0.033}$	$0.034^{+0.000}_{-0.000}$
ZTF19acytcsg	$58827.7^{+1.0}_{-0.2}$	$12.77^{+0.153}_{-0.179}$	$1.233^{+0.043}_{-0.136}$	$0.002^{+0.000}_{-0.002}$	$0.678^{+0.317}_{-0.065}$	$3.757^{+1.238}_{-0.032}$	$0.002^{+0.006}_{-0.002}$	$0.028^{+0.000}_{-0.000}$

ZTF19adbryab	$58834.6^{+1.2}_{-0.6}$	$12.05^{+0.437}_{-0.048}$	$0.555^{+0.123}_{-0.050}$	$0.000^{+0.004}_{-0.000}$	$0.960^{+0.035}_{-0.444}$	$1.853^{+1.134}_{-0.317}$	$0.980^{+0.267}_{-0.099}$	$0.021^{+0.001}_{-0.001}$
ZTF20aadchdd	$58840.5^{+0.1}_{-0.3}$	$12.00^{+0.019}_{-0.006}$	$0.517^{+0.014}_{-0.013}$	$0.009^{+2.095}_{-6.474}$	$0.999^{+0.000}_{-0.001}$	$3.749^{+0.019}_{-0.020}$	$0.217^{+0.044}_{-0.066}$	$0.036^{+0.000}_{-0.001}$
ZTF20aaekbdr	$58847.4^{+0.2}_{-0.3}$	$12.03^{+0.103}_{-0.028}$	$1.153^{+0.066}_{-0.060}$	$0.009^{+0.000}_{-0.000}$	$0.997^{+0.002}_{-0.008}$	$3.751^{+0.071}_{-0.057}$	$1.125^{+0.097}_{-0.087}$	$0.036^{+0.002}_{-0.001}$
ZTF20aafclxb	$58851.5^{+0.3}_{-0.1}$	$12.00^{+0.032}_{-0.005}$	$1.819^{+0.018}_{-0.015}$	$0.003^{+0.000}_{-9.861}$	$0.998^{+0.001}_{-0.004}$	$4.985^{+0.013}_{-1.048}$	$0.746^{+0.031}_{-0.064}$	$0.015^{+0.000}_{-0.000}$
ZTF20aagjpmt	$58857.3^{+0.4}_{-0.7}$	$12.60^{+0.491}_{-0.326}$	$1.079^{+0.237}_{-0.184}$	$0.007^{+0.000}_{-0.001}$	$0.571^{+0.085}_{-0.055}$	$3.651^{+0.783}_{-0.369}$	$0.533^{+0.104}_{-0.081}$	$0.018^{+0.001}_{-0.001}$
ZTF20aagnbes	$58858.1^{+0.1}_{-0.1}$	$12.74^{+0.121}_{-0.150}$	$1.022^{+0.009}_{-0.010}$	$0.009^{+4.472}_{-0.000}$	$0.999^{+0.000}_{-0.001}$	$3.750^{+0.026}_{-0.015}$	$1.007^{+0.025}_{-0.029}$	$0.019^{+0.000}_{-0.000}$
ZTF20aahqbsr	$58860.2^{+1.0}_{-1.2}$	$14.09^{+0.686}_{-0.132}$	$1.107^{+0.084}_{-0.231}$	$0.004^{+0.003}_{-0.001}$	$0.710^{+0.045}_{-0.199}$	$4.467^{+0.404}_{-3.102}$	$0.995^{+0.140}_{-0.196}$	$0.020^{+0.002}_{-0.000}$
ZTF20aahqbun	$58856.5^{+0.4}_{-0.3}$	$13.62^{+0.253}_{-0.263}$	$1.297^{+0.051}_{-0.042}$	$0.009^{+0.000}_{-0.000}$	$0.999^{+0.000}_{-0.001}$	$4.986^{+0.012}_{-0.043}$	$1.259^{+0.058}_{-0.056}$	$0.024^{+0.000}_{-0.000}$
ZTF20aanvqbi	$58889.5^{+0.0}_{-0.0}$	$13.49^{+0.119}_{-0.748}$	$1.949^{+0.048}_{-0.779}$	$0.009^{+9.158}_{-0.000}$	$0.674^{+0.158}_{-0.048}$	$3.752^{+1.230}_{-0.015}$	$0.708^{+0.091}_{-0.094}$	$0.023^{+0.001}_{-0.000}$
ZTF20aaoldej	$58889.6^{+0.2}_{-0.2}$	$12.21^{+0.246}_{-0.190}$	$1.541^{+0.032}_{-0.030}$	$0.005^{+0.000}_{-0.000}$	$0.994^{+0.005}_{-0.013}$	$3.970^{+0.791}_{-0.342}$	$0.688^{+0.102}_{-0.126}$	$0.031^{+0.001}_{-0.000}$
ZTF20aapycrh	$58897.1^{+0.0}_{-2.4}$	$12.27^{+3.284}_{-0.151}$	$1.536^{+0.027}_{-0.361}$	$0.000^{+0.002}_{-8.475}$	$0.956^{+0.032}_{-0.095}$	$3.822^{+0.783}_{-0.742}$	$0.002^{+0.052}_{-0.002}$	$0.037^{+0.000}_{-0.000}$
ZTF20aascvvo	$58898.9^{+0.1}_{-0.1}$	$15.99^{+0.002}_{-0.007}$	$1.068^{+0.007}_{-0.007}$	$0.009^{+2.730}_{-9.373}$	$0.999^{+4.038}_{-0.000}$	$4.856^{+0.016}_{-0.018}$	$0.693^{+0.027}_{-0.024}$	$0.017^{+0.000}_{-0.000}$
ZTF20aasjzhg	$58903.9^{+1.5}_{-0.2}$	$13.91^{+0.095}_{-0.872}$	$0.992^{+0.014}_{-0.030}$	$0.000^{+0.009}_{-6.625}$	$0.994^{+0.005}_{-0.159}$	$4.903^{+0.092}_{-1.162}$	$0.045^{+0.127}_{-0.043}$	$0.014^{+0.000}_{-0.000}$
ZTF20aatqgeo	$58919.2^{+0.0}_{-0.0}$	$14.88^{+0.288}_{-0.282}$	$1.986^{+0.012}_{-0.038}$	$0.009^{+5.675}_{-0.000}$	$0.999^{+0.000}_{-0.001}$	$3.765^{+0.072}_{-0.097}$	$0.555^{+0.067}_{-0.060}$	$0.038^{+0.000}_{-0.000}$
ZTF20aatqidk	$58919.0^{+1.9}_{-0.8}$	$13.27^{+0.217}_{-0.222}$	$1.308^{+0.396}_{-0.090}$	$0.007^{+0.002}_{-0.001}$	$0.647^{+0.077}_{-0.094}$	$4.966^{+0.030}_{-0.207}$	$0.437^{+0.230}_{-0.128}$	$0.032^{+0.001}_{-0.001}$
ZTF20aattqle	$58917.9^{+0.2}_{-0.3}$	$13.86^{+0.289}_{-0.194}$	$1.983^{+0.015}_{-0.041}$	$0.006^{+0.000}_{-0.000}$	$0.999^{+0.000}_{-0.001}$	$4.739^{+0.093}_{-0.103}$	$0.647^{+0.092}_{-0.085}$	$0.028^{+0.000}_{-0.000}$
ZTF20aatwisu	$58916.0^{+1.7}_{-0.3}$	$12.00^{+0.035}_{-0.007}$	$1.476^{+0.076}_{-0.808}$	$0.009^{+6.448}_{-0.000}$	$0.998^{+0.001}_{-0.003}$	$4.982^{+0.016}_{-1.234}$	$0.235^{+0.074}_{-0.051}$	$0.031^{+0.001}_{-0.008}$
ZTF20aaunfpj	$58929.6^{+0.1}_{-4.1}$	$14.13^{+1.840}_{-0.115}$	$1.995^{+0.004}_{-0.515}$	$0.009^{+5.511}_{-0.004}$	$0.999^{+0.000}_{-0.003}$	$4.998^{+0.000}_{-0.298}$	$1.779^{+0.044}_{-0.299}$	$0.009^{+0.000}_{-0.000}$
ZTF20aauoipy	$58918.3^{+0.6}_{-0.4}$	$15.92^{+0.073}_{-0.233}$	$1.554^{+0.104}_{-0.060}$	$0.009^{+0.000}_{-0.005}$	$0.971^{+0.025}_{-0.059}$	$3.766^{+1.218}_{-0.086}$	$0.618^{+0.143}_{-0.168}$	$0.035^{+0.001}_{-0.001}$
ZTF20aauoktk	$58933.3^{+0.5}_{-0.4}$	$14.96^{+0.764}_{-1.207}$	$0.623^{+0.103}_{-0.057}$	$0.006^{+0.001}_{-0.000}$	$0.997^{+0.002}_{-0.029}$	$4.861^{+0.127}_{-0.434}$	$0.004^{+0.013}_{-0.003}$	$0.040^{+0.001}_{-0.001}$
ZTF20aauompx	$58925.9^{+0.1}_{-0.0}$	$14.72^{+0.104}_{-0.439}$	$1.403^{+0.254}_{-0.064}$	$0.002^{+0.000}_{-0.000}$	$0.577^{+0.157}_{-0.037}$	$1.208^{+0.271}_{-0.146}$	$1.078^{+0.068}_{-0.052}$	$0.020^{+0.000}_{-0.000}$
ZTF20aauqhka	$58935.6^{+0.1}_{-0.2}$	$15.96^{+0.031}_{-0.104}$	$1.308^{+0.043}_{-0.045}$	$0.009^{+2.066}_{-7.222}$	$0.991^{+0.006}_{-0.009}$	$4.998^{+0.001}_{-0.004}$	$0.001^{+0.003}_{-0.001}$	$0.038^{+0.000}_{-0.000}$
ZTF20aauqlwv	$58924.9^{+0.1}_{-0.1}$	$12.00^{+0.025}_{-0.007}$	$1.999^{+0.000}_{-0.001}$	$0.009^{+9.765}_{-0.000}$	$0.998^{+0.001}_{-0.005}$	$3.749^{+0.020}_{-0.024}$	$0.662^{+0.100}_{-0.105}$	$0.029^{+0.000}_{-0.000}$
ZTF20aaurjbj	$58946.3^{+0.0}_{-0.0}$	$12.00^{+0.023}_{-0.007}$	$1.994^{+0.004}_{-0.014}$	$0.009^{+1.770}_{-5.236}$	$0.999^{+0.000}_{-0.000}$	$4.873^{+0.025}_{-0.029}$	$0.001^{+0.002}_{-0.001}$	$0.039^{+0.000}_{-0.000}$
ZTF20aausahr	$58944.4^{+1.0}_{-0.9}$	$12.33^{+0.946}_{-0.310}$	$1.483^{+0.447}_{-0.564}$	$0.006^{+0.002}_{-0.002}$	$0.915^{+0.075}_{-0.072}$	$4.829^{+0.161}_{-1.174}$	$0.651^{+0.167}_{-0.203}$	$0.033^{+0.004}_{-0.005}$
ZTF20aauvjws	$58939.5^{+0.3}_{-0.2}$	$12.02^{+0.059}_{-0.018}$	$1.926^{+0.049}_{-0.049}$	$0.008^{+0.000}_{-0.000}$	$0.990^{+0.008}_{-0.016}$	$4.987^{+0.011}_{-0.042}$	$0.984^{+0.037}_{-0.037}$	$0.026^{+0.000}_{-0.000}$
ZTF20aavdcxo	$58947.1^{+0.3}_{-0.5}$	$12.02^{+0.097}_{-0.024}$	$1.992^{+0.007}_{-0.025}$	$0.009^{+0.000}_{-0.000}$	$0.984^{+0.013}_{-0.025}$	$4.904^{+0.072}_{-0.079}$	$1.079^{+0.057}_{-0.061}$	$0.038^{+0.001}_{-0.001}$
ZTF20aavptjf	$58953.2^{+0.2}_{-0.3}$	$12.02^{+0.111}_{-0.021}$	$1.833^{+0.136}_{-0.182}$	$0.009^{+0.000}_{-0.000}$	$0.967^{+0.014}_{-0.014}$	$4.991^{+0.007}_{-0.029}$	$0.719^{+0.067}_{-0.088}$	$0.030^{+0.001}_{-0.001}$
ZTF20aaynrrh	$58968.9^{+0.0}_{-0.0}$	$12.00^{+0.001}_{-0.000}$	$1.999^{+0.000}_{-0.000}$	$0.009^{+1.805}_{-3.933}$	$0.999^{+7.199}_{-0.000}$	$4.998^{+0.001}_{-0.004}$	$0.376^{+0.006}_{-0.006}$	$0.007^{+4.030}_{-4.034}$
ZTF20aazcnrv	$58967.0^{+0.8}_{-0.6}$	$14.79^{+0.553}_{-1.340}$	$1.489^{+0.146}_{-0.066}$	$0.008^{+0.000}_{-0.000}$	$0.996^{+0.003}_{-0.113}$	$4.958^{+0.038}_{-0.104}$	$0.933^{+0.046}_{-0.083}$	$0.024^{+0.000}_{-0.001}$
ZTF20aazpphd	$58975.8^{+1.9}_{-0.2}$	$12.62^{+0.333}_{-0.579}$	$1.171^{+0.069}_{-0.060}$	$0.009^{+0.000}_{-0.007}$	$0.767^{+0.226}_{-0.147}$	$3.755^{+1.219}_{-0.142}$	$0.776^{+0.061}_{-0.293}$	$0.033^{+0.003}_{-0.001}$
ZTF20aazrxef	$58977.7^{+0.1}_{-0.1}$	$12.00^{+0.029}_{-0.008}$	$1.735^{+0.155}_{-0.166}$	$0.009^{+0.000}_{-0.000}$	$0.817^{+0.031}_{-0.034}$	$4.983^{+0.015}_{-0.053}$	$0.380^{+0.053}_{-0.049}$	$0.030^{+0.001}_{-0.001}$

ZTF20aazswwk	$58978.9^{+0.2}_{-0.2}$	$12.11^{+0.211}_{-0.103}$	$1.171^{+0.037}_{-0.035}$	$0.000^{+8.216}_{-6.780}$	$0.995^{+0.003}_{-0.014}$	$4.207^{+0.414}_{-0.792}$	$0.045^{+0.036}_{-0.027}$	$0.041^{+0.000}_{-0.000}$
ZTF20abccixp	$58990.8^{+0.0}_{-0.0}$	$12.00^{+0.009}_{-0.003}$	$1.998^{+0.000}_{-0.003}$	$0.009^{+1.228}_{-3.683}$	$0.999^{+0.000}_{-0.000}$	$3.750^{+0.003}_{-0.003}$	$0.243^{+0.016}_{-0.015}$	$0.037^{+0.000}_{-0.000}$
ZTF20abfcdkj	$59005.5^{+0.7}_{-0.6}$	$13.83^{+0.382}_{-0.557}$	$0.706^{+0.115}_{-0.060}$	$0.005^{+0.004}_{-0.001}$	$0.965^{+0.032}_{-0.184}$	$4.973^{+0.025}_{-0.147}$	$0.735^{+0.066}_{-0.107}$	$0.035^{+0.001}_{-0.001}$
ZTF20abjaapj	$59020.7^{+0.2}_{-0.2}$	$12.69^{+0.080}_{-0.086}$	$1.899^{+0.053}_{-0.047}$	$0.008^{+0.000}_{-0.000}$	$0.661^{+0.029}_{-0.028}$	$4.995^{+0.004}_{-0.016}$	$0.768^{+0.028}_{-0.050}$	$0.025^{+0.000}_{-0.000}$
ZTF20abjatqy	$59022.1^{+0.7}_{-0.1}$	$13.93^{+0.135}_{-0.354}$	$1.865^{+0.097}_{-0.080}$	$0.006^{+0.000}_{-0.004}$	$0.689^{+0.018}_{-0.059}$	$3.753^{+1.224}_{-0.039}$	$1.275^{+0.042}_{-0.078}$	$0.014^{+0.000}_{-0.000}$
ZTF20abjcyhg	$59024.1^{+0.0}_{-0.1}$	$12.00^{+0.018}_{-0.004}$	$1.928^{+0.059}_{-0.074}$	$0.009^{+0.000}_{-0.000}$	$0.999^{+0.000}_{-0.001}$	$4.729^{+0.094}_{-0.092}$	$0.477^{+0.040}_{-0.039}$	$0.025^{+0.000}_{-0.000}$
ZTF20abjonjs	$59027.8^{+0.1}_{-0.1}$	$13.41^{+0.139}_{-0.149}$	$0.758^{+0.016}_{-0.015}$	$0.002^{+0.000}_{-0.000}$	$0.997^{+0.002}_{-0.010}$	$3.748^{+0.080}_{-0.085}$	$0.746^{+0.046}_{-0.080}$	$0.018^{+0.000}_{-0.000}$
ZTF20abjyorg	$59027.5^{+1.0}_{-0.8}$	$13.81^{+0.976}_{-0.597}$	$1.988^{+0.010}_{-0.039}$	$0.009^{+0.000}_{-0.001}$	$0.998^{+0.001}_{-0.005}$	$3.375^{+1.057}_{-0.936}$	$0.272^{+0.091}_{-0.074}$	$0.057^{+0.002}_{-0.002}$
ZTF20ablklei	$59037.2^{+0.2}_{-0.1}$	$12.31^{+0.103}_{-0.230}$	$1.757^{+0.031}_{-0.026}$	$0.008^{+0.000}_{-0.000}$	$0.995^{+0.003}_{-0.018}$	$4.997^{+0.001}_{-0.007}$	$0.602^{+0.039}_{-0.043}$	$0.026^{+0.000}_{-0.000}$
ZTF20abqferm	$59060.5^{+0.2}_{-0.2}$	$12.05^{+0.142}_{-0.049}$	$1.718^{+0.063}_{-0.059}$	$0.002^{+0.000}_{-0.000}$	$0.995^{+0.004}_{-0.015}$	$4.464^{+0.399}_{-0.994}$	$0.258^{+0.057}_{-0.066}$	$0.045^{+0.001}_{-0.001}$
ZTF20abupxie	$59072.4^{+0.1}_{-0.0}$	$12.01^{+0.045}_{-0.011}$	$1.107^{+0.011}_{-0.013}$	$0.008^{+0.000}_{-0.000}$	$0.999^{+0.000}_{-0.001}$	$4.994^{+0.004}_{-0.025}$	$0.898^{+0.024}_{-0.019}$	$0.015^{+0.000}_{-0.000}$
ZTF20abuqali	$59063.1^{+0.5}_{-0.1}$	$15.87^{+0.114}_{-0.717}$	$1.109^{+0.313}_{-0.059}$	$0.009^{+0.000}_{-0.002}$	$0.993^{+0.005}_{-0.019}$	$3.751^{+1.199}_{-0.079}$	$1.012^{+0.083}_{-0.349}$	$0.032^{+0.006}_{-0.001}$
ZTF20abwdaeo	$59074.9^{+0.3}_{-0.3}$	$13.15^{+0.151}_{-0.153}$	$0.908^{+0.039}_{-0.035}$	$0.004^{+0.000}_{-0.000}$	$0.996^{+0.002}_{-0.010}$	$4.950^{+0.045}_{-0.110}$	$0.799^{+0.033}_{-0.056}$	$0.020^{+0.000}_{-0.000}$
ZTF20abybeex	$59085.2^{+0.6}_{-0.2}$	$15.96^{+0.030}_{-0.949}$	$0.616^{+0.414}_{-0.050}$	$0.009^{+0.000}_{-0.000}$	$0.500^{+0.006}_{-0.005}$	$3.740^{+0.392}_{-0.301}$	$0.711^{+0.062}_{-0.098}$	$0.022^{+0.001}_{-0.000}$
ZTF20abywoaa	$59086.2^{+0.2}_{-0.2}$	$12.02^{+0.075}_{-0.022}$	$1.987^{+0.011}_{-0.034}$	$0.009^{+8.930}_{-0.000}$	$0.997^{+0.002}_{-0.007}$	$4.988^{+0.010}_{-0.036}$	$0.466^{+0.109}_{-0.072}$	$0.046^{+0.001}_{-0.001}$
ZTF20abywydb	$59091.0^{+0.2}_{-0.2}$	$12.00^{+0.022}_{-0.006}$	$1.992^{+0.006}_{-0.021}$	$0.009^{+2.381}_{-7.608}$	$0.999^{+0.000}_{-0.001}$	$3.750^{+0.023}_{-0.019}$	$0.271^{+0.043}_{-0.041}$	$0.054^{+0.001}_{-0.001}$
ZTF20abyylgi	$59098.0^{+0.0}_{-0.0}$	$13.44^{+0.033}_{-0.030}$	$1.998^{+0.001}_{-0.005}$	$0.007^{+0.000}_{-0.000}$	$0.574^{+0.012}_{-0.011}$	$4.999^{+0.000}_{-0.002}$	$0.000^{+0.001}_{-0.000}$	$0.020^{+0.000}_{-0.000}$
ZTF20abyzomt	$59097.6^{+0.0}_{-0.0}$	$12.00^{+0.017}_{-0.004}$	$1.590^{+0.018}_{-0.018}$	$0.007^{+0.000}_{-0.000}$	$0.990^{+0.006}_{-0.006}$	$4.997^{+0.002}_{-0.008}$	$0.707^{+0.051}_{-0.053}$	$0.021^{+0.000}_{-0.000}$
ZTF20abyzprl	$59097.0^{+0.2}_{-0.2}$	$14.16^{+0.127}_{-0.133}$	$1.283^{+0.095}_{-0.077}$	$0.004^{+0.000}_{-0.000}$	$0.704^{+0.034}_{-0.038}$	$4.942^{+0.051}_{-0.114}$	$0.734^{+0.050}_{-0.085}$	$0.024^{+0.000}_{-0.000}$
ZTF20abzoaas	$59096.8^{+0.1}_{-0.2}$	$12.00^{+0.005}_{-0.001}$	$0.568^{+0.022}_{-0.025}$	$0.009^{+4.823}_{-1.833}$	$0.999^{+0.000}_{-0.000}$	$3.750^{+0.002}_{-0.002}$	$0.468^{+0.033}_{-0.033}$	$0.022^{+0.000}_{-0.000}$
ZTF20abzxihn	$59097.8^{+1.2}_{-0.6}$	$12.03^{+0.112}_{-0.027}$	$1.957^{+0.039}_{-0.191}$	$0.009^{+8.233}_{-0.000}$	$0.997^{+0.002}_{-0.007}$	$3.746^{+0.054}_{-1.252}$	$0.305^{+0.105}_{-0.112}$	$0.090^{+0.008}_{-0.008}$
ZTF20accrldu	$59108.6^{+0.1}_{-1.0}$	$12.27^{+0.952}_{-0.250}$	$1.710^{+0.065}_{-0.099}$	$0.008^{+0.001}_{-0.001}$	$0.969^{+0.019}_{-0.022}$	$3.749^{+0.123}_{-0.215}$	$0.725^{+0.081}_{-0.120}$	$0.037^{+0.001}_{-0.001}$
ZTF20acectxy	$59110.6^{+0.1}_{-0.1}$	$12.02^{+0.069}_{-0.020}$	$1.691^{+0.171}_{-0.166}$	$0.009^{+0.000}_{-0.000}$	$0.998^{+0.001}_{-0.006}$	$4.990^{+0.009}_{-0.030}$	$0.416^{+0.080}_{-0.069}$	$0.044^{+0.002}_{-0.002}$
ZTF20acfdmex	$59114.3^{+0.0}_{-0.0}$	$12.85^{+0.074}_{-0.054}$	$1.000^{+0.003}_{-0.001}$	$0.002^{+2.242}_{-6.541}$	$0.740^{+0.026}_{-0.026}$	$3.749^{+0.004}_{-0.004}$	$0.317^{+0.025}_{-0.022}$	$0.021^{+0.000}_{-0.000}$
ZTF20acfkyll	$59112.9^{+1.6}_{-0.1}$	$13.83^{+0.138}_{-0.129}$	$1.068^{+0.046}_{-0.340}$	$0.009^{+0.000}_{-0.006}$	$0.714^{+0.285}_{-0.035}$	$3.739^{+0.020}_{-0.809}$	$0.441^{+0.057}_{-0.085}$	$0.018^{+0.000}_{-0.000}$
ZTF20acfkzcg	$59115.4^{+0.0}_{-0.7}$	$12.12^{+0.588}_{-0.120}$	$0.937^{+0.061}_{-0.027}$	$0.003^{+0.000}_{-0.000}$	$0.500^{+0.013}_{-0.003}$	$3.765^{+0.981}_{-0.022}$	$0.414^{+0.036}_{-0.066}$	$0.019^{+0.000}_{-0.000}$
ZTF20acfvgdp	$59114.7^{+0.2}_{-0.3}$	$12.01^{+0.060}_{-0.013}$	$1.000^{+0.016}_{-0.015}$	$0.001^{+0.004}_{-0.000}$	$0.500^{+0.038}_{-0.024}$	$3.143^{+0.709}_{-1.412}$	$0.134^{+0.081}_{-0.060}$	$0.030^{+0.000}_{-0.000}$
ZTF20acgided	$59116.4^{+0.1}_{-0.0}$	$13.10^{+0.065}_{-0.062}$	$1.998^{+0.001}_{-0.004}$	$0.008^{+0.000}_{-0.000}$	$0.555^{+0.028}_{-0.023}$	$4.997^{+0.002}_{-0.007}$	$0.023^{+0.025}_{-0.010}$	$0.021^{+0.000}_{-0.000}$
ZTF20acgnelh	$59116.3^{+1.2}_{-1.0}$	$13.60^{+1.369}_{-0.775}$	$1.150^{+0.091}_{-0.103}$	$0.005^{+0.003}_{-0.003}$	$0.981^{+0.016}_{-0.127}$	$4.496^{+0.462}_{-0.964}$	$0.332^{+0.246}_{-0.163}$	$0.034^{+0.002}_{-0.002}$
ZTF20acgoxns	$59135.5^{+0.1}_{-0.0}$	$12.03^{+3.583}_{-0.029}$	$1.990^{+0.008}_{-0.092}$	$0.002^{+0.000}_{-0.001}$	$0.996^{+0.002}_{-0.611}$	$3.774^{+1.100}_{-0.083}$	$1.462^{+0.147}_{-1.348}$	$0.020^{+0.017}_{-0.001}$
ZTF20achbejn	$59119.6^{+0.4}_{-0.3}$	$13.25^{+0.398}_{-0.462}$	$1.137^{+0.053}_{-0.046}$	$0.006^{+0.001}_{-0.001}$	$0.988^{+0.010}_{-0.043}$	$4.943^{+0.052}_{-0.347}$	$0.806^{+0.074}_{-0.125}$	$0.033^{+0.001}_{-0.001}$
ZTF20achuhlt	$59114.3^{+0.3}_{-0.3}$	$14.12^{+0.416}_{-0.160}$	$1.984^{+0.014}_{-0.051}$	$0.001^{+0.000}_{-0.000}$	$0.706^{+0.128}_{-0.371}$	$1.115^{+0.120}_{-0.068}$	$0.002^{+0.009}_{-0.002}$	$0.052^{+0.001}_{-0.001}$

ZTF20acitoie	$59127.8^{+0.8}_{-0.3}$	$12.01^{+0.040}_{-0.009}$	$1.052^{+0.033}_{-0.034}$	$0.004^{+0.005}_{-0.001}$	$0.556^{+0.070}_{-0.168}$	$3.737^{+0.104}_{-1.280}$	$0.645^{+0.123}_{-0.090}$	$0.022^{+0.000}_{-0.000}$
ZTF20aciubfx	$59124.4^{+0.5}_{-0.1}$	$12.00^{+0.015}_{-0.005}$	$1.997^{+0.002}_{-0.007}$	$0.009^{+1.479}_{-5.398}$	$0.999^{+0.000}_{-0.000}$	$3.750^{+0.013}_{-0.013}$	$1.148^{+0.044}_{-0.044}$	$0.027^{+0.000}_{-0.000}$
ZTF20acknpig	$59134.3^{+0.1}_{-0.2}$	$12.74^{+0.289}_{-0.168}$	$0.926^{+0.113}_{-0.044}$	$0.002^{+0.000}_{-0.000}$	$0.500^{+0.012}_{-0.009}$	$3.749^{+0.025}_{-0.029}$	$0.435^{+0.069}_{-0.062}$	$0.023^{+0.000}_{-0.000}$
ZTF20acmaaan	$59138.1^{+0.1}_{-0.1}$	$12.04^{+0.127}_{-0.042}$	$1.396^{+0.048}_{-0.048}$	$0.001^{+0.000}_{-4.137}$	$0.998^{+0.001}_{-0.005}$	$3.751^{+0.081}_{-0.073}$	$0.576^{+0.090}_{-0.073}$	$0.027^{+0.000}_{-0.000}$
ZTF20acpevli	$59150.8^{+0.9}_{-0.2}$	$12.10^{+0.196}_{-0.089}$	$1.063^{+0.055}_{-0.016}$	$0.009^{+0.000}_{-0.004}$	$0.933^{+0.052}_{-0.024}$	$4.986^{+0.012}_{-0.047}$	$0.883^{+0.040}_{-0.188}$	$0.023^{+0.002}_{-0.000}$
ZTF20acpvbbh	$59157.3^{+0.0}_{-0.0}$	$12.00^{+0.002}_{-0.000}$	$1.999^{+0.000}_{-0.002}$	$0.009^{+3.896}_{-1.107}$	$0.999^{+6.792}_{-0.000}$	$3.750^{+0.002}_{-0.001}$	$0.085^{+0.022}_{-0.017}$	$0.033^{+0.000}_{-0.000}$
ZTF20acqexmr	$59161.8^{+0.1}_{-0.1}$	$12.03^{+0.109}_{-0.033}$	$1.514^{+0.014}_{-0.013}$	$0.001^{+0.000}_{-0.000}$	$0.996^{+0.003}_{-0.012}$	$3.785^{+0.578}_{-0.513}$	$2.409^{+0.097}_{-0.100}$	$0.011^{+0.000}_{-0.000}$
ZTF20acrinvz	$59166.5^{+0.4}_{-0.4}$	$12.80^{+0.447}_{-0.482}$	$1.047^{+0.071}_{-0.058}$	$0.000^{+0.000}_{-0.000}$	$0.914^{+0.072}_{-0.328}$	$3.507^{+0.750}_{-1.230}$	$0.016^{+0.065}_{-0.015}$	$0.041^{+0.001}_{-0.001}$
ZTF20actawpa	$59169.1^{+0.0}_{-0.0}$	$12.00^{+0.007}_{-0.002}$	$1.926^{+0.012}_{-0.013}$	$0.009^{+1.498}_{-5.775}$	$0.999^{+0.000}_{-0.000}$	$3.750^{+0.008}_{-0.007}$	$0.349^{+0.015}_{-0.015}$	$0.022^{+0.000}_{-0.000}$
ZTF20actnuls	$59169.1^{+0.2}_{-0.3}$	$12.40^{+0.383}_{-0.346}$	$1.677^{+0.062}_{-0.040}$	$0.009^{+0.000}_{-0.001}$	$0.998^{+0.001}_{-0.004}$	$3.810^{+1.094}_{-0.217}$	$1.245^{+0.075}_{-0.074}$	$0.026^{+0.001}_{-0.001}$
ZTF20actpavu	$59169.3^{+1.1}_{-0.9}$	$14.21^{+1.102}_{-1.537}$	$1.068^{+0.863}_{-0.366}$	$0.003^{+0.004}_{-0.001}$	$0.922^{+0.063}_{-0.198}$	$4.499^{+0.427}_{-1.059}$	$0.651^{+0.185}_{-0.305}$	$0.027^{+0.006}_{-0.003}$
ZTF20actquzl	$59170.8^{+0.1}_{-0.1}$	$12.01^{+0.036}_{-0.010}$	$1.796^{+0.059}_{-0.057}$	$0.009^{+5.665}_{-0.000}$	$0.998^{+0.001}_{-0.004}$	$4.991^{+0.008}_{-0.028}$	$0.418^{+0.051}_{-0.043}$	$0.033^{+0.000}_{-0.000}$
ZTF20acuhren	$59175.8^{+0.4}_{-0.5}$	$12.99^{+0.382}_{-0.338}$	$0.880^{+0.161}_{-0.081}$	$0.009^{+0.000}_{-0.004}$	$0.423^{+0.092}_{-0.128}$	$1.750^{+0.747}_{-0.276}$	$0.929^{+0.075}_{-0.078}$	$0.019^{+0.001}_{-0.000}$
ZTF20acvjagm	$59176.2^{+0.0}_{-0.0}$	$15.66^{+0.094}_{-0.095}$	$1.064^{+0.012}_{-0.021}$	$0.009^{+4.589}_{-0.000}$	$0.999^{+0.000}_{-0.002}$	$4.951^{+0.024}_{-0.036}$	$0.343^{+0.019}_{-0.038}$	$0.020^{+0.000}_{-0.000}$
ZTF20acxtdcm	$59191.2^{+0.9}_{-0.6}$	$13.45^{+0.489}_{-0.455}$	$1.226^{+0.102}_{-0.081}$	$0.007^{+0.001}_{-0.002}$	$0.974^{+0.021}_{-0.036}$	$4.940^{+0.054}_{-0.317}$	$0.656^{+0.160}_{-0.201}$	$0.040^{+0.002}_{-0.002}$
ZTF20acyqzeu	$59195.8^{+0.0}_{-0.0}$	$12.05^{+0.060}_{-0.045}$	$1.228^{+0.012}_{-0.011}$	$0.009^{+4.628}_{-1.626}$	$0.999^{+0.000}_{-0.000}$	$4.999^{+0.000}_{-0.001}$	$0.867^{+0.013}_{-0.013}$	$0.016^{+0.000}_{-0.000}$
ZTF21aaabwem	$59201.6^{+0.9}_{-0.3}$	$13.33^{+0.540}_{-1.124}$	$1.964^{+0.032}_{-0.077}$	$0.009^{+0.000}_{-0.001}$	$0.995^{+0.004}_{-0.096}$	$4.912^{+0.081}_{-0.291}$	$0.674^{+0.133}_{-0.178}$	$0.049^{+0.002}_{-0.002}$
ZTF21aabfwwl	$59211.6^{+0.2}_{-0.4}$	$13.64^{+0.184}_{-0.172}$	$1.002^{+0.007}_{-0.002}$	$0.000^{+0.000}_{-7.377}$	$0.999^{+0.000}_{-0.001}$	$4.992^{+0.006}_{-0.024}$	$0.738^{+0.067}_{-0.110}$	$0.026^{+0.000}_{-0.000}$
ZTF21aafepon	$59223.5^{+0.0}_{-0.0}$	$14.00^{+0.053}_{-0.037}$	$1.262^{+0.587}_{-0.270}$	$0.009^{+0.000}_{-0.000}$	$0.499^{+0.003}_{-0.003}$	$3.750^{+0.013}_{-0.015}$	$1.483^{+0.046}_{-0.043}$	$0.009^{+0.000}_{-0.000}$
ZTF21aafkktu	$59225.9^{+0.2}_{-0.2}$	$13.15^{+0.322}_{-0.308}$	$1.083^{+0.031}_{-0.033}$	$0.003^{+0.000}_{-0.000}$	$0.995^{+0.003}_{-0.011}$	$4.675^{+0.211}_{-0.423}$	$0.011^{+0.043}_{-0.010}$	$0.037^{+0.000}_{-0.000}$
ZTF21aafkwtk	$59225.5^{+0.1}_{-2.0}$	$12.81^{+3.101}_{-0.252}$	$1.363^{+0.037}_{-0.286}$	$0.002^{+0.000}_{-0.000}$	$0.999^{+0.000}_{-0.008}$	$3.779^{+1.198}_{-0.101}$	$0.592^{+0.281}_{-0.100}$	$0.028^{+0.000}_{-0.002}$
ZTF21aagbeah	$59225.8^{+0.1}_{-0.0}$	$12.07^{+0.193}_{-0.067}$	$1.989^{+0.009}_{-0.031}$	$0.009^{+0.000}_{-0.000}$	$0.997^{+0.002}_{-0.008}$	$2.498^{+0.133}_{-0.130}$	$0.089^{+0.093}_{-0.051}$	$0.058^{+0.002}_{-0.002}$
ZTF21aagnzjy	$59230.7^{+0.3}_{-0.4}$	$12.00^{+0.017}_{-0.004}$	$1.502^{+0.010}_{-0.020}$	$0.004^{+0.001}_{-0.000}$	$0.876^{+0.028}_{-0.043}$	$4.122^{+0.299}_{-0.585}$	$1.058^{+0.046}_{-0.029}$	$0.013^{+0.000}_{-0.000}$
ZTF21aagsysd	$59233.0^{+0.1}_{-0.1}$	$12.00^{+0.008}_{-0.002}$	$1.999^{+0.000}_{-0.001}$	$0.009^{+5.476}_{-2.267}$	$0.999^{+0.000}_{-0.000}$	$3.750^{+0.002}_{-0.002}$	$1.052^{+0.031}_{-0.029}$	$0.023^{+0.000}_{-0.000}$
ZTF21aagtekf	$59237.1^{+1.1}_{-2.4}$	$12.01^{+0.054}_{-0.016}$	$1.991^{+0.008}_{-0.027}$	$0.009^{+0.000}_{-0.000}$	$0.791^{+0.068}_{-0.064}$	$4.985^{+0.013}_{-0.054}$	$0.023^{+0.093}_{-0.018}$	$0.068^{+0.001}_{-0.002}$
ZTF21aaiaeri	$59245.2^{+0.4}_{-0.1}$	$12.01^{+0.052}_{-0.012}$	$1.995^{+0.004}_{-0.015}$	$0.008^{+0.000}_{-0.000}$	$0.999^{+0.000}_{-0.003}$	$3.734^{+0.122}_{-1.153}$	$0.407^{+0.088}_{-0.078}$	$0.047^{+0.001}_{-0.001}$
ZTF21aaiaqhh	$59246.4^{+0.0}_{-0.0}$	$12.00^{+0.002}_{-0.000}$	$1.999^{+0.000}_{-0.001}$	$0.009^{+3.539}_{-1.055}$	$0.999^{+3.372}_{-0.000}$	$3.750^{+0.002}_{-0.001}$	$0.040^{+0.019}_{-0.022}$	$0.031^{+0.000}_{-0.000}$
ZTF21aapdulz	$59275.3^{+0.2}_{-0.2}$	$12.06^{+0.170}_{-0.059}$	$0.513^{+0.033}_{-0.012}$	$0.009^{+8.187}_{-0.000}$	$0.998^{+0.001}_{-0.004}$	$2.470^{+0.106}_{-0.765}$	$0.922^{+0.051}_{-0.054}$	$0.023^{+0.000}_{-0.000}$
ZTF21aapegtd	$59276.8^{+0.6}_{-0.1}$	$12.00^{+0.019}_{-0.005}$	$1.994^{+0.004}_{-0.019}$	$0.009^{+3.177}_{-0.000}$	$0.999^{+0.000}_{-0.001}$	$3.746^{+0.031}_{-1.255}$	$0.456^{+0.079}_{-0.096}$	$0.040^{+0.001}_{-0.001}$

4.2 Sample distribution

The inferred values, shown in Table 4.1, are the ones we associate with each object in order to study the distribution of physical parameters for the whole sample of 186 SNe II. These distributions are shown in Fig. 4.2. Table 4.2 contains a summary of the sample distribution of parameters from Fib. 4.2. Here we report the mean, standard deviation, median, percentile 5 (P_5), and percentile 95 (P_{95}) of the distributions.

Table 4.2: Sample parameters distributions summary

Parameter	Mean	Sigma	Median	P_5	P_{95}
Mass [$M_\odot$]	12.94	1.14	12.39	12.001	15.56
Energy [foe]	1.44	0.45	1.47	0.69	1.99
Mass loss rate [$M_\odot$ year^{-1}]	0.0068	0.0033	0.008	0.0007	0.0099
r_{CSM} [10^{15} cm]	0.87	0.17	0.98	0.50	0.99
β	4.18	0.83	4.15	2.50	4.99
A_V [mag]	0.55	0.40	0.50	0.003	1.23

We used a Bayesian approach to found the value of the exponent (α) of a power-law distribution for our mass distribution. We ran MCMC using one mass value sampled from the mass posterior for every SNe to consider the error of the mass. We took the median of this posterior as the value of α. We repeated this process 100 times with a different mass sampled from the posterior of the SNe in order to obtain confidence interval of α.We found that the mass distribution for our whole sample follows a power-law distribution with $\alpha = 11.65\ ^{+0.37}_{-0.32}$ (see fig. 4.4) steeper than the value found in [44] and steeper than the Salpeter IMF [61] where α =2.35. Our results also show that the models that best fit the data have high mass loss rates, high r_{CSM} values, and values of $\beta > 2$. A double peak shape in the distributions of energy (near 1 and 2 foe) and β are observed.

In Fig. 4.3 we present a pair-plot for the fitted physical parameters, where there are no clear visual correlations between any of pair of parameters any pair-plot parameters, aside from A_V and redshift. We confirmed this by calculating the Pearson correlation coefficient (PCC) to look for the correlation between parameters. To have robust results we do bootstrapping, we calculated the PCC for samples with replacement 100 times to obtain a distribution of PCC for every combination of parameters. In Fig. 4.5 we display a correlation matrix where the reported values correspond to the median of the PCC distribution and the subscript and superscript to the distances to the percentiles 2.5 and 97.5 respectively.

The redshift and the attenuation affect the peak of the SN, but A_V also affects the color of the SN, this can be seen in the LC as the separation between different filters, so adding different filters would help constrain the value of A_V and therefore obtain a better estimation of redshift.

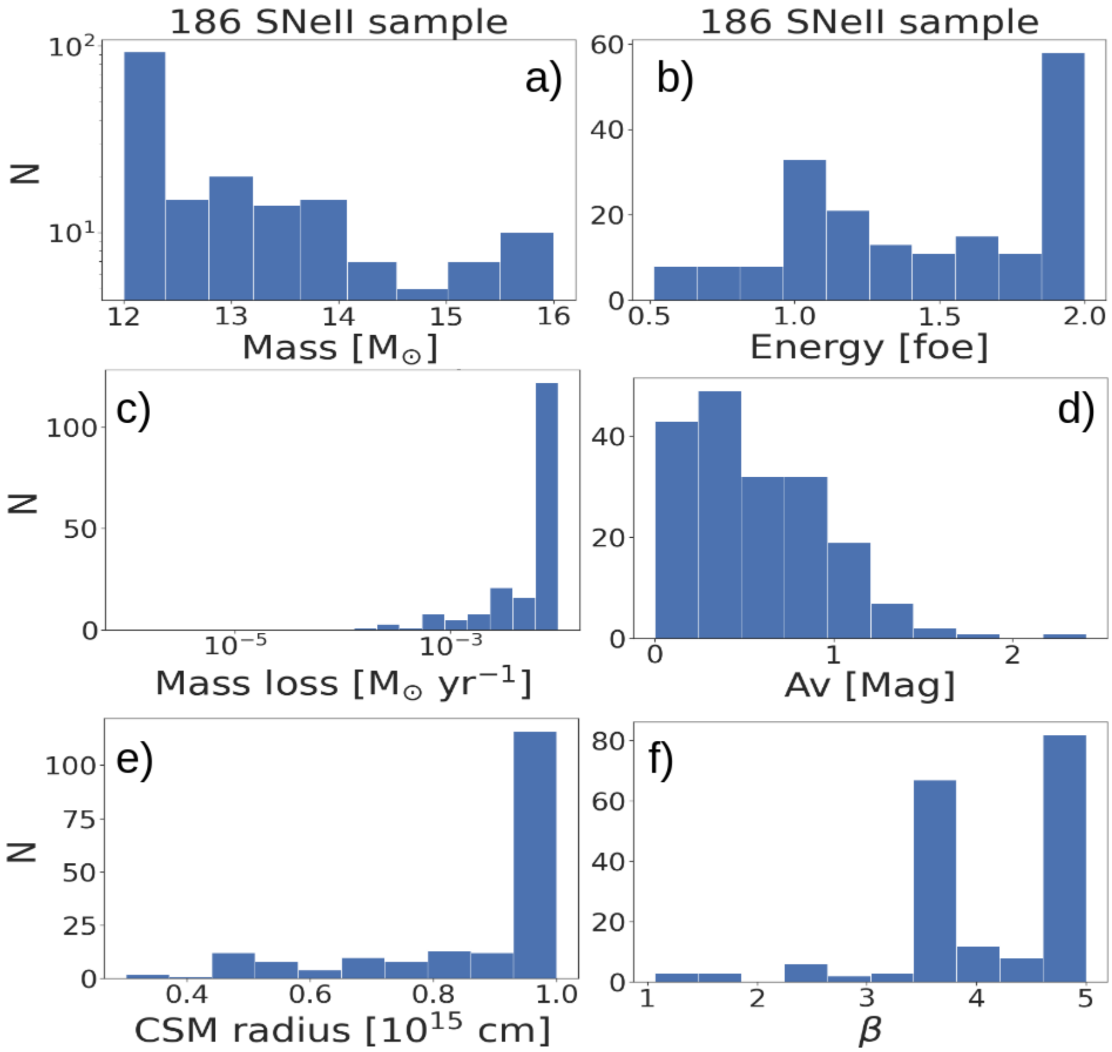

Figure 4.2: Parameters distributions histograms for the whole sample of 186 SNe II. a) Mass distribution, y axis in log scale. b) Energy distribution. c) Mass loss rates distribution log scale binning. d) Attenuation A_V distribution. e)Radii of the CSM distribution. f) β from eq. 1.7 distribution.

4.3 Inferred redshift vs host redshift

Our method can leave the redshift as a variable or fix it if we know the value. In our case, we leave it as a variable in order to compare it with cases where we have information about the redshift.

Different surveys have measured the redshift of galaxies. We can use information from these catalogs to compare the redshifts of SN host galaxies with our inferred values of redshift (the median of the posterior distribution, hereafter LCz). We will use data from Sloan Digital Sky Survey data release 16 [1], NASA/IPAC Extragalactic Database [1], and SIMBAD [76] to

---

[1] The NASA/IPAC Extragalactic Database (NED) is funded by the National Aeronautics and Space Administration and operated by the California Institute of Technology.

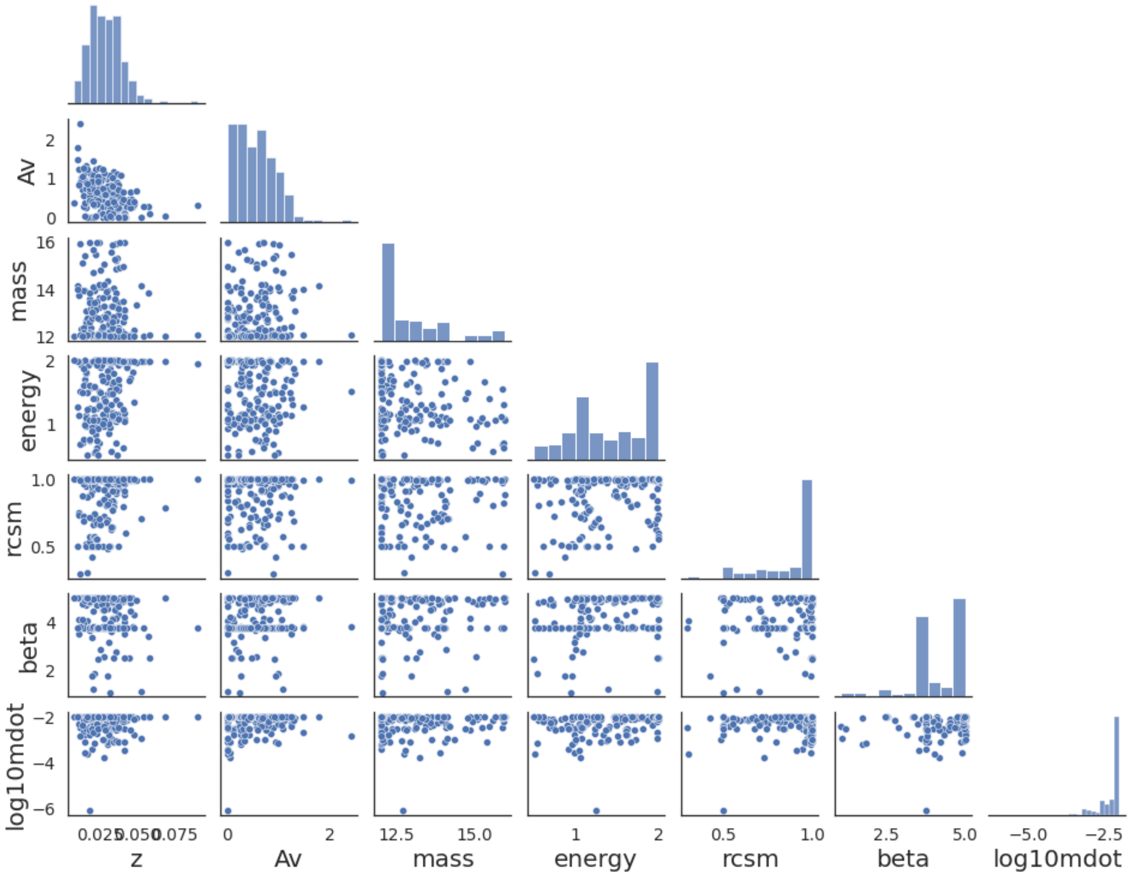

Figure 4.3: Pair-plot of the physical parameters distributions. From left to right (and for top to bottom): Redshift, attenuation (A_V), mass [$M_\odot$], energy [foe], radius CSM [10^{15} cm], β velocity law value (from eq 1.7), and mass loss rate ($\dot{M}$) [$M_\odot$ yr^{-1}] in log scale.

obtain the redshifts of host galaxies.

To implement this, we visually associated a galaxy as the host galaxy of every SNe in our sample (see Appendix 6), and obtain the best available redshift measurement (spectroscopic if available, photometric otherwise). The spectroscopic redshifts (red circles in Figure 4.6) were obtained for 98 SNe from our sample, while photometric redshifts (blue squares in Figure 4.6), hereafter photoz, were obtained for 64 SNe in our sample. The other 24 SNe from our sample could not be associated with a host or the host did not have a redshift available. We found that LCz is comparable with the host spectroscopic redshift as in Figure 4.6 red circles are gathered around the identity line (y = x), and the root-mean square error (RMSE) for only spectroscopic redshift is RMSE = 0.0081, but when comparing LCz to photoz we found that RMSE = 0.1261 .

When comparing the relation between LCz and photoz in Figure 4.6, we see a large scatter around the identity line. To test if this poor correlation is related to our data or due to the low accuracy of photoz, we compare both inferred redshifts, photoz and LCz, to spectroscopic redshifts. To do this we look for the cases in the sample of 98 SNe whose host have a spectroscopic redshift (red circles from Fig. 4.6) that also have a photoz for that host (72 out of the 98 SNe).

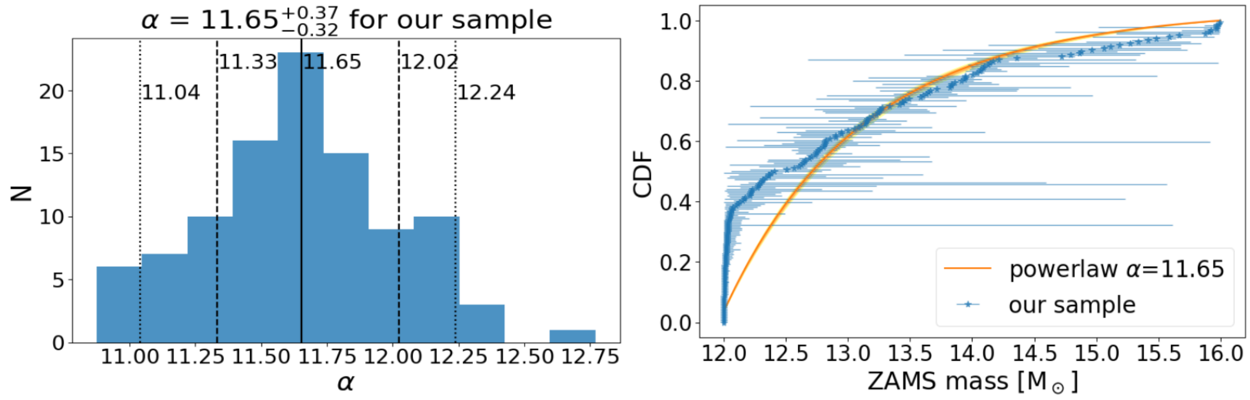

Figure 4.4: Mass IMF power-law exponent estimation for our sample. Left panel: The posterior distribution of α. The median value is reported next to a continuous vertical line, the 16 and 84 percentiles are reported next to dashed vertical lines, and the 5 and 95 percentiles are reported next to dotted vertical lines. Right panel: Cumulative distribution function (CDF) of our mass distribution and CDF of a power law distribution with an exponent equal to the median value reported on the left panel. The orange surface and yellow surface represents the 1 σ and 2 σ error respectively

For the sample of 72 SNe whose host have spectroscopic redshift and photoz measurements available, we check how LCz (black circles) and photoz (orange triangles) compare to spectroscopic redshift in Figure 4.7. We found that the RMSE when comparing LCz to spectroscopic redshift is 0.0088, and the RMSE when comparing photoz to spectroscopic redshift is 0.1567. Also, we found that in 50 of the 72 cases, LCz was closer to the spectroscopic redshift value than photoz.

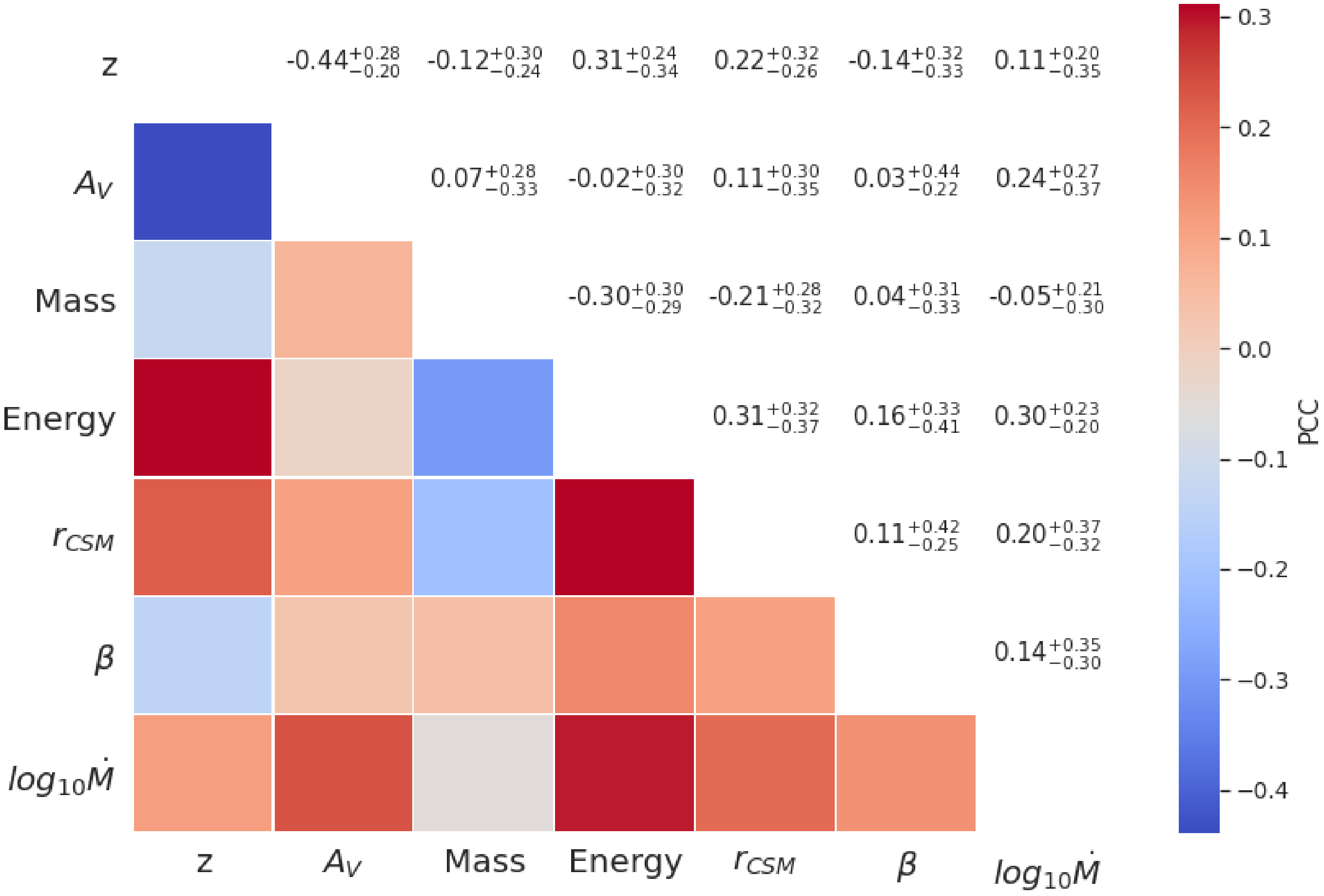

Figure 4.5: Correlation matrix between the physical parameters. In the upper triangle, the reported number correspond to the mean of the Pearson correlation coefficient (PCC) and the subscript and superscript to the distance to the percentiles 2.5 and 97.5 respectively. In the lower triangle the correlation coefficients are colour-coded. From left to right (and for top to bottom): Redshift, attenuation, mass, energy, radius CSM, β velocity law value (from eq 1.7), and mass loss rate.

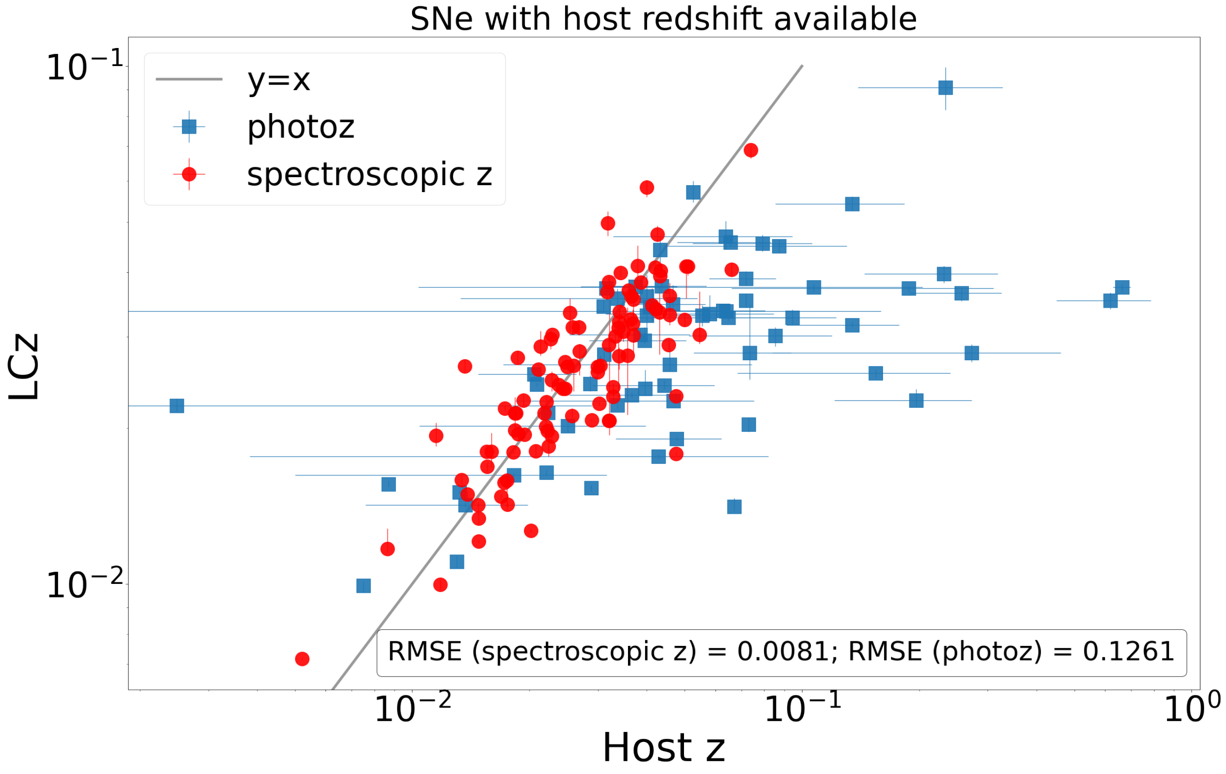

Figure 4.6: Relation between LCz and Host z, the error is reported as error bars when available. Red circles are host galaxies whose best redshift available was spectroscopically measured, while blue squares are host galaxies that best redshift available was photoz. RMSE for LCz compared to spectroscopic redshift and photoz is reported at the bottom right corner.

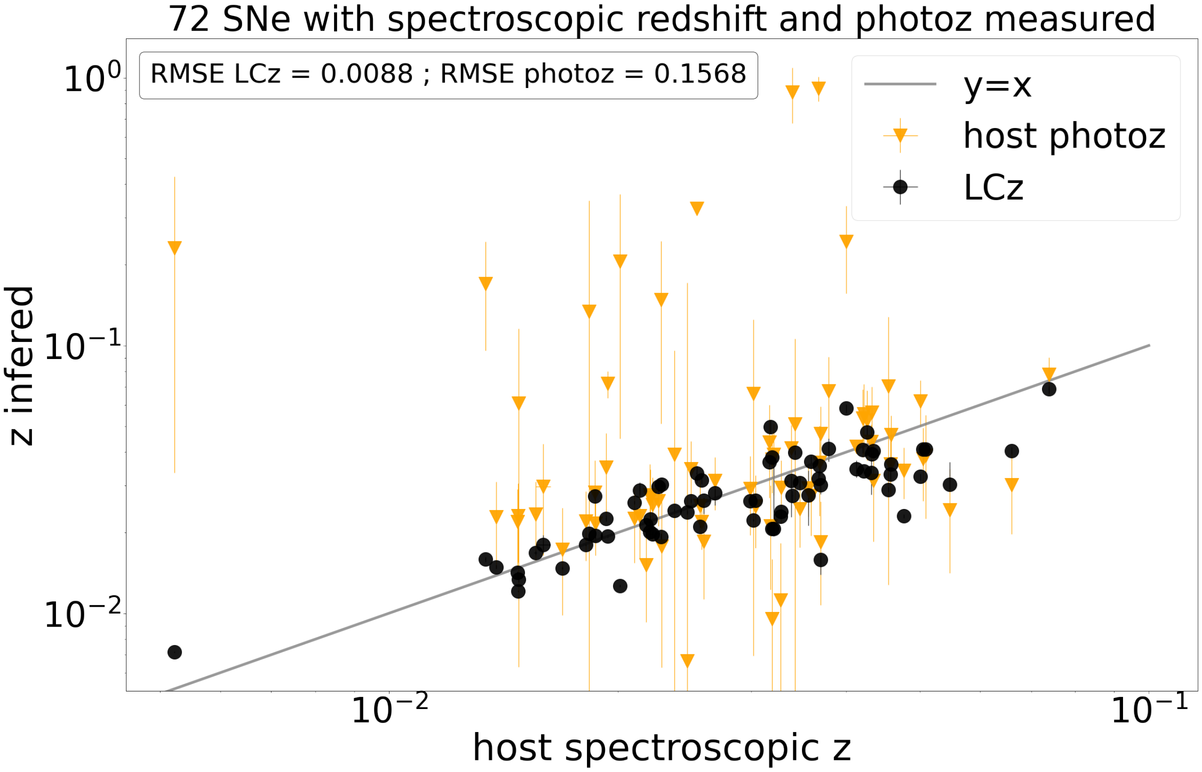

Figure 4.7: Relation between inferred redshift (LCz and photoz) with spectroscopic host redshift. Black circles correspond to LCz, while orange triangles correspond to photoz. Error bars correspond to the errors (when reported) for spectroscopic z and photoz, and for LCz correspond to the lower and upper limits (percentiles 5 and 95 respectively). Root-mean square error for LCz and photoz compared to spectroscopic redshift is reported at the top left corner.

Chapter 5

Analysis

In the previous chapter, we successfully inferred physical parameters for a sample of 186 type II SNe, i.e., the mass of the progenitor, energy of the explosion, mass loss rate, attenuation, radius of the CSM, and the β value of the wind beta velocity law in eq. 1.7. In this chapter, we will discuss the significance of our results, how they compare to similar works, and the relevance of our work in the context of future optical surveys, namely, LSST.

We will start by analyzing the sample distributions. In fig. 4.2 we found that the mass distribution follows a power-law shape, this behavior is in accordance with the literature for stars with mass > 1 M$_\odot$ [61, 15]. Our results also show that the models with a dense CSM near the surface of the progenitor star are the ones that best represent our sample, i.e. the ones with high CSM radius, high mass loss rate, and high β value. The double peak shape on the distributions of energy (near 1 and 2 foe) and β (near 3.75 and 5), may be an artifact created by interpolating near the values of the models.

Despite our results being in accordance with what would be expected (the mass distribution follows a power-law and a dense CSM is preferred), we would like to validate our results somehow. We will discuss this in the next section.

5.1 Validating our results

As a validation method, we look to compare our results with independent measurements of any of the parameters inferred. Most of the parameters are impossible to know without having information about the progenitor, so one option is to compare our results with similar studies in the literature.

So, we search for similar analyses. For example, in [62] they study a sample of SN Ia from the ZTF Bright Transient Survey (BTS) catalog and estimate the attenuation values of their sample. Although SN Ia and SN II are different objects with different evaluations, we compare their results to ours as a sanity check. It is possible to see a similar trend in both works where the distribution peaks around A$_V \sim 0.5$ as seen in Fig 5.1, although SN Ia have largest attenuation overall.

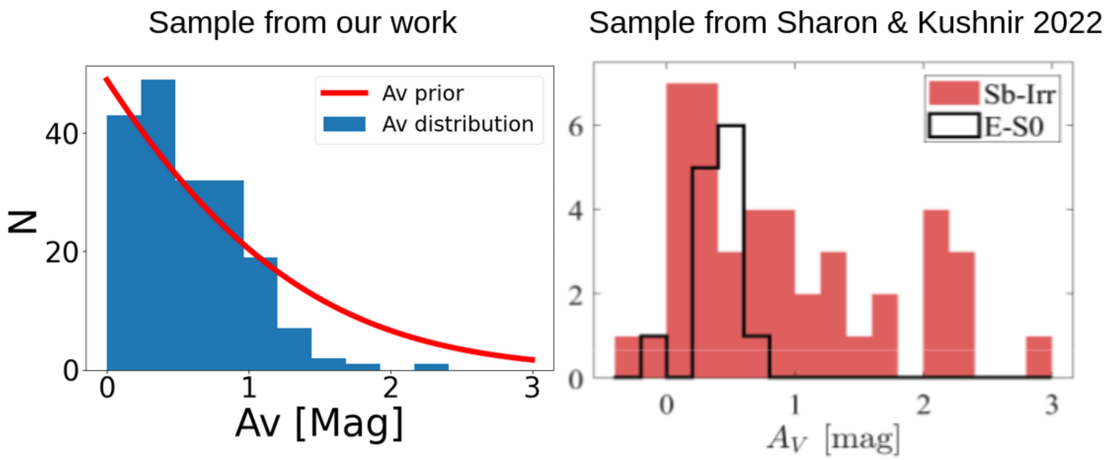
Sample from our work

Sample from Sharon & Kushnir 2022

Figure 5.1: Side to side comparison of the distribution of attenuation of A_V from this work (Left panel), where A_V prior is scaled and shown as a red line, with the one from [62] (Right panel).

[44] inferred SNe II physical parameters from bolometric LCs using hydrodynamical models, and studied the correlation between physical and observed parameters from a sample of SNe II from the Carnegie Supernova Project-I. In their work, they found a weak correlation between explosion energy and ZAMS mass of the progenitor star that differs from the weak (or negligible) negative correlation we found for these two parameters. They found that the inferred masses from their sample followed a power-law with exponential $\alpha = 4.07^{+0.29}_{-0.29}$ for their whole sample, and $\alpha = 6.35^{+0.57}_{-0.52}$ for their gold sample. Both values are steeper than the Salpeter IMF. This was called the IMF incompatibility by [44]. They concluded that this incompatibility is due to the lack of understanding of some physical ingredients and not related to the completeness of their sample. We found a value of $\alpha = 11.65^{+0.37}_{-0.32}$ (see fig. 4.4) steeper than the values found in [44]. Our estimation of the value of α could be overestimated by our limited parameter space. Our mass parameter space goes from 12 $M_\odot$ to 16 $M_\odot$ in contrast with [44] that goes from 9 $M_\odot$ to 25 $M_\odot$. In fig. 4.4 it is possible to see how our limited parameter space affects our estimation of α as most of our masses are stacked near $12M_\odot$. To avoid this issue we repeat the analysis but with the SNe in our sample with inferred masses greater than $12.1M_\odot$. We obtained a value of $\alpha = 4.13^{+0.38}_{-0.39}$ (see fig. 5.2) comparable with the result of [44] for their sample. [44] called this the IMF incompability.

Also, [44] used information about the photosphere velocity to avoid degeneracy in the parameter estimation, i.e that two different models produce the same bolometric LC. The implementation of this is out of the scope of this work, given that we are working in the context of LSST where most of the SNe discovered are not going to be spectroscopically follow-up.

Recent work by [68] used wind-enhanced models from [50], similar to our work, to infer physical parameters from a sample of 45 SNe using ZTF alerts but they included ^{56}Ni mass as a parameter of the model and did not infer the redshift. They also explored a bigger parameter space for energy and mass loss rate. They focused on the effect of using hydrodynamical modeling with different stages of completeness of the LC to forecasts and guide follow-up observations. In their work they find β values around 3 and mass loss rates between 10^{-4}

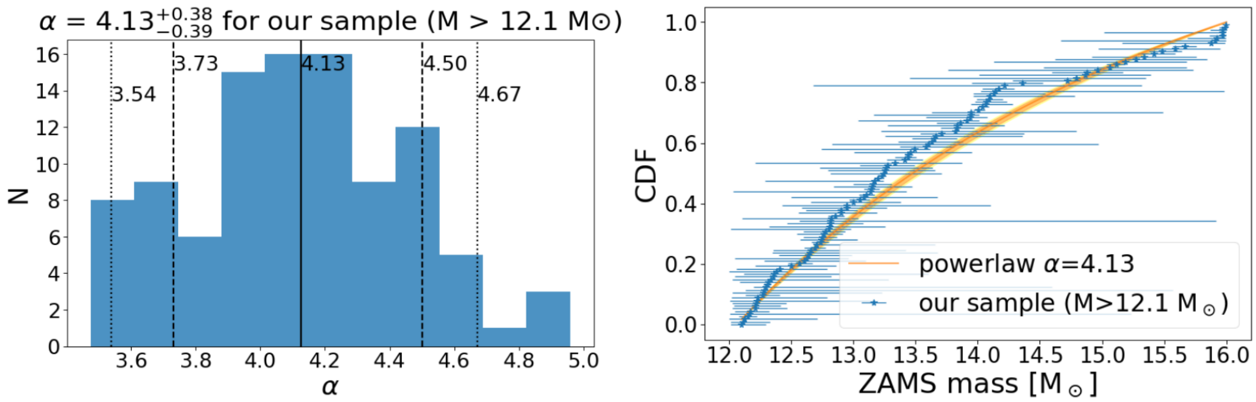

Figure 5.2: Same as fig. 4.4 but for SNe with inferred masses $\geq 12.1 M_\odot$

M$_\odot$ yr^{-1} - 10^{-2} M$_\odot$ yr^{-1} consistent with our results. As well as our results, they did not find a significant correlation among the inferred parameters. A comparison between their results, [44] results, and ours is shown in fig. 5.3 where we compare a parameter combination of energy with mass, A$_V$, and mass loss rate, and mass with β, A$_V$, and mass loss rate. It is possible to see that our mass parameter space is smaller than [44] and [68]. Also, our energy and mass loss rate parameter space is smaller that [68].

19 SNe in our sample were also studied by [68]. The comparison of our inferred parameters with the inferred by [68] is shown in fig. 5.4. Given that in [68] work they did not infer the redshift of the SNe the previous comparison could be affected by it. Therefore, we inferred the parameters of the 19 SNe in both samples with fixed redshift. Fig. 5.5 shows our results fixing z compared with the results of [68].

Overall we found similar trends between our work [44], and [68]. A preference for lower mass stars and dense CSM models. Although figures 5.4 and 5.5 do not show that our results and [68] are the same for the overlapping SNe, they show similar trends for most of the overlapping sample.

We believe that the disagreement in the values is due to the difference in the grid of models and the difference in the data used. A combination of higher energy and lower mass produces fast-rising LCs. [68] has a larger energy space to explore. Therefore, some of their SNe can have similar rise times to ours having larger masses with higher energies. We previously mentioned that the double peak shape found in our energy and β distributions could be an artifact due to the values of our models. We found that [68] has the same problem with values of β close to 3 (see fig. 5.3), this can affect the others parameters and thus cause the difference in figures 5.4 and 5.5. Finally, [68] used only ZTF alerts data, limiting the information they had previous to the explosion and having a lower cadence than our work. Therefore, the accuracy of the inferred parameters by [68] is lower than ours.

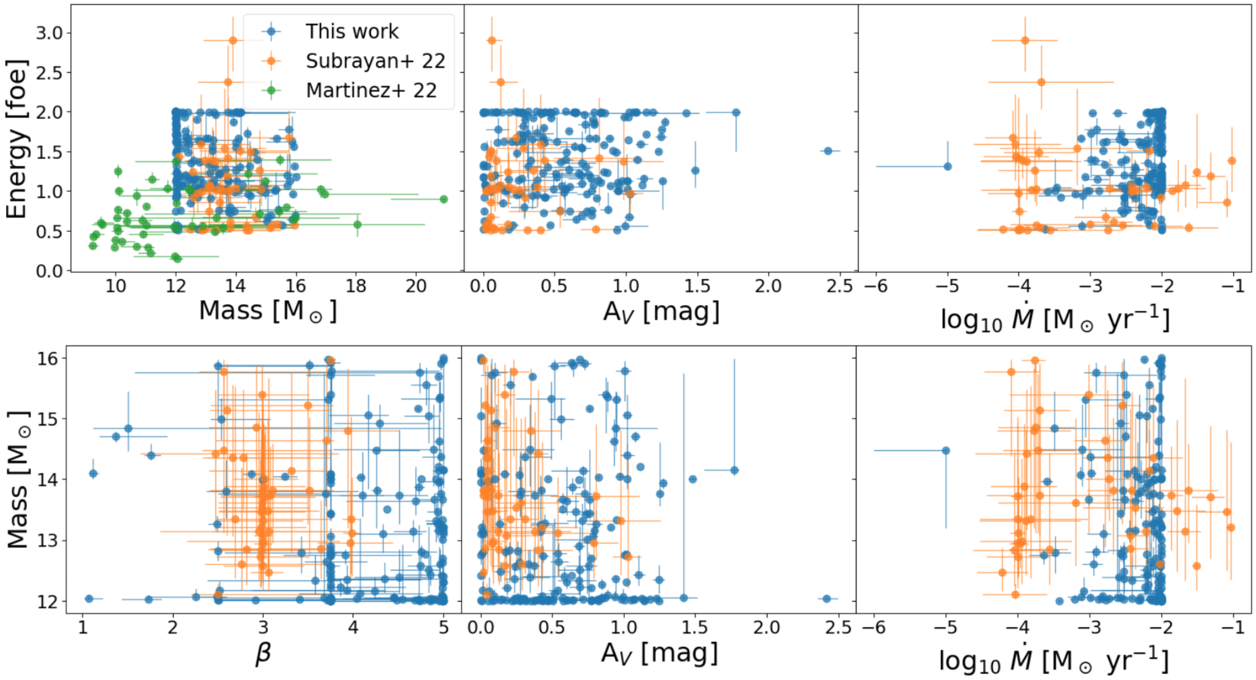

Figure 5.3: Combination of parameters comparison of our resuts (blue circles), [68] results(orange circles), and [44] results (green circles). Top panel: Energy plotted against ZAMS mass, attenuation (A_V), and mass loss rate. Bottom panel: ZAMS mass plotted against beta parameter from the velocity law, attenuation (A_V), and mass loss rate.

5.2 Our method as a distance indicator

The only parameter we can compare with independent measurements is the redshift if we know it for the SN host galaxy. We can compare our LCz, given that we left the redshift of the SN as a variable, with the host galaxy redshift, and if there is agreement it means our method is correctly inferring this parameter. We do this in Fig. 4.6, where we compare LCz with the redshift of the SN host galaxy, finding a good agreement between our results and the spectroscopic redshift. Therefore our method is correctly estimating the redshift. On the other hand, the agreement with photoz is not as good. We could confirm that this is an issue related to the accuracy of photoz, as in Fig. 4.7 we showed that the RMSE of photoz compared with spectroscopic redshift is 3 orders of magnitude higher than LCz compare with spectroscopic redshift.

This last result is particularly interesting because it can allow us to use our obtained redshift for type II SNe using only their LCs and without using the standard candle method (SCM). Using type II SNe as distance indicators is something that previous works have tried with different methods (see [38, 33, 58, 59, 18]) but none of them using hydrodynamical models. The advantages of our method over the others are that it requires only the LCs of a SN from any telescope; and it does not need the bolometric LC, spectroscopic information, or some standardization. The disadvantages will be reviewed as part of the next section, where we will discuss the limitations of our method.

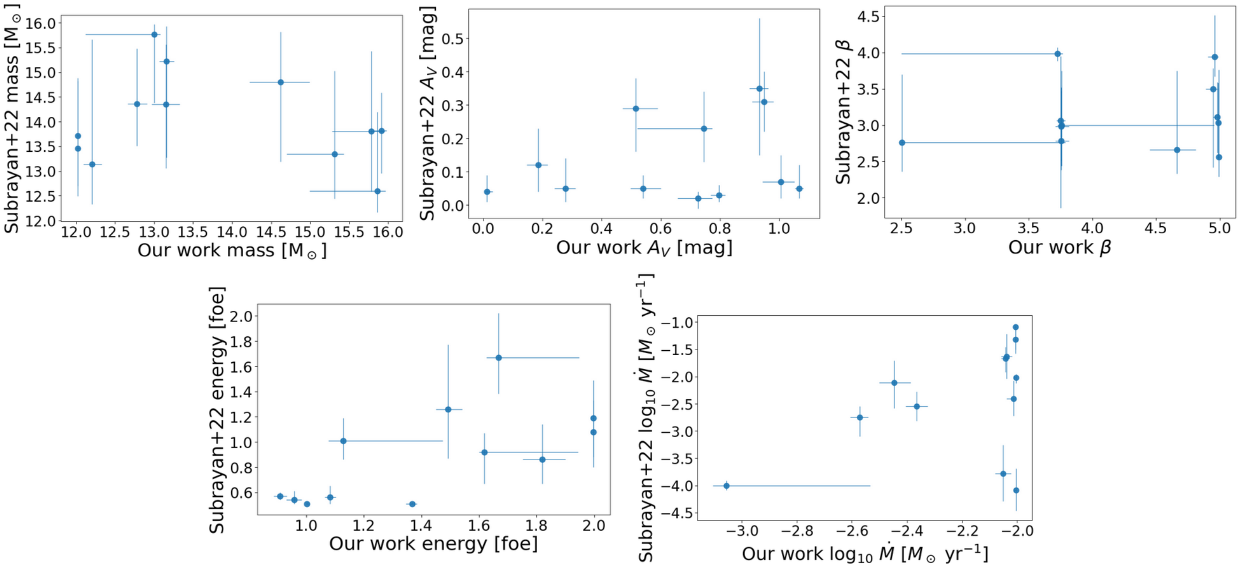

Figure 5.4: Comparison of the inferred parameters for the 19 SNe in both our and [68] sample. The top panel, from left to right, corresponds to mass, attenuation, and wind acceleration parameter β. The bottom panel corresponds to the energy of the explosion and mass loss rate

5.3 Limitations of our method

One of the limitations that our method currently has is that the models we are using can only explore a limited region of the parameter space (see Table 1.1). For example, we do not have information about SNe whose progenitor stars were less massive than 12 $M_\odot$. Also, there may be other physical parameters that we are not considering in this work that could affect the LC of a SN, for example, the nickel-56 mass. Therefore, we need more models to be able to relate all possible RSGs progenitors to SNe LCs and thus have a more complete study of SNe II progenitors.

Another limitation is that we need SNe that are well observed during the rise and in the peak of the LC. If we do not have information that can constrain the explosion time of the SN, our results are going to be extremely inaccurate. This is why we discarded 70 SNe from our sample of 256 confirmed type II SNe. Also, any gap in the LC could mean a bimodality in some parameters or inaccurate results as shown in Fig. 5.6, where the lack of data points between MJD 58920 - 59050 in the LC of SN 2020aer produces wider distributions, i.e. less precise results, in the posterior.

The last limitation we found is that our method uses a large amount of memory. We are using the large partition from the National Laboratory for High Performance Computing (NLHPC, URL: `https://www.nlhpc.cl/`) where we need to allocate 5 Giga Bytes of memory to be able to run the code for one SN. This is because we preload the synthetic LCs when we ran our code. So before being able to use more models, we need to optimize the use of memory, otherwise, the memory we will need could exceed what we have available.

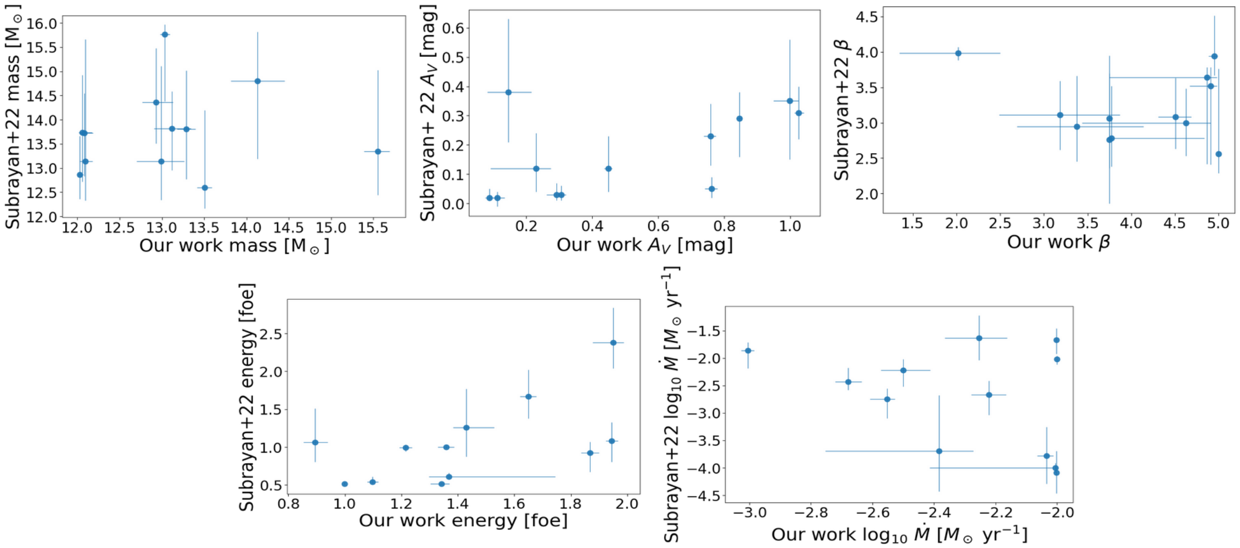

Figure 5.5: Same as fig 5.4 bur we fixed z for our sample

5.4 Implementation on LSST

As stated previously, the amount of data and SNe LSST will discover is going to be an order of magnitude larger than what we are experiencing nowadays, so it is necessary to be prepared for this challenge. Looking forward to LSST, our method can be easily adapted to be used in LSST data, but we still need to improve it and try to fix the limitations discussed in the previous section.

Our method was capable of inferring physical parameters of a sample of 186 SNe in less than 12 hours. Hence we believe that our method will be able to infer parameters of a big sample of LSST in batches as it gathers data with time. In the meantime, we are still working on optimizing our method, not only to be faster but to use fewer computational resources, especially given that we want to test it with more models to explore a larger parameter space.

The main issue we see in our method being used in LSST data is the cadence of LSST. Although the LSST cadence/observation strategy is still not defined, the cadence is going to be worst than ZTF. From our experience during this thesis, the ZTF cadence in some cases was enough so our method could correctly infer the physical parameters from a LC using only ZTF data, but in some other cases it was not and ATLAS data was necessary. Otherwise, we could have bimodality or incorrect posterior distributions. Therefore, we believe that it will be necessary to complement LSST data with data from other sources such as another survey or follow-up data on the object. The latter case seems like the more difficult of the two. This is why in this thesis we work with data from two surveys to explore the first case. Looking at the advantages of LSST, besides the amount of SNe it will discover, it is going to observe in 6 filters, which will allow our method to constrain better the value of A_V and thus a better redshift estimation. Another issue we could face with LSST is that the method of [44] could not break the degeneracy using spectra information, this is something we need to explore in future works if spectra information could be useful given the LSST cadence.

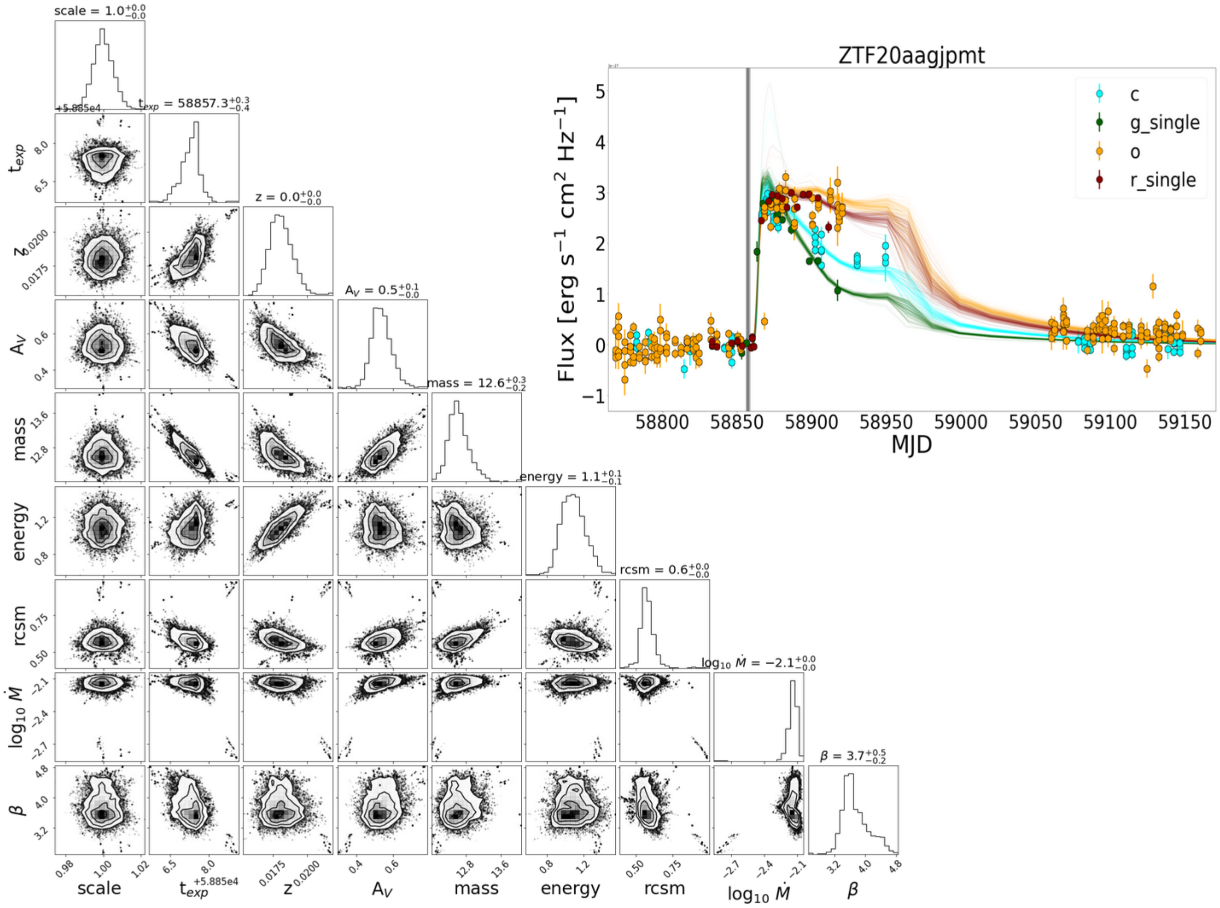

Figure 5.6: Same as 4.1, but for SN 2020aer/ZTF20aagjpmt

It is necessary to test how accurate our method would be using only LSST data, therefore simulations are necessary. Implementing our method on the PLAsTiCC data set [70] or other simulations will be the next step.

Finally, the fact that our method is able to infer the redshift better than photoz is promising. Given that a considerable amount of SNe will have a host galaxy whose redshift has not been measured, it will also allow photometric redshift campaigns to have an independent redshift to compare with.

Chapter 6

Conclusions

We have developed a method that can be used in data from any telescope to infer physical parameters of SNe type II using the models from [49], which is ~ 6 times faster than [24]. The method was applied to a sample of 186 SNe in less than 12 hours. We studied the distribution of physical parameters and found that the dense CSM models are the ones that best represent SNe type II. We found a low negative correlation between redshift and attenuation, while other parameters did not show a negligible correlation [53] as seen in the correlation matrix in Fig. 4.5. We found a that the mass distribution follows a steeper power-law than Salpeter, in agreement with [44].

As a byproduct, we developed a guideline to clean forced photometry data from the ZTF and ATLAS forced photometry services for transient object LCs.

We compare our light curve inferred redshif (LCz) with the host galaxy redshifts for those SNe where this was available and found that our method is capable of correctly estimating the redshift for a SNe with better accuracy than photometric redshift. Considering the amount of data that LSST will produce, we can use our method to estimate the redshift of SNe II based on the LCs. However, to implement this we need a sample of SNe II that are classified with high confidence.

Most SNe discovered by LSST will not have spectroscopic classification. Therefore to use our method with SNe with no spectral information, photometric classification will be necessary (e.g. [24], [23, 69]). Also, given the cadence of LSST, data from other telescopes may be necessary to complement the LCs and reduce the uncertainty in the posteriors.

Our method uses a large amount of memory when running. Therefore, optimization is needed. A possible solution for this problem could be to implement a different package than emcee to estimate Bayesian posteriors, e.g. dynesty [67]. Another option could be to implement our method in a faster programming language. Lastly, looking for another way of representing the synthetic LCs could save memory which is our main issue.

Our method is flexible, so it can be used in other models, as long as we have time series spectra. We look forward to testing it with different models, or with more enhanced wind scenario models so we can explore a bigger parameter space. Also, more models could produce a thinner model grid that will allow for more accurate interpolation.

The code used in this work is publicly available in `https://github.com/fforster/surveysim/tree/dev-javier` .

Acknowledgements

Powered@NLHPC: This thesis was partially supported by the supercomputing infrastructure of the NLHPC (ECM-02)

Bibliography

[1] Romina Ahumada, Carlos Allende Prieto, Andrés Almeida, Friedrich Anders, Scott F. Anderson, Brett H. Andrews, Borja Anguiano, Riccardo Arcodia, Eric Armengaud, Marie Aubert, Santiago Avila, Vladimir Avila-Reese, Carles Badenes, Christophe Balland, Kat Barger, Jorge K. Barrera-Ballesteros, Sarbani Basu, Julian Bautista, Rachael L. Beaton, Timothy C. Beers, B. Izamar T. Benavides, Chad F. Bender, Mariangela Bernardi, Matthew Bershady, Florian Beutler, Christian Moni Bidin, Jonathan Bird, Dmitry Bizyaev, Guillermo A. Blanc, Michael R. Blanton, Médéric Boquien, Jura Borissova, Jo Bovy, W. N. Brandt, Jonathan Brinkmann, Joel R. Brownstein, Kevin Bundy, Martin Bureau, Adam Burgasser, Etienne Burtin, Mariana Cano-Díaz, Raffaella Capasso, Michele Cappellari, Ricardo Carrera, Solène Chabanier, William Chaplin, Michael Chapman, Brian Cherinka, Cristina Chiappini, Peter Doohyun Choi, S. Drew Chojnowski, Haeun Chung, Nicolas Clerc, Damien Coffey, Julia M. Comerford, Johan Comparat, Luiz da Costa, Marie-Claude Cousinou, Kevin Covey, Jeffrey D. Crane, Katia Cunha, Gabriele da Silva Ilha, Yu Sophia Dai, Sanna B. Damsted, Jeremy Darling, Jr. Davidson, James W., Roger Davies, Kyle Dawson, Nikhil De, Axel de la Macorra, Nathan De Lee, Anna Bárbara de Andrade Queiroz, Alice Deconto Machado, Sylvain de la Torre, Flavia Dell'Agli, Hélion du Mas des Bourboux, Aleksandar M. Diamond-Stanic, Sean Dillon, John Donor, Niv Drory, Chris Duckworth, Tom Dwelly, Garrett Ebelke, Sarah Eftekharzadeh, Arthur Davis Eigenbrot, Yvonne P. Elsworth, Mike Eracleous, Ghazaleh Erfanianfar, Stephanie Escoffier, Xiaohui Fan, Emily Farr, José G. Fernández-Trincado, Diane Feuillet, Alexis Finoguenov, Patricia Fofie, Amelia Fraser-McKelvie, Peter M. Frinchaboy, Sebastien Fromenteau, Hai Fu, Lluís Galbany, Rafael A. Garcia, D. A. García-Hernández, Luis Alberto Garma Oehmichen, Junqiang Ge, Marcio Antonio Geimba Maia, Doug Geisler, Joseph Gelfand, Julian Goddy, Violeta Gonzalez-Perez, Kathleen Grabowski, Paul Green, Catherine J. Grier, Hong Guo, Julien Guy, Paul Harding, Sten Hasselquist, Adam James Hawken, Christian R. Hayes, Fred Hearty, S. Hekker, David W. Hogg, Jon A. Holtzman, Danny Horta, Jiamin Hou, Bau-Ching Hsieh, Daniel Huber, Jason A. S. Hunt, J. Ider Chitham, Julie Imig, Mariana Jaber, Camilo Eduardo Jimenez Angel, Jennifer A. Johnson, Amy M. Jones, Henrik Jönsson, Eric Jullo, Yerim Kim, Karen Kinemuchi, IV Kirkpatrick, Charles C., George W. Kite, Mark Klaene, Jean-Paul Kneib, Juna A. Kollmeier, Hui Kong, Marina Kounkel, Dhanesh Krishnarao, Ivan Lacerna, Ting-Wen Lan, Richard R. Lane, David R. Law, Jean-Marc Le Goff, Henry W. Leung, Hannah Lewis, Cheng Li, Jianhui Lian, Lihwai Lin, Dan Long, Penélope Longa-Peña, Britt Lundgren, Brad W. Lyke, J. Ted Mackereth, Chelsea L. MacLeod, Steven R. Majewski, Arturo Manchado, Claudia Maraston, Paul Martini, Thomas Masseron, Karen L.

Masters, Savita Mathur, Richard M. McDermid, Andrea Merloni, Michael Merrifield, Szabolcs Mészáros, Andrea Miglio, Dante Minniti, Rebecca Minsley, Takamitsu Miyaji, Faizan Gohar Mohammad, Benoit Mosser, Eva-Maria Mueller, Demitri Muna, Andrea Muñoz-Gutiérrez, Adam D. Myers, Seshadri Nadathur, Preethi Nair, Kirpal Nandra, Janaina Correa do Nascimento, Rebecca Jean Nevin, Jeffrey A. Newman, David L. Nidever, Christian Nitschelm, Pasquier Noterdaeme, Julia E. O'Connell, Matthew D. Olmstead, Daniel Oravetz, Audrey Oravetz, Yeisson Osorio, Zachary J. Pace, Nelson Padilla, Nathalie Palanque-Delabrouille, Pedro A. Palicio, Hsi-An Pan, Kaike Pan, James Parker, Romain Paviot, Sebastien Peirani, Karla Peña Ramŕez, Samantha Penny, Will J. Percival, Ismael Perez-Fournon, Ignasi Pérez-Ràfols, Patrick Petitjean, Matthew M. Pieri, Marc Pinsonneault, Vijith Jacob Poovelil, Joshua Tyler Povick, Abhishek Prakash, Adrian M. Price-Whelan, M. Jordan Raddick, Anand Raichoor, Amy Ray, Sandro Barboza Rembold, Mehdi Rezaie, Rogemar A. Riffel, Rogério Riffel, Hans-Walter Rix, Annie C. Robin, A. Roman-Lopes, Carlos Román-Zúñiga, Benjamin Rose, Ashley J. Ross, Graziano Rossi, Kate Rowlands, Kate H. R. Rubin, Mara Salvato, Ariel G. Sánchez, Laura Sánchez-Menguiano, José R. Sánchez-Gallego, Conor Sayres, Adam Schaefer, Ricardo P. Schiavon, Jaderson S. Schimoia, Edward Schlafly, David Schlegel, Donald P. Schneider, Mathias Schultheis, Axel Schwope, Hee-Jong Seo, Aldo Serenelli, Arman Shafieloo, Shoaib Jamal Shamsi, Zhengyi Shao, Shiyin Shen, Matthew Shetrone, Raphael Shirley, Víctor Silva Aguirre, Joshua D. Simon, M. F. Skrutskie, Anže Slosar, Rebecca Smethurst, Jennifer Sobeck, Bernardo Cervantes Sodi, Diogo Souto, David V. Stark, Keivan G. Stassun, Matthias Steinmetz, Dennis Stello, Julianna Stermer, Thaisa Storchi-Bergmann, Alina Streblyanska, Guy S. Stringfellow, Amelia Stutz, Genaro Suárez, Jing Sun, Manuchehr Taghizadeh-Popp, Michael S. Talbot, Jamie Tayar, Aniruddha R. Thakar, Riley Theriault, Daniel Thomas, Zak C. Thomas, Jeremy Tinker, Rita Tojeiro, Hector Hernandez Toledo, Christy A. Tremonti, Nicholas W. Troup, Sarah Tuttle, Eduardo Unda-Sanzana, Marica Valentini, Jaime Vargas-González, Mariana Vargas-Magaña, Jose Antonio Vázquez-Mata, M. Vivek, David Wake, Yuting Wang, Benjamin Alan Weaver, Anne-Marie Weijmans, Vivienne Wild, John C. Wilson, Robert F. Wilson, Nathan Wolthuis, W. M. Wood-Vasey, Renbin Yan, Meng Yang, Christophe Yèche, Olga Zamora, Pauline Zarrouk, Gail Zasowski, Kai Zhang, Cheng Zhao, Gongbo Zhao, Zheng Zheng, Zheng Zheng, Guangtun Zhu, and Hu Zou. The 16th Data Release of the Sloan Digital Sky Surveys: First Release from the APOGEE-2 Southern Survey and Full Release of eBOSS Spectra. , 249(1):3, July 2020.

[2] Athem W. Alsabti and Paul Murdin. *Handbook of Supernovae.* 2017.

[3] Joseph P. Anderson, Santiago González-Gaitán, Mario Hamuy, Claudia P. Gutiérrez, Maximilian D. Stritzinger, Felipe Olivares E., Mark M. Phillips, Steve Schulze, Roberto Antezana, Luis Bolt, Abdo Campillay, Sergio Castellón, Carlos Contreras, Thomas de Jaeger, Gastón Folatelli, Francisco Förster, Wendy L. Freedman, Luis González, Eric Hsiao, Wojtek Krzemiński, Kevin Krisciunas, José Maza, Patrick McCarthy, Nidia I. Morrell, Sven E. Persson, Miguel Roth, Francisco Salgado, Nicholas B. Suntzeff, and Joanna Thomas-Osip. Characterizing the V-band Light-curves of Hydrogen-rich Type II Supernovae. , 786(1):67, May 2014.

[4] W. D. Arnett. Analytic solutions for light curves of supernovae of Type II. , 237:541–549, April 1980.

[5] W. D. Arnett. Type I supernovae. I - Analytic solutions for the early part of the light curve. , 253:785–797, February 1982.

[6] R. Barbon, F. Ciatti, and L. Rosino. Photometric properties of type II supernovae. , 72:287–292, February 1979.

[7] Eric C. Bellm, Shrinivas R. Kulkarni, Matthew J. Graham, Richard Dekany, Roger M. Smith, Reed Riddle, Frank J. Masci, George Helou, Thomas A. Prince, Scott M. Adams, C. Barbarino, Tom Barlow, James Bauer, Ron Beck, Justin Belicki, Rahul Biswas, Nadejda Blagorodnova, Dennis Bodewits, Bryce Bolin, Valery Brinnel, Tim Brooke, Brian Bue, Mattia Bulla, Rick Burruss, S. Bradley Cenko, Chan-Kao Chang, Andrew Connolly, Michael Coughlin, John Cromer, Virginia Cunningham, Kishalay De, Alex Delacroix, Vandana Desai, Dmitry A. Duev, Gwendolyn Eadie, Tony L. Farnham, Michael Feeney, Ulrich Feindt, David Flynn, Anna Franckowiak, S. Frederick, C. Fremling, Avishay Gal-Yam, Suvi Gezari, Matteo Giomi, Daniel A. Goldstein, V. Zach Golkhou, Ariel Goobar, Steven Groom, Eugean Hacopians, David Hale, John Henning, Anna Y. Q. Ho, David Hover, Justin Howell, Tiara Hung, Daniela Huppenkothen, David Imel, Wing-Huen Ip, Željko Ivezić, Edward Jackson, Lynne Jones, Mario Juric, Mansi M. Kasliwal, S. Kaspi, Stephen Kaye, Michael S. P. Kelley, Marek Kowalski, Emily Kramer, Thomas Kupfer, Walter Landry, Russ R. Laher, Chien-De Lee, Hsing Wen Lin, Zhong-Yi Lin, Ragnhild Lunnan, Matteo Giomi, Ashish Mahabal, Peter Mao, Adam A. Miller, Serge Monkewitz, Patrick Murphy, Chow-Choong Ngeow, Jakob Nordin, Peter Nugent, Eran Ofek, Maria T. Patterson, Bryan Penprase, Michael Porter, Ludwig Rauch, Umaa Rebbapragada, Dan Reiley, Mickael Rigault, Hector Rodriguez, Jan van Roestel, Ben Rusholme, Jakob van Santen, S. Schulze, David L. Shupe, Leo P. Singer, Maayane T. Soumagnac, Robert Stein, Jason Surace, Jesper Sollerman, Paula Szkody, F. Taddia, Scott Terek, Angela Van Sistine, Sjoert van Velzen, W. Thomas Vestrand, Richard Walters, Charlotte Ward, Quan-Zhi Ye, Po-Chieh Yu, Lin Yan, and Jeffry Zolkower. The Zwicky Transient Facility: System Overview, Performance, and First Results. , 131(995):018002, January 2019.

[8] P. D. Bennett. Chromospheres and Winds of Red Supergiants: An Empirical Look at Outer Atmospheric Structure. In C. Leitherer, P. D. Bennett, P. W. Morris, and J. Th. Van Loon, editors, *Hot and Cool: Bridging Gaps in Massive Star Evolution*, volume 425 of *Astronomical Society of the Pacific Conference Series*, page 181, June 2010.

[9] Melina C. Bersten, Omar Benvenuto, and Mario Hamuy. Hydrodynamical Models of Type II Plateau Supernovae. , 729(1):61, March 2011.

[10] S. I. Blinnikov, R. Eastman, O. S. Bartunov, V. A. Popolitov, and S. E. Woosley. A Comparative Modeling of Supernova 1993J. , 496(1):454–472, March 1998.

[11] S. I. Blinnikov, F. K. Röpke, E. I. Sorokina, M. Gieseler, M. Reinecke, C. Travaglio, W. Hillebrandt, and M. Stritzinger. Theoretical light curves for deflagration models of type Ia supernova. , 453(1):229–240, July 2006.

[12] Sergei Blinnikov, Peter Lundqvist, Oleg Bartunov, Ken'ichi Nomoto, and Koichi Iwamoto. Radiation Hydrodynamics of SN 1987A. I. Global Analysis of the Light Curve for the First 4 Months. , 532(2):1132–1149, April 2000.

[13] Thomas Boch and Jérôme Desroziers. ipyaladin: Enabling Aladin Lite in Jupyter Notebooks. In Pascal Ballester, Jorge Ibsen, Mauricio Solar, and Keith Shortridge, editors, *Astronomical Data Analysis Software and Systems XXVII*, volume 522 of *Astronomical Society of the Pacific Conference Series*, page 117, April 2020.

[14] Bradley W Carroll and Dale A Ostlie. *An introduction to modern astrophysics*. Cambridge University Press, 2017.

[15] Gilles Chabrier. Galactic Stellar and Substellar Initial Mass Function. , 115(809):763–795, July 2003.

[16] E. Chatzopoulos, J. Craig Wheeler, and J. Vinko. Generalized Semi-analytical Models of Supernova Light Curves. , 746(2):121, February 2012.

[17] Shlomo Dado and Arnon Dar. Analytical Expressions for Light Curves of Ordinary and Superluminous Type Ia Supernovae. , 809(1):32, August 2015.

[18] T. de Jaeger, L. Galbany, S. González-Gaitán, R. Kessler, A. V. Filippenko, F. Förster, M. Hamuy, P. J. Brown, T. M. Davis, C. P. Gutiérrez, C. Inserra, G. F. Lewis, A. Möller, D. Scolnic, M. Smith, D. Brout, D. Carollo, R. J. Foley, K. Glazebrook, S. R. Hinton, E. Macaulay, B. Nichol, M. Sako, N. E. Sommer, B. E. Tucker, T. M. C. Abbott, M. Aguena, S. Allam, J. Annis, S. Avila, E. Bertin, S. Bhargava, D. Brooks, D. L. Burke, A. Carnero Rosell, M. Carrasco Kind, J. Carretero, M. Costanzi, M. Crocce, L. N. da Costa, J. De Vicente, S. Desai, H. T. Diehl, P. Doel, A. Drlica-Wagner, T. F. Eifler, J. Estrada, S. Everett, B. Flaugher, P. Fosalba, J. Frieman, J. García-Bellido, E. Gaztanaga, D. Gruen, R. A. Gruendl, J. Gschwend, G. Gutierrez, W. G. Hartley, D. L. Hollowood, K. Honscheid, D. J. James, K. Kuehn, N. Kuropatkin, T. S. Li, M. Lima, M. A. G. Maia, F. Menanteau, R. Miquel, A. Palmese, F. Paz-Chinchón, A. A. Plazas, A. K. Romer, A. Roodman, E. Sanchez, V. Scarpine, M. Schubnell, S. Serrano, I. Sevilla-Noarbe, M. Soares-Santos, E. Suchyta, M. E. C. Swanson, G. Tarle, D. Thomas, D. L. Tucker, T. N. Varga, A. R. Walker, J. Weller, R. Wilkinson, and DES Collaboration. Studying Type II supernovae as cosmological standard candles using the Dark Energy Survey. , 495(4):4860–4892, July 2020.

[19] Richard Dekany, Roger M. Smith, Reed Riddle, Michael Feeney, Michael Porter, David Hale, Jeffry Zolkower, Justin Belicki, Stephen Kaye, John Henning, Richard Walters, John Cromer, Alex Delacroix, Hector Rodriguez, Daniel J. Reiley, Peter Mao, David Hover, Patrick Murphy, Rick Burruss, John Baker, Marek Kowalski, Klaus Reif, Phillip Mueller, Eric Bellm, Matthew Graham, and Shrinivas R. Kulkarni. The Zwicky Transient Facility: Observing System. , 132(1009):038001, March 2020.

[20] Tamar Faran, Tomer Goldfriend, Ehud Nakar, and Re'em Sari. Recombination Effects on Supernova Light Curves. , 879(1):20, July 2019.

[21] Alexei V. Filippenko. Optical Spectra of Supernovae. , 35:309–355, January 1997.

[22] Jim Fuller. Pre-supernova outbursts via wave heating in massive stars - I. Red supergiants. , 470(2):1642–1656, September 2017.

[23] F. Förster, G. Cabrera-Vives, E. Castillo-Navarrete, P. A. Estévez, P. Sánchez-Sáez, J. Arredondo, F. E. Bauer, R. Carrasco-Davis, M. Catelan, F. Elorrieta, S. Eyheramendy, P. Huijse, G. Pignata, E. Reyes, I. Reyes, D. Rodríguez-Mancini, D. Ruz-Mieres, C. Valenzuela, I. Álvarez-Maldonado, N. Astorga, J. Borissova, A. Clocchiatti, D. De Cicco, C. Donoso-Oliva, L. Hernández-García, M. J. Graham, A. Jordán, R. Kurtev, A. Mahabal, J. C. Maureira, A. Muñoz-Arancibia, R. Molina-Ferreiro, A. Moya, W. Palma, M. Pérez-Carrasco, P. Protopapas, M. Romero, L. Sabatini-Gacitua, A. Sánchez, J. San Martín, C. Sepúlveda-Cobo, E. Vera, and J. R. Vergara. The Automatic Learning for the Rapid Classification of Events (ALeRCE) Alert Broker. , 161(5):242, May 2021.

[24] F. Förster, T. J. Moriya, J. C. Maureira, J. P. Anderson, S. Blinnikov, F. Bufano, G. Cabrera-Vives, A. Clocchiatti, T. de Jaeger, P. A. Estévez, L. Galbany, S. González-Gaitán, G. Gräfener, M. Hamuy, E. Y. Hsiao, P. Huentelemu, P. Huijse, H. Kuncarayakti, J. Martínez, G. Medina, F. Olivares E., G. Pignata, A. Razza, I. Reyes, J. San Martín, R. C. Smith, E. Vera, A. K. Vivas, A. de Ugarte Postigo, S. C. Yoon, C. Ashall, M. Fraser, A. Gal-Yam, E. Kankare, L. Le Guillou, P. A. Mazzali, N. A. Walton, and D. R. Young. The delay of shock breakout due to circumstellar material evident in most type II supernovae. *Nature Astronomy*, 2:808, September 2018.

[25] E. E. E. Gall, J. Polshaw, R. Kotak, A. Jerkstrand, B. Leibundgut, D. Rabinowitz, J. Sollerman, M. Sullivan, S. J. Smartt, J. P. Anderson, S. Benetti, C. Baltay, U. Feindt, M. Fraser, S. González-Gaitán, C. Inserra, K. Maguire, R. McKinnon, S. Valenti, and D. Young. A comparative study of Type II-P and II-L supernova rise times as exemplified by the case of LSQ13cuw. , 582:A3, October 2015.

[26] P. M. Garnavich, B. E. Tucker, A. Rest, E. J. Shaya, R. P. Olling, D. Kasen, and A. Villar. Shock Breakout and Early Light Curves of Type II-P Supernovae Observed with Kepler. , 820(1):23, March 2016.

[27] S. González-Gaitán, N. Tominaga, J. Molina, L. Galbany, F. Bufano, J. P. Anderson, C. Gutierrez, F. Förster, G. Pignata, M. Bersten, D. A. Howell, M. Sullivan, R. Carlberg, T. de Jaeger, M. Hamuy, P. V. Baklanov, and S. I. Blinnikov. The rise-time of Type II supernovae. , 451(2):2212–2229, August 2015.

[28] Jonathan Goodman and Jonathan Weare. Ensemble samplers with affine invariance. *Communications in Applied Mathematics and Computational Science*, 5(1):65–80, January 2010.

[29] Jonathan Goodman and Jonathan Weare. Ensemble samplers with affine invariance. *Communications in Applied Mathematics and Computational Science*, 5(1):65–80, January 2010.

[30] Geoffrey Grimmett and David Stirzaker. *Probability and random processes*. Oxford university press, 2020.

[31] M. A. T. Groenewegen and H. J. G. L. M. Lamers. The winds of O-stars. I. an analysis of the UV line profiles with theSEI method. , 79:359–383, September 1989.

[32] James Guillochon, Jerod Parrent, Luke Zoltan Kelley, and Raffaella Margutti. An Open Catalog for Supernova Data. , 835(1):64, January 2017.

[33] Mario Andres Hamuy. *Type II supernovae as distance indicators*. PhD thesis, University of Arizona, January 2001.

[34] A. Jerkstrand, C. Fransson, K. Maguire, S. Smartt, M. Ergon, and J. Spyromilio. The progenitor mass of the Type IIP supernova SN 2004et from late-time spectral modeling. , 546:A28, October 2012.

[35] Daniel Kasen. One-zone arnett model of radioactive transients.

[36] Daniel Kasen and Lars Bildsten. Supernova Light Curves Powered by Young Magnetars. , 717(1):245–249, July 2010.

[37] D. Khazov, O. Yaron, A. Gal-Yam, I. Manulis, A. Rubin, S. R. Kulkarni, I. Arcavi, M. M. Kasliwal, E. O. Ofek, Y. Cao, D. Perley, J. Sollerman, A. Horesh, M. Sullivan, A. V. Filippenko, P. E. Nugent, D. A. Howell, S. B. Cenko, J. M. Silverman, H. Ebeling, F. Taddia, J. Johansson, R. R. Laher, J. Surace, U. D. Rebbapragada, P. R. Wozniak, and T. Matheson. Flash Spectroscopy: Emission Lines from the Ionized Circumstellar Material around ¡10-day-old Type II Supernovae. , 818(1):3, February 2016.

[38] R. P. Kirshner and J. Kwan. Distances to extragalactic supernovae. , 193:27–36, October 1974.

[39] Siu Kwan Lam, Stuartarchibald, Antoine Pitrou, Mark Florisson, Stan Seibert, Graham Markall, Esc, Todd A. Anderson, Rjenc29, Guilherme Leobas, Luk-F-A, Jay Bourque, Aaron Meurer, Travis E. Oliphant, Densmirn, Michael Collison, Njwhite, Ehsan Totoni, Ethan Pronovost, Stefan Seefeld, Hernan Grecco, Eric Wieser, Pearu Peterson, Isaac Virshup, Matty G, Itamar Turner-Trauring, James Bourbeau, Anton Malakhov, Uri Laserson, and Pedro Morales Maries. numba/numba: Version 0.54.0. Zenodo, September 2021.

[40] Weidong Li, Jesse Leaman, Ryan Chornock, Alexei V Filippenko, Dovi Poznanski, Mohan Ganeshalingam, Xiaofeng Wang, Maryam Modjaz, Saurabh Jha, Ryan J Foley, et al. Nearby supernova rates from the lick observatory supernova search–ii. the observed luminosity functions and fractions of supernovae in a complete sample. *Monthly Notices of the Royal Astronomical Society*, 412(3):1441–1472, 2011.

[41] LSST. Supernovae. `https://www.lsst.org/science/transient-optical-sky/supernovae`. Accessed: 2022-06-20.

[42] LSST Science Collaboration, Paul A. Abell, Julius Allison, Scott F. Anderson, John R. Andrew, J. Roger P. Angel, Lee Armus, David Arnett, S. J. Asztalos, Tim S. Axelrod, Stephen Bailey, D. R. Ballantyne, Justin R. Bankert, Wayne A. Barkhouse, Jeffrey D. Barr, L. Felipe Barrientos, Aaron J. Barth, James G. Bartlett, Andrew C. Becker, Jacek Becla, Timothy C. Beers, Joseph P. Bernstein, Rahul Biswas, Michael R. Blanton, Joshua S. Bloom, John J. Bochanski, Pat Boeshaar, Kirk D. Borne, Marusa Bradac, W. N. Brandt, Carrie R. Bridge, Michael E. Brown, Robert J. Brunner, James S. Bullock, Adam J. Burgasser, James H. Burge, David L. Burke, Phillip A.

Cargile, Srinivasan Chandrasekharan, George Chartas, Steven R. Chesley, You-Hua Chu, David Cinabro, Mark W. Claire, Charles F. Claver, Douglas Clowe, A. J. Connolly, Kem H. Cook, Jeff Cooke, Asantha Cooray, Kevin R. Covey, Christopher S. Culliton, Roelof de Jong, Willem H. de Vries, Victor P. Debattista, Francisco Delgado, Ian P. Dell'Antonio, Saurav Dhital, Rosanne Di Stefano, Mark Dickinson, Benjamin Dilday, S. G. Djorgovski, Gregory Dobler, Ciro Donalek, Gregory Dubois-Felsmann, Josef Durech, Ardis Eliasdottir, Michael Eracleous, Laurent Eyer, Emilio E. Falco, Xiaohui Fan, Christopher D. Fassnacht, Harry C. Ferguson, Yanga R. Fernandez, Brian D. Fields, Douglas Finkbeiner, Eduardo E. Figueroa, Derek B. Fox, Harold Francke, James S. Frank, Josh Frieman, Sebastien Fromenteau, Muhammad Furqan, Gaspar Galaz, A. Gal-Yam, Peter Garnavich, Eric Gawiser, John Geary, Perry Gee, Robert R. Gibson, Kirk Gilmore, Emily A. Grace, Richard F. Green, William J. Gressler, Carl J. Grillmair, Salman Habib, J. S. Haggerty, Mario Hamuy, Alan W. Harris, Suzanne L. Hawley, Alan F. Heavens, Leslie Hebb, Todd J. Henry, Edward Hileman, Eric J. Hilton, Keri Hoadley, J. B. Holberg, Matt J. Holman, Steve B. Howell, Leopoldo Infante, Zeljko Ivezic, Suzanne H. Jacoby, Bhuvnesh Jain, R, Jedicke, M. James Jee, J. Garrett Jernigan, Saurabh W. Jha, Kathryn V. Johnston, R. Lynne Jones, Mario Juric, Mikko Kaasalainen, Styliani, Kafka, Steven M. Kahn, Nathan A. Kaib, Jason Kalirai, Jeff Kantor, Mansi M. Kasliwal, Charles R. Keeton, Richard Kessler, Zoran Knezevic, Adam Kowalski, Victor L. Krabbendam, K. Simon Krughoff, Shrinivas Kulkarni, Stephen Kuhlman, Mark Lacy, Sebastien Lepine, Ming Liang, Amy Lien, Paulina Lira, Knox S. Long, Suzanne Lorenz, Jennifer M. Lotz, R. H. Lupton, Julie Lutz, Lucas M. Macri, Ashish A. Mahabal, Rachel Mandelbaum, Phil Marshall, Morgan May, Peregrine M. McGehee, Brian T. Meadows, Alan Meert, Andrea Milani, Christopher J. Miller, Michelle Miller, David Mills, Dante Minniti, David Monet, Anjum S. Mukadam, Ehud Nakar, Douglas R. Neill, Jeffrey A. Newman, Sergei Nikolaev, Martin Nordby, Paul O'Connor, Masamune Oguri, John Oliver, Scot S. Olivier, Julia K. Olsen, Knut Olsen, Edward W. Olszewski, Hakeem Oluseyi, Nelson D. Padilla, Alex Parker, Joshua Pepper, John R. Peterson, Catherine Petry, Philip A. Pinto, James L. Pizagno, Bogdan Popescu, Andrej Prsa, Veljko Radcka, M. Jordan Raddick, Andrew Rasmussen, Arne Rau, Jeonghee Rho, James E. Rhoads, Gordon T. Richards, Stephen T. Ridgway, Brant E. Robertson, Rok Roskar, Abhijit Saha, Ata Sarajedini, Evan Scannapieco, Terry Schalk, Rafe Schindler, Samuel Schmidt, Sarah Schmidt, Donald P. Schneider, German Schumacher, Ryan Scranton, Jacques Sebag, Lynn G. Seppala, Ohad Shemmer, Joshua D. Simon, M. Sivertz, Howard A. Smith, J. Allyn Smith, Nathan Smith, Anna H. Spitz, Adam Stanford, Keivan G. Stassun, Jay Strader, Michael A. Strauss, Christopher W. Stubbs, Donald W. Sweeney, Alex Szalay, Paula Szkody, Masahiro Takada, Paul Thorman, David E. Trilling, Virginia Trimble, Anthony Tyson, Richard Van Berg, Daniel Vanden Berk, Jake VanderPlas, Licia Verde, Bojan Vrsnak, Lucianne M. Walkowicz, Benjamin D. Wandelt, Sheng Wang, Yun Wang, Michael Warner, Risa H. Wechsler, Andrew A. West, Oliver Wiecha, Benjamin F. Williams, Beth Willman, David Wittman, Sidney C. Wolff, W. Michael Wood-Vasey, Przemek Wozniak, Patrick Young, Andrew Zentner, and Hu Zhan. LSST Science Book, Version 2.0. *arXiv e-prints*, page arXiv:0912.0201, December 2009.

[43] Jonathan R. Marshall, Jacco Th. van Loon, Mikako Matsuura, Peter R. Wood, Albert A. Zijlstra, and Patricia A. Whitelock. Asymptotic giant branch superwind speed at low

metallicity. , 355(4):1348–1360, December 2004.

[44] L. Martinez, J. P. Anderson, M. C. Bersten, M. Hamuy, S. González-Gaitán, M. Orellana, M. Stritzinger, M. M. Phillips, C. P. Gutiérrez, C. Burns, T. de Jaeger, K. Ertini, G. Folatelli, F. Förster, L. Galbany, P. Hoeflich, E. Y. Hsiao, N. Morrell, P. J. Pessi, and N. B. Suntzeff. Type II supernovae from the Carnegie Supernova Project-I. III. Understanding SN II diversity through correlations between physical and observed properties. , 660:A42, April 2022.

[45] L. Martinez, M. C. Bersten, J. P. Anderson, S. González-Gaitán, F. Förster, and G. Folatelli. Progenitor properties of type II supernovae: fitting to hydrodynamical models using Markov chain Monte Carlo methods. , 642:A143, October 2020.

[46] Frank Masci, Russ Laher, David Shupe, and Ben Rusholme. Generating lightcurves from forced psf-fit photometry on ztf difference images. `https://irsa.ipac.caltech.edu/data/ZTF/docs/forcedphot.pdf`, April 2022.

[47] R. Minkowski. Spectra of Supernovae. , 53(314):224, August 1941.

[48] Takashi Moriya, Nozomu Tominaga, Sergei I. Blinnikov, Petr V. Baklanov, and Elena I. Sorokina. Erratum: Supernovae from red supergiants with extensive mass loss. , 424(3):2400–2400, August 2012.

[49] Takashi J. Moriya, Francisco Förster, Sung-Chul Yoon, Götz Gräfener, and Sergei I. Blinnikov. Type IIP supernova light curves affected by the acceleration of red supergiant winds. , 476(2):2840–2851, May 2018.

[50] Takashi J. Moriya, Bhagya M. Subrayan, Dan Milisavljevic, and Sergei I. Blinnikov. Synthetic red supergiant explosion model grid for systematic characterization of Type II supernovae. *arXiv e-prints*, page arXiv:2303.01532, March 2023.

[51] Takashi J. Moriya, Sung-Chul Yoon, Götz Gräfener, and Sergei I. Blinnikov. Immediate dense circumstellar environment of supernova progenitors caused by wind acceleration: its effect on supernova light curves. , 469(1):L108–L112, July 2017.

[52] Viktoriya Morozova, Anthony L. Piro, Jim Fuller, and Schuyler D. Van Dyk. The Influence of Late-stage Nuclear Burning on Red Supergiant Supernova Light Curves. , 891(2):L32, March 2020.

[53] MJMMJ Mukaka. Statistics corner: a guide to appropriate use of correlation in medical research. *Malawi Med J*, 24(3):69–71, 2012.

[54] Bill Paxton, Lars Bildsten, Aaron Dotter, Falk Herwig, Pierre Lesaffre, and Frank Timmes. Modules for Experiments in Stellar Astrophysics (MESA). , 192(1):3, January 2011.

[55] Bill Paxton, Matteo Cantiello, Phil Arras, Lars Bildsten, Edward F. Brown, Aaron Dotter, Christopher Mankovich, M. H. Montgomery, Dennis Stello, F. X. Timmes, and Richard Townsend. Modules for Experiments in Stellar Astrophysics (MESA): Planets, Oscillations, Rotation, and Massive Stars. , 208(1):4, September 2013.

[56] Bill Paxton, Pablo Marchant, Josiah Schwab, Evan B. Bauer, Lars Bildsten, Matteo Cantiello, Luc Dessart, R. Farmer, H. Hu, N. Langer, R. H. D. Townsend, Dean M. Townsley, and F. X. Timmes. Modules for Experiments in Stellar Astrophysics (MESA): Binaries, Pulsations, and Explosions. , 220(1):15, September 2015.

[57] Bill Paxton, Josiah Schwab, Evan B. Bauer, Lars Bildsten, Sergei Blinnikov, Paul Duffell, R. Farmer, Jared A. Goldberg, Pablo Marchant, Elena Sorokina, Anne Thoul, Richard H. D. Townsend, and F. X. Timmes. Modules for Experiments in Stellar Astrophysics (MESA): Convective Boundaries, Element Diffusion, and Massive Star Explosions. , 234(2):34, February 2018.

[58] Dovi Poznanski, Nathaniel Butler, Alexei V. Filippenko, Mohan Ganeshalingam, Weidong Li, Joshua S. Bloom, Ryan Chornock, Ryan J. Foley, Peter E. Nugent, Jeffrey M. Silverman, S. Bradley Cenko, Elinor L. Gates, Douglas C. Leonard, Adam A. Miller, Maryam Modjaz, Frank J. D. Serduke, Nathan Smith, Brandon J. Swift, and Diane S. Wong. Improved Standardization of Type II-P Supernovae: Application to an Expanded Sample. , 694(2):1067–1079, April 2009.

[59] Ó. Rodríguez, G. Pignata, M. Hamuy, A. Clocchiatti, M. M. Phillips, K. Krisciunas, N. I. Morrell, G. Folatelli, M. Roth, S. Castellón, I. S. Jang, Y. Apostolovski, P. López, S. Marchi, R. Ramírez, and P. Sánchez. Type II supernovae as distance indicators at near-IR wavelengths. , 483(4):5459–5479, March 2019.

[60] Adam Rubin and Avishay Gal-Yam. Exploring the Efficacy and Limitations of Shock-cooling Models: New Analysis of Type II Supernovae Observed by the Kepler Mission. , 848(1):8, October 2017.

[61] Edwin E. Salpeter. The Luminosity Function and Stellar Evolution. , 121:161, January 1955.

[62] Amir Sharon and Doron Kushnir. The ZTF-BTS Type Ia supernovae luminosity function is consistent with a single progenitor channel for the explosions. , 509(4):5275–5297, February 2022.

[63] S. J. Smartt, J. J. Eldridge, R. M. Crockett, and J. R. Maund. The death of massive stars - I. Observational constraints on the progenitors of Type II-P supernovae. , 395(3):1409–1437, May 2009.

[64] Stephen J. Smartt, Justyn R. Maund, Margaret A. Hendry, Christopher A. Tout, Gerard F. Gilmore, Seppo Mattila, and Chris R. Benn. Detection of a Red Supergiant Progenitor Star of a Type II-Plateau Supernova. *Science*, 303(5657):499–503, January 2004.

[65] K. W. Smith, S. J. Smartt, D. R. Young, J. L. Tonry, L. Denneau, H. Flewelling, A. N. Heinze, H. J. Weiland, B. Stalder, A. Rest, C. W. Stubbs, J. P. Anderson, T.-W Chen, P. Clark, A. Do, F. Förster, M. Fulton, J. Gillanders, O. R. McBrien, D. O'Neill, S. Srivastav, and D. E. Wright. Design and operation of the ATLAS transient science server. *Publications of the Astronomical Society of the Pacific*, 132(1014):085002, jun 2020.

[66] S. Sonnett, K. Meech, R. Jedicke, S. Bus, J. Tonry, and O. Hainaut. Testing Accuracy and Precision of Existing Photometry Algorithms on Moving Targets. , 125(926):456, April 2013.

[67] Joshua S. Speagle and Kyle Barbary. dynesty: Dynamic Nested Sampling package. Astrophysics Source Code Library, record ascl:1809.013, September 2018.

[68] Bhagya M. Subrayan, Danny Milisavljevic, Takashi J. Moriya, Kathryn E. Weil, Geoffrey Lentner, Mark Linvill, John Banovetz, Braden Garretson, Jack Reynolds, Niharika Sravan, Ryan Chornock, and Rafaella Margutti. Inferencing Progenitor and Explosion Properties of Evolving Core-collapse Supernovae from Zwicky Transient Facility Light Curves. *arXiv e-prints*, page arXiv:2211.15702, November 2022.

[69] P. Sánchez-Sáez, I. Reyes, C. Valenzuela, F. Förster, S. Eyheramendy, F. Elorrieta, F. E. Bauer, G. Cabrera-Vives, P. A. Estévez, M. Catelan, G. Pignata, P. Huijse, D. De Cicco, P. Arévalo, R. Carrasco-Davis, J. Abril, R. Kurtev, J. Borissova, J. Arredondo, E. Castillo-Navarrete, D. Rodriguez, D. Ruz-Mieres, A. Moya, L. Sabatini-Gacitúa, C. Sepúlveda-Cobo, and E. Camacho-Iñiguez. Alert Classification for the ALeRCE Broker System: The Light Curve Classifier. , 161(3):141, March 2021.

[70] The PLAsTiCC team, Jr. Allam, Tarek, Anita Bahmanyar, Rahul Biswas, Mi Dai, Lluís Galbany, Renée Hložek, Emille E. O. Ishida, Saurabh W. Jha, David O. Jones, Richard Kessler, Michelle Lochner, Ashish A. Mahabal, Alex I. Malz, Kaisey S. Mandel, Juan Rafael Martínez-Galarza, Jason D. McEwen, Daniel Muthukrishna, Gautham Narayan, Hiranya Peiris, Christina M. Peters, Kara Ponder, Christian N. Setzer, The LSST Dark Energy Science Collaboration, The LSST Transients, and Variable Stars Science Collaboration. The Photometric LSST Astronomical Time-series Classification Challenge (PLAsTiCC): Data set. *arXiv e-prints*, page arXiv:1810.00001, September 2018.

[71] J. L. Tonry, L. Denneau, A. N. Heinze, B. Stalder, K. W. Smith, S. J. Smartt, C. W. Stubbs, H. J. Weiland, and A. Rest. ATLAS: A High-cadence All-sky Survey System. , 130(988):064505, June 2018.

[72] John L. Tonry. An Early Warning System for Asteroid Impact. , 123(899):58, January 2011.

[73] J. Anthony Tyson. Cosmology data analysis challenges and opportunities in the LSST sky survey. In *Journal of Physics Conference Series*, volume 1290 of *Journal of Physics Conference Series*, page 012001, October 2019.

[74] Schuyler D. Van Dyk, Weidong Li, and Alexei V. Filippenko. On the Progenitor of the Type II-Plateau Supernova 2003gd in M74. , 115(813):1289–1295, November 2003.

[75] V. Ashley Villar, Edo Berger, Brian D. Metzger, and James Guillochon. Theoretical Models of Optical Transients. I. A Broad Exploration of the Duration-Luminosity Phase Space. , 849(1):70, November 2017.

[76] M. Wenger, F. Ochsenbein, D. Egret, P. Dubois, F. Bonnarel, S. Borde, F. Genova, G. Jasniewicz, S. Laloë, S. Lesteven, and R. Monier. The SIMBAD astronomical database. The CDS reference database for astronomical objects. , 143:9–22, April 2000.

Host association

Host association was done using a modify version for the code available in the following repository `https://github.com/alercebroker/TNS_upload`.

To determine the host galaxy we do a visual inspection using ipyaladin [13]. The process to associate each SNe to a host is as follows: First, we load a Pan-STARRS-DR1 image as seen in the left panels of Figure 1, where every color square is a source in NED, SIMBAD, or SDSS catalogs. We can hover the cursor over the different squares to look for information about the source, such as the name of the source, the survey, the redshift of the object (if available), the kind of redshift (spectroscopic or photometric), etc. We visually associate a SN to its host galaxy, if multiple sources (squares in Figure 1) are in the core of the host, we select the one with the best redshift available (spectroscopic over photometric), and if possible the best available that report errors. We select the source by clicking on the corresponding square and saving the following information about the hos: Name, right ascension, declination', offset, source, redshift spec (True if redshift is spectroscopic, False otherwise), redshift, redshift error, redshift type.

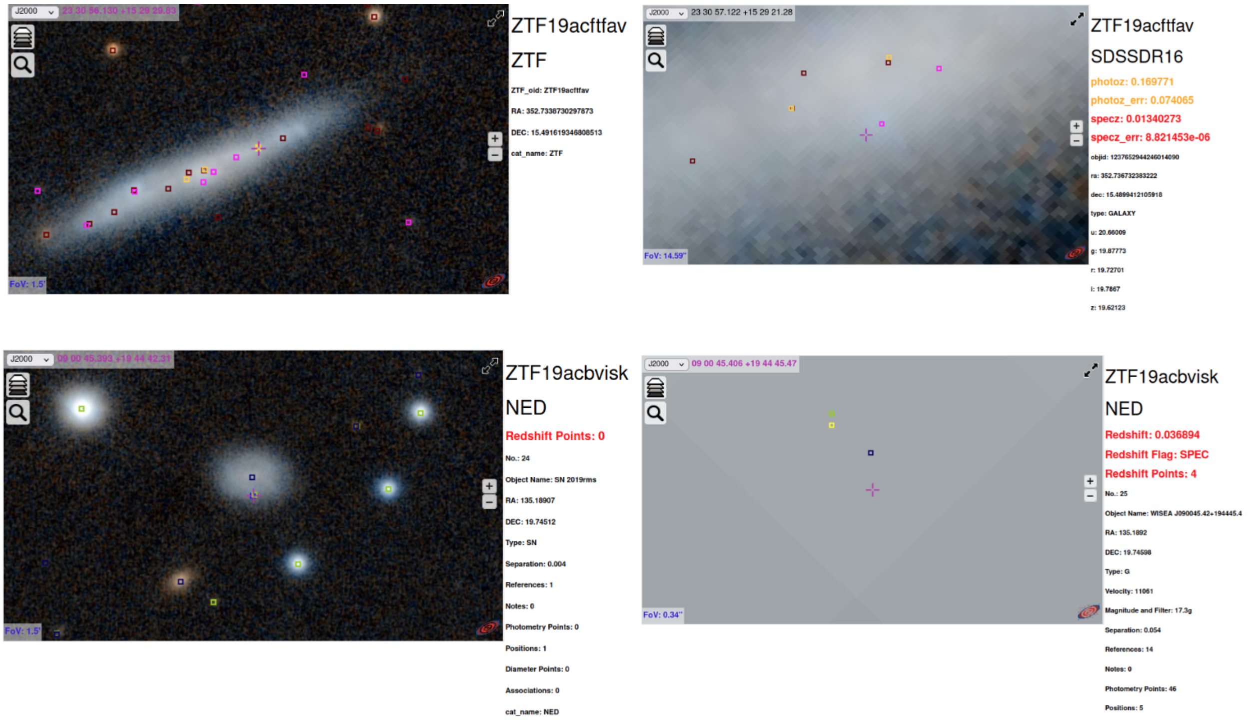

ZTF19acftfav

ZTF

ZTF_oid: ZTF19acftfav
RA: 352.7338730297873
DEC: 15.491619346808513
cat_name: ZTF

ZTF19acftfav

SDSSDR16

photoz: 0.169771
photoz_err: 0.074065
specz: 0.01340273
specz_err: 8.821453e-06
objid: 1237652944246014090
ra: 352.736732383222
dec: 15.4899412105918
type: GALAXY
u: 20.66009
g: 19.87773
r: 19.72701
i: 19.7867
z: 19.62123

ZTF19acbvisk

NED

Redshift Points: 0
No.: 24
Object Name: SN 2019rms
RA: 135.18907
DEC: 19.74512
Type: SN
Separation: 0.004
References: 1
Notes: 0
Photometry Points: 0
Positions: 1
Diameter Points: 0
Associations: 0
cat_name: NED

ZTF19acbvisk

NED

Redshift: 0.036894
Redshift Flag: SPEC
Redshift Points: 4
No.: 25
Object Name: WISEA J090045.42+194445.4
RA: 135.1892
DEC: 19.74598
Type: G
Velocity: 11061
Magnitude and Filter: 17.3g
Separation: 0.054
References: 14
Notes: 0
Photometry Points: 46
Positions: 5

Figure 1: Left panels: Images of Pan-STARRS with a field of view (FOV) of 1.5' centered in the SN location. The upper panel corresponds to ZTF19acftfav and the lower panel corresponds to ZTF19acbvisk. Right panels: Same as left panels but zoom in on the core of the host galaxy. Multiple squares in the images correspond to data from different surveys